5-2015

Impact of Solidification on Tensile Strength of CoCr 2LC in Selective Laser Melting

Stefan Robert Popp
University of Tennessee - Knoxville, spopp@vols.utk.edu

To the Graduate Council:

I am submitting herewith a thesis written by Stefan Robert Popp entitled "Impact of Solidification on Tensile Strength of CoCr 2LC in Selective Laser Melting." I have examined the final electronic copy of this thesis for form and content and recommend that it be accepted in partial fulfillment of the requirements for the degree of Master of Science, with a major in Mechanical Engineering.

Sudarsanam S. Babu, Major Professor

We have read this thesis and recommend its acceptance:

Ryan R. Dehoff, Taigang G. Nieh

Accepted for the Council:
Dixie L. Thompson

Vice Provost and Dean of the Graduate School

(Original signatures are on file with official student records.)

Impact of Solidification on Tensile Strength of CoCr 2LC in Selective Laser Melting

A Thesis Presented for the
Master of Science
Degree
The University of Tennessee, Knoxville

Stefan Robert Popp
May 2015

Dedication

To my newborn daughter Hanna. Thanks for keeping up the pressure to finish my thesis as soon as possible.

Acknowledgements

I would like to thank all those who helped and provided their support during the preparation of this thesis.

Firstly, I would like to thank Professor Babu for giving me the opportunity to work on his team and make use of all the resources at ORNL. I greatly appreciate his constant guidance and support.

Secondly, I would like to express my sincere thanks to Jonaaron Jones for countless hours of support and patience throughout my whole project and Dr. Michel Kirka for his advice and assistance in EBSD and SEM microscopy. They made the introduction to a new group and new work environment much easier. Our beer meetings were also a great way to let off some steam.

Furthermore, I would also like to thank Dr. Grant Helmreich for his assistance in deciphering the research.

Also, I would like to thank Keith Carver for running my experiments on the Renishaw machine.

Moreover, I would like to thank the entire team. It has been great working with all of them. I have learned a lot during the process and also had fun doing so.

Last but not least, I would like to thank Dr. Ryan Dehoff and Professor Nieh for serving on my graduate committee.
Personally I would like to thank my family on both sides of the Atlantic. I could never have gotten where I am without them and could never thank them enough. I also would like to thank my loving wife Tarah who stood beside me through many difficulties and also beautiful times. She has accompanied me during my studies and this work. She supported me at all times and gave me power. She also spell-checked this thesis with “endless” patience ;). Thank you! Ich liebe Dich!

Abstract

Selective laser melting (SLM) is an additive manufacturing technique with which parts of nearly arbitrary shape and complexity can be produced. The parts are generated layer for layer directly out of a 3D CAD model completely without forming tools.

In this work, the selective laser technique is applied to a CoCrMo alloy. Due to its high corrosion resistance, wear-resistance, and heat resistance, this alloy is mainly used for medical or high temperature applications.

A systematic approach is used to investigate the influence of the process parameters laser power and exposure time (pulsed laser) on density, melt pool dimensions, melt pool shape, deformation due to residual stresses, microstructure, and mechanical properties. The density analysis as well as the melt pool analysis is carried out by means of optical light microscopy. A qualitative method is used to evaluate the deformation due to residual stress. The microstructure is evaluated using scanning electron microscopy and electron backscatter diffraction. A tensile test is performed to evaluate the mechanical properties.

Parts with a density greater than 99% are obtained where the volume energy exceeds 61 J/mm³. The melt pools have an elliptic shape, a width of 120 to 140 um, and a height of 70 to 80 um, depending on the volume energy. So-called twincantilevers are used to measure the deformation of builds due to residual stresses. The deformation in z-direction is on average 2.1 mm. The microstructure consists of elongated grains parallel to the build direction with different crystal orientations. Anisotropy is confirmed via tensile test. A maximum yield stress of 1000 MPa and tensile strength of 1200 MPa are found, while the average yield stress is found to be 680 MPa with a tensile strength of 1100 MPa. Furthermore, it is established, that the position of the samples on the base plate has a huge influence on the density and, hence, the mechanical properties.

Table of Contents

List of Tables

List of Figures

1 Introduction

Selective laser melting (SLM) is an additive manufacturing process with which complex series components can be created out of materials that are identical with the final product. The production is carried out layer for layer directly out of a 3D CAD volume model completely without forming tools. The layered composition allows for great geometrical freedom. For these reasons, SLM offers the potential to shorten the time span between the conception and manufacturing of components. The inherent potential for cost saving in the production of prototypes and small series is of special interest to countries with high personnel wages.

CoCr 2LC is a cobalt-based alloy with very low carbon content. The main alloying components are cobalt, chrome, and molybdenum. CoCr 2LC is conventionally used for casting or forging and meets the ASTM F75 standards for surgical implants. Due to its high resistance to corrosion and erosion and its biocompatibility, CoCr 2LC has been chiefly implemented in medical technology, for example for hip and knee prostheses, bone screws, surgical clamps, and the supporting structures for heart valves [1].

Previous analyses (see *Chapter 2.2*) confirm the processability of ASTM F75 cobalt-based alloys by means of SLM. Research involving pulsed laser in combination with CoCr 2LC is not established. There are also no studies pertaining to the influence of the geometry of the melt pool on the tensile strength. Furthermore, it is unknown how the various process parameters impact the residual stress and, hence, the mechanical properties like yield stress and tensile strength.

According to Davis [1], the manufacturing process of CoCr alloys has a strong influence on their mechanical properties. This project will examine the impact of various process parameters of pulsed laser on the geometry of melt pools, the resulting microstructures, and their deformation due to residual stresses. Finally, these factors will be studied in relation to the mechanical properties. The yield stress and tensile strength results achieved through the SLM process will be compared with values for conventionally manufactured samples in the literature.

2 State of the Art

2.1 The SLM Technique

The process cycle is schematically represented in *Figure 1*. The geometry of the construction component is derived from the 3D CAD model and is by means of software sliced into layers of a defined thickness before initiation of the actual manufacturing process (A). The construction process is divided into the following repeating steps:

- Powder application: powder is applied as a defined layer (1)
- Selective melting: the powder and a portion of the subjacent layer is selectively melted by means of exposure to laser radiation (2)
- Lowering of the platform: the platform is lowered following the selective melting process to enable application of a new layer of powder (3)

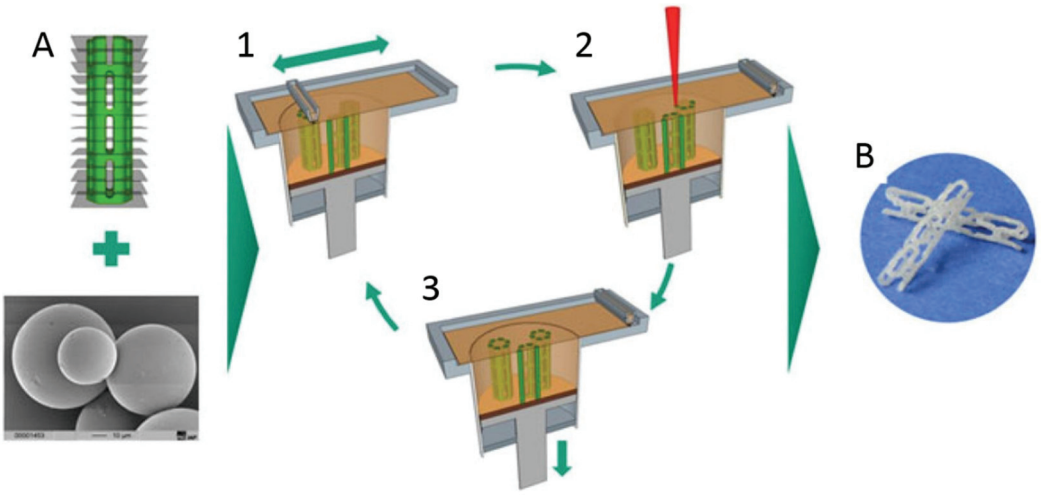

Figure 1 Schematic representation of the SLM process [2]

A comprehensive demonstration of the basic principles of the process can be found in [3] and [4], including explanations of the process management and important principles pertaining to SLM.

2.2 Generative manufacturing of Co-Cr Alloys and Co-Cr-Mo Alloys

A short chronological summary of selected works pertaining to SLM and Co-Cr alloys and Co-Cr-Mo alloys, respectively, can be found below. The SLM System utilized, the most important parameters, as well as the chemical composition of the powder substance used is outlined in *Table 1*. Detailed information can be obtained from the respective sources.

2.2.1 Eligibility of Co-Cr-Mo for the SLM Process

A Co-Cr-Mo alloy was first examined using SLM within the scope of a paper regarding the workability of biocompatible materials in 2007 by Vandenbroucke and Kruth [5].

Objective: Aim of the investigation was to identify parameters for the generative construction of dental prostheses and to optimize them by means of iterative parameter variations. Assessment criteria were density, corrosion behavior (Co-emission/day), and surface roughness.
Results: The generation of samples with a density of >99.9% is possible with SLM. The corrosion behavior of the generated parts is favorable in comparison with conventionally manufactured parts. The surface roughness is dependent on the surface of the component examined between $RZ = 87$ µm for the top face of the part and $RZ = 90$ µm for the lateral surface.

2.2.2 Tensile Strength

Jevremovic et al focused on the mechanical characteristics of samples constructed by means of SLM from a cobalt-based alloy F75 for use in dental prostheses [6].

Objective: Yield strength ($R_{p0.2}$), tensile strength (R_m), and elongation (A) were compared with the values for the conventionally casted alloy Remanium GM 380+.
Remanium GM 380+ is also a cobalt-based alloy with a similar chemical composition to F75 [6].
Results: Tensile specimens taken from F75 produced with SLM have a slightly higher yield stress ($R_{p0.2}$) (approx. 10% higher); the tensile strength is, however, significantly higher (approx. 50%) in

comparison to Remanium GM 380+. On average, the tensile specimens manufactured via SLM obtained a yield stress of approx. 700 MPa and a tensile strength of approximately 1400 MPa.

2.2.3 Dependence of Tensile Strength From the Position in a Build Chamber

Gatto et al examined the density, tensile strength, microstructure, and fracture plane of Co-Cr-Mo samples using a scan strategy arranged in bands [7]. The values attained for tensile strength and density were compared with values from the literature for conventionally manufactured samples and with samples manufactured by means of electron beam welding.

Objective: The aim was to investigate the influence of the scanning strategy on the tensile strength from SLM samples. For this purpose, samples were constructed at 0°, 45°, and 90° in the x-y plain.
Results: The attained densities are approximately 2.3% less than the values available in the literature. Tensile strengths with an average of 1290 MPa were attained. The attained values are comparable with established values in the literature for electron beam welding and surpass those obtained with conventionally forged or casted parts.

2.2.4 The Relationship of Tensile Strength to Build Angle, Microstructure, and Density

Atsushi et al examined the microstructure as well as mechanical characteristics, including tensile strength, yield strength, and elongation, of the alloy depicted in *Table 1* [8]. Furthermore, iterative laser output and hatch spacing were varied with the aim to generate more dense samples by means of SLM. Tensile specimens were built with varying parameters in three different angles (0°- parallel to the build direction, 45°, 90°- perpendicular to the build direction).

Objective: The aim was to determine whether samples produced with SLM are suitable for dental products.
Results: It was found that dense samples with a multitude of combinations with regard to construction parameters could be manufactured as long as a volume energy E_V greater than 400 J/mm³ was obtained.
Microstructure analysis by means of SEM showed cellular, dendritic growth parallel to the direction of construction with a dominant γ Phase (fcc) and a marginal proportion of the ε Phase (martensitic

hcp). At the grain boundaries, there were comparatively higher values of Cr and Mo measured than at the core. In addition, needle-like sediments with elevated Cr and Mn content were detected. Crystallographic analysis of orientation revealed a preferred orientation in the <001> direction (parallel to the direction of construction). Tensile testing of SLM samples yielded higher yield stress, tensile strength, and elongation. On average, a yield stress of 506 MPa was obtained (296 MPa for the cast alloy). The tensile strength amounted on average to 928 MPa (591 MPa for the cast alloy). The yield strength were highest for samples that were located perpendicular to the direction of construction (0°); in comparison, the tensile strength is lowest in these cases.

2.2.5 Microstructure, Corrosion Behavior, and Hardness

Xian-Zhen et al examined the corrosive characteristics, the Vickers hardness, and the microstructure of cobalt-chrome (Wirobond C+) samples [9]. Samples were manufactured out of identical materials by means of SLM and conventional casting.

Objective: Corrosive characteristics, surface hardness, and microstructure of SLM samples were compared with samples manufactured via conventional casting.
Results: The microstructure of the casted samples exhibited a crystalline phase in dendritic alignment, as well as a solid solution matrix with the same composition. In contrast, the SLM samples demonstrated a columnar, homogenous structure without dendritic alignment. The grain boundaries have a similar composition as in the grain's core.
The Vickers hardness of the SLM samples was found to be significantly higher than in the case of the casted samples. A Vickers hardness of 458.3 HV 0.05/10 was obtained in the SLM samples, while the hardness of the casted samples was found to be 385 HV 0.05/10.
Corrosion tests showed no significant difference between the SLM and conventional samples.

2.2.6 Microstructure, Biocompatibility, and Corrosion Behavior

Hedberg et all focused on the biocompatibility and corrosion behavior of SLM samples [10]. Scan strategies (stripes, rotational, non-rotational), scan speeds, hatch spacing, and layer thickness were varied, and the CobaltChrome MP1 alloy was compared with a CoCrMo casting alloy.

Objective: The focus of attention was on the influence of the resulting microstructure during the unsteady cooling process on the corrosion behavior and the biocompatibility of SLM samples. Results: All of the samples manufactured by means of SLM were found to be completely dense. All three samples demonstrated a finely elongated, columnar microstructure independent from the scan strategy utilized. They were primarily composed of γ Phase (fcc) with a small proportion of the ε Phase (martensitic hcp). The grain boundaries have an accumulation of Cr and Mo. In contrast to casting alloys, the quick cooling process inherent to SLM prevents the formation of carbides. The latter point, as well as the accumulation of Mo at the grain boundaries, reduces the vulnerability for corrosion in comparison to casting alloys. There was little influence of the scanning strategy on the corrosion behavior.

2.2.7 Metal Powder Materials, Utilized Parameters, and Used SLM Systems

The chemical composition of the various powder materials utilized in works [5] through [10] are summarized in the following table (*Table 1*). *Table 2* shows the utilized construction procedure, as well as the parameters employed (insofar that they are known).

Table 1 Chemical composition of metal powder material for works [5] to [10]

Material	Co [%]	Cr [%]	Mo [%]	W [%]	Si [%]	Mn [%]	Fe [%]	N [%]	Ni [%]	C [%]	O [%]	N [%]	Source
Co-Cr-Mo	63	29.53	5	/	1	0.5	0.5	0.3	/	0.17	/	/	[5]
F75	Bal.	27-30	5-7	/	<1	<1	<0.75	/	<0.5	<0.35	/	/	[6]
Co-Cr-Mo	59.5	31.5	5	/	2	1	/	/	/	/	/	/	[7]
Co-29Cr-6Mo	Bal.	28.64	5.99	/	0.81	0.49	0.11	/	0.02	0.009	/	/	[8]
Wirobond C+	62.5	26	6	5	Bal.	/	Bal.	/	/	/	0.16	0.02	[9]
Cobalt Chrome MP1	60-65	26-30	5-7	/	<1	<1	<0.75	/	<0.1	<0.16	/	/	[10]

Table 2 Used SLM Systems and parameters for works [5] to [10]

SLM System & Company	Laser	Focus Diameter [µm]	Layer Thickness [µm]	Laser Power [W]	Scan Speed [mm/s]	Hatch Spacing [mm]	Source
M3 linear Concept Laser GmbH	Nd:YAG (cw)	200	40	95	200	0.14	[5]
N/A ReaLizer SLM	N/A	150-200	75	N/A	300	N/A	[6]
EOSINT-M270 EOS GmbH	Nd:YAG (cw)	200	20	200	up to 7000	N/A	[7]
EOSINT-M250 X EOS GmbH	Nd:YAG (cw)	N/A	50	75-200	50	0.1-0.3	[8]
N/A BEGO Medical	N/A	N/A	N/A	N/A	N/A	N/A	[9]
EOSINT-M270 EOS GmbH	Nd:YAG (cw)	N/A	20-40	195	535-800	0.1-0.14	[10]

2.2.8 Summary of Literature Review

The densities of the sample items obtained were close to 100% in all of the studies reviewed [5-10].

The Vickers hardness of SLM samples exceeds that of the conventionally manufactured samples. The potential cause of this finding was not named in the literature reviewed [9].

Due to the fine grain structure induced through the SLM process, greater tensile strengths and higher yield stress are attained than in the case of conventionally manufactured samples. A small degree of anisotropy can be detected in the SLM samples depending on the angle with regard to the direction of construction [6-8].

The established microstructure consists of very finely granulated γ Phase with a small proportion of the ε Phase (hcp). The metal grains expand columnar in the z direction (build direction). There is an accumulation of Cr and Mo in the grain boundaries. One study also reported precipitants with an elevated Cr and Mo content [9-10].

The superior corrosion resistance and biocompatibility found in the SLM samples in comparison to the conventionally manufactured samples results from the high thermal gradient, as well as the accumulation of Mo enriched grains. Metal release of carbides and the grain boundaries impair corrosion resistance and

biocompatibility. Quick cooling rates prevent the formation of carbides, and the accumulation of Mo at the boundaries also works against metal release [9-10].

3 Basics

3.1 Material

3.1.1 Cobalt-Based Alloys

Cobalt undergoes an allotropic transformation at cool down or heating. At temperatures below 417 °C pure Cobalt has a hexagonal close-packed (hcp) structure (ε-Cobalt). Above 417 °C, Cobalt has a face centered cubic (fcc) structure (α-Cobalt). Alloying elements like nickel, iron, and carbon act as fcc stabilizers. In contrast, chrome, tungsten, and molybdenum are hcp stabilizers and have an opposing effect. Due to the slowly proceeding phase transformation process, cobalt-based alloys mainly have a metastable fcc crystal structure at room temperature. In addition, chrome has anti-corrosive effects, because it forms a protective passive layer (oxide layer). Furthermore, the elements molybdenum and tungsten improve the corrosion resistance of cobalt-based alloys [1].

In general, cobalt-based alloys are considered to be particularly corrosion-resistant, wear-resistant, and heat-resistant. Many of the properties of cobalt-based alloys can be attributed to the crystal structure of cobalt; the solid solution solidification of chrome Cr, tungsten W, and molybdenum Mo; the formation of carbides; and the corrosion resistance due to chrome [1]. The effect of certain alloying elements are listed in *Table 3*.

According to Davis [1] cobalt-based alloys can be divided into three categories:

- High-carbon alloys developed for high wear resistance
- Low-carbon alloys for high temperature applications
- Low-carbon alloys developed for high corrosion resistance or corrosion- and wear resistance

The alloy used in this work belongs to the latter of those three groups and will be described in more detail in the subsequent chapter. Additional information with respect to the other two groups can be found in [1].

Table 3 Effect of a selection of alloying components in cobalt-based alloys [11]

Element	Effectiveness	
Fe	+	fcc stabilizer
	+	improves the workability of wrought alloys
	-	reduces strength at higher contents
Ni	+	fcc stabilizer
	+	improves the workability of wrought alloys (increases ductility due to higher stacking fault energy)
	-	reduction of strength due to high stacking fault energy
Cr	+	Cr_2O_3-layer formation; improves the corrosion resistance
	+	carbide former (mainly $M_{23}C_6$)
	-	promotes the TCP (topologically closed packed) phase formation
Mo	+	solid solution hardening
	+	carbide former (M_6C)
	-	promotes the TCP phase formation
	-	hcp stabilizer
W	+	solid solution hardening
	+	increases the solidus temperature
	+	carbide former (M_6C and MC)
	-	promotes the TCP phase formation
	-	hcp stabilizer
C	+	carbide formation
	+	fcc stabilizer
	-	reduction of ductility
	-	reduction of solidus temperature
Mn	+	deoxidized the melt and binds S
Si	+	reduces viscosity
	+	deoxidized the melt
	-	promotes the Laves phase formation, embrittlement

3.1.2 CoCrMo-Alloy According to ASTM F75 Standard

Due to high complexity and the associated expensive machining, medical implants of CoCr alloys according to ASTM F75-12 standards (F = materials for specific applications; 75 = sequential number assigned; 12 = year of original adoption) are conventionally produced as near net shape by investment casting, or, in the case of denture prostheses, milled [12].

The chemical composition and tolerances for CoCrMo alloys according to ASTM F75 standards are listed in *Table 4*.

Table 4 Chemical composition for CoCrMo alloys according to ASTM F75 standards [13]

	Co [%]	Cr [%]	Mo [%]	Ni [%]	Fe [%]	C [%]	Si [%]	Mn [%]	W [%]	P [%]	S [%]	N [%]	Al [%]	Ti [%]
Comp.	Bal.	27-30	5-7	<0.5	<0.75	<0.35	<1	<1	<0.2	<0.02	<0.01	<0.25	<0.1	<0.1
Tol.	-	0.3	0.15	0.05	0.03	0.02	0.05	0.03	0.04	0.005	0.003	0.02	0.02	0.02

The mechanical requirements according to ASTM F75 standards for CoCrMo alloys are summarized in *Table 5*.

Table 5 Mechanical requirements for CoCrMo alloys according to ASTM F75 standards [13] [1]

ASTM specification	Alloy System	Condition	Yield strength [MPa]	Tensile strength [MPa]	Elongation [%]	Elastic modulus [GPa]
F75	Co-Cr-Mo	Cast	450	655	8	248

Unfortunately, only little information is available in the literature with regard to the physical and thermo-physical properties of CoCr 2LC. Therefore, the values given in *Table 5* are taken from a data sheet [14] devised by the company 3TRPT Ltd. The data is based on SLM samples, and the chemical composition of the used material corresponds to ASTM F75 standards.

Table 6 Physical properties of CoCr 2LC alloy [14]

	As built	
Coefficient of thermal expansion	20 – 500 °C 500 – 1000 °C	$13.6 \cdot 10^{-6}$ m/m°C $15.1 \cdot 10^{-6}$ m/m°C
Thermal Conductivity	at 20 °C typ. 13 W/m°C at 300 °C typ. 18 W/m°C	at 500 °C typ. 22 W/m°C at 1000 °C typ. 33 W/m°C
Melting range	1350 – 1430 °C	
Density	8.3 g/cm³	

The chemical composition of the alloy and the prevailing boundary conditions during the casting process, for example the cooling rate, have a huge impact on the resulting microstructure. The microstructure of ASTM F75 certified casting alloys typically show a coarse dendritic fcc (α Phase) matrix with precipitates on the grain boundaries and in interdendritic regions (*Figure 2a*). In the interdendritic region and at the grain boundaries are chromium and molybdenum enriched $M_{23}C_6$ carbides, as well as a coarse lamellar (α(fcc) + $M_{23}C_6$) and a tetragonal intermetallic σ phase (*Figure 2b*). Depending on the alloy composition, M_6C carbides and metallic inclusions can occur [15].

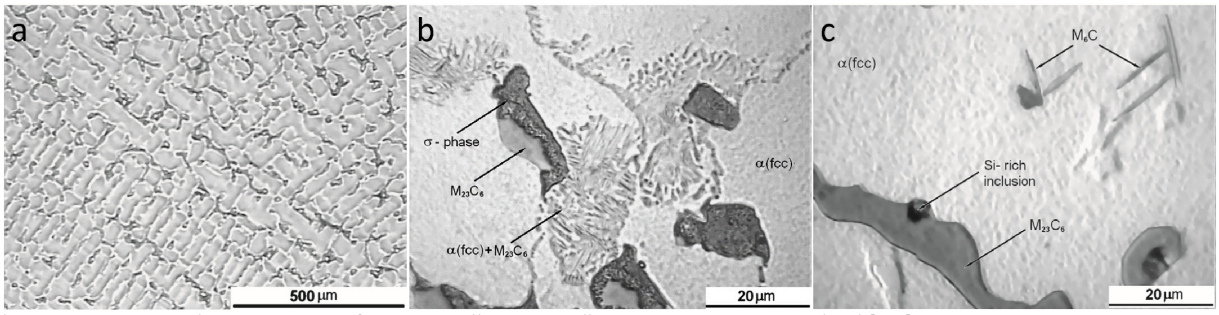

Figure 2 Microstructure of CoCrMo alloy according to ASTM F75 standard [15]

3.1.3 CoCr-2LC Powder according to ASTM F75 Standard

The powder utilized in this work is provided by the company Renishaw Ltd. The composition (*Table 7*) corresponds to ASTM F75 standards with the exception of a slight increase in sulfur content (compare with *Table 4*), which is outside of the tolerated range. The particle size distribution is 15 µm – 45 µm.

Table 7 Chemical composition of the used powder [16]

Co [%]	Cr [%]	Mo [%]	Ni [%]	Fe [%]	C [%]	Si [%]	Mn [%]	W [%]	P [%]	S [%]	N [%]	Al [%]	Ti [%]	O [%]
Bal.	27.7	5.6	<0.05	0.2	0.03	0.74	0.72	<0.03	0.002	0.002	0.16	<0.01	<0.01	0.02

3.2 Residual Stress

3.2.1 Definition

Residual stresses are stresses that exist in a material without the action of external forces, moments, and temperature gradients. Residual stresses can affect the static and dynamic properties of the material in two ways, positive and negative. Residual stresses can be subdivided into three different inherent stress conditions. A distinction is made between residual stresses of the I., II., and III. kind. The classification depends on the areas over which the residual stress occupies constant values. Residual stresses of the I. kind are called macro-residual stresses. Residual stresses of the II. and III. kind are called micro-residual stresses and nano-residual stresses, respectively. In engineering material, there is always a superposition of these three types of residual stresses present (*Figure 3*) [17] [18] [19].

- Residual stresses of the I. kind: act over macroscopic distance, meaning over several grains, and is almost constant. Arises for example due to thermal causes [20].
- Residual stresses of the II. kind: constant within a grain, but may vary from grain to grain. Cause of the residual stress in a grain are the different yield strength and different thermal expansion coefficients depending on the present phase and orientation of the observed grain [20].
- Residual stresses of the III. kind: vary over a few atomic distances and are caused by lattice defects such as vacancies, interstitials, dislocations and twins [21].

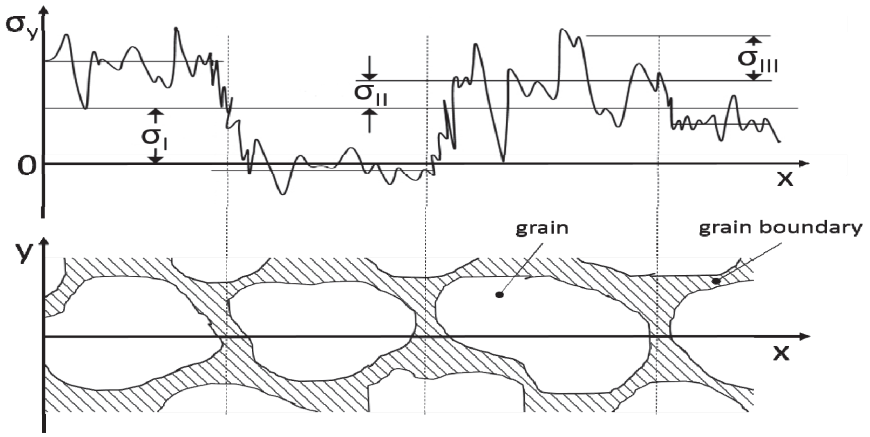

Figure 3 Superposition of residual stresses of the I., II. and III. kind (modified from [17])

The forces and moments caused by the residual stresses are always in equilibrium with each other. In parts in which residual stresses of the first kind are present, which results in a change in the equilibrium of forces and moments, there are macroscopic deviations. This is why residual stresses of the first kind are considered the most important from an engineering point of view [22]. In the studies to be subsequently described, those macroscopic deviations are used to draw conclusions pertaining to residual stresses. With a test geometry that has been developed for this particular reason (Twincantilever) and a subsequent change in the equilibrium of forces and moments, a delay in the test geometry will occur. Due to the magnitude of the delay, qualitative conclusions about the previously present residual stress state can be drawn.

3.2.2 Residual Stresses in SLM

The origin of residual stresses in SLM are due, in the first place, to constrained shrinkage of the cooling melt pool and the surrounding material. The high temperature gradients present in the SLM process instigate, similar to conventional welding, the formation of residual stresses [23]. It is generally believed that a low thermal conductivity leads to high residual stresses in SLM. Due to low thermal conductivity, the heat can only be dissipated very slowly, which leads to high thermal gradients and, hence, to high residual stresses [24]. Similarly, a high thermal expansion results in high residual stress, because while the shrinkage during cooling is very large, it is constrained by the underlying layers that have already been solidified (see cool-down phase model below) [25]. Attempts to prove both phenomena experimentally are described in [25]. A clear correlation between thermal conductivity and thermal expansion coefficient and residual stress, however, was not identifiable. It should be mentioned that some of the samples used in [25] showed a very heavy crack and pore formation. Hence, it is questionable to what extent the residual stress measurement of these samples is reliable.

A vivid and very intuitive explanation of the formation of residual stresses in the SLM process can be explained with the so-called “temperature gradient model” [26] [27] and the “cool-down phase model“ [26] [27] [3].

Temperature Gradient Model (TGM): The TGM model is based on large temperature gradients in the beam-material interaction zone. According to the TGM model, material is heated locally by the

exposure of the laser beam. This results in the expansion of the heated material. The expansion is hampered by the colder material. The result is a region exposed to compressive stress (*Figure 4a*). If the compressive stress exceeds the yield point of the material, the expansion takes place partly plastically and partly elastically. After the exposure process, cool down takes place, and thereby shrinkage of the material occurs. The shrinkage is hindered by the plastic deformation which previously occurred. This results in a zone of tensile stress in the previously exposed zone (*Figure 4b*). Since the equilibrium of forces and moments must be met, there is compressive stress present in the edge region [26] [27].

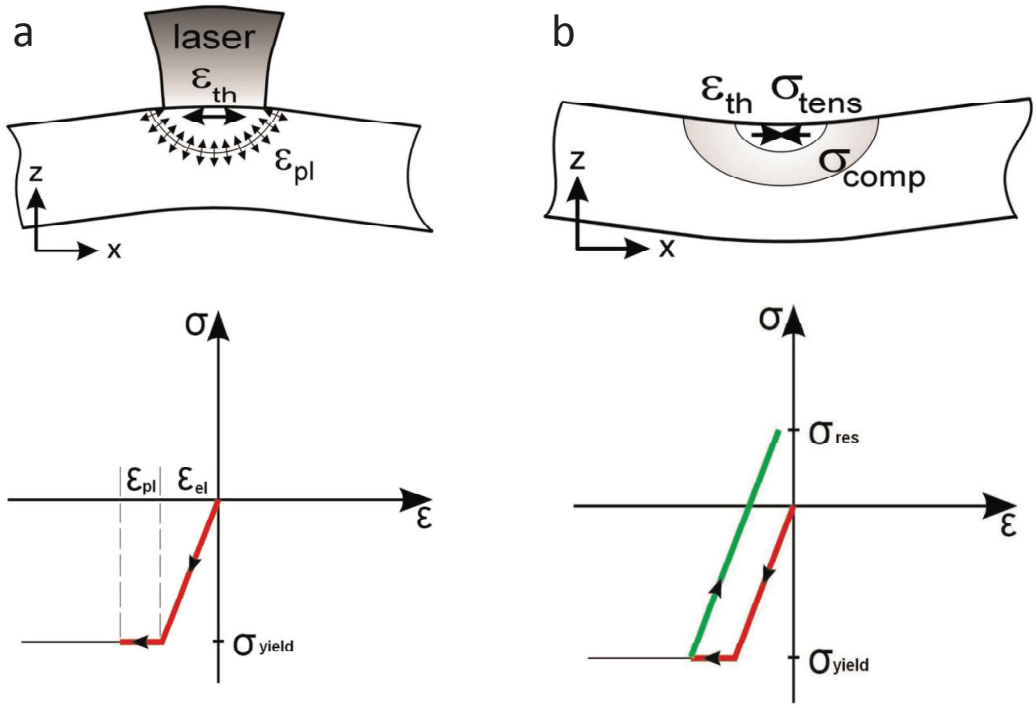

Figure 4 a) Top: stresses and deformation during heating [26]
b) Top: stresses and deformation after heating [26]
a) and b) Bottom: simplified representation of stress and strain in the irradiated zone [26]

Cool-down Phase Model (CDM): Due to the layer-by-layer stepwise building process, the currently exposed layer *n* has a different temperature than the underlying previously exposed layers. The shrinkage of the last exposed layer is hindered by the underlying layers; there is no free contraction possible. The result is a delay

due to tensile stress (*Figure 5*). The deformation of the part is always oriented in the z-direction [26] [27] [3].

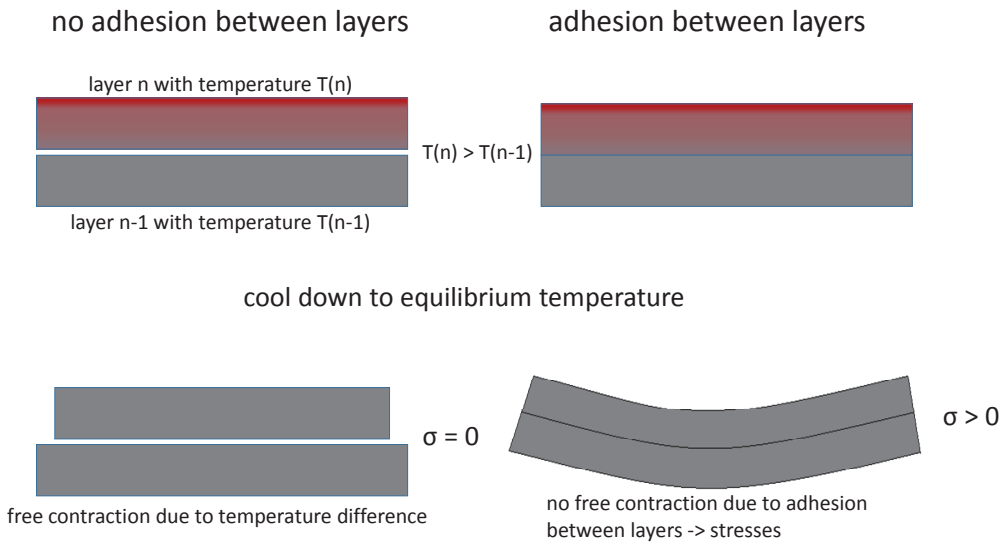

Figure 5 Schematic representation of the delay according to the CDM model (modified from [3])

3.2.3 Simplified Theoretical Model

To calculate the residual stress distribution in SLM, Mercelis and Kruth [27] and Shiomi at al [28] developed simplified mathematical models based on the CDM. Due to a few minor errors in [27] and the, therefore, difficult comprehensibility of the results, the basic principles of the simplified theoretical model are explained in this chapter. Firstly, the simplified theoretical model according to [27] is described.

A SLM part of height h_p is built layer-by-layer on a base plate of height h_b. The layer thickness of the last solidified layer is t (*Figure 6, left*). After the layer has been exposed, it cools down from the melting point to room temperature and shrinks. Thereby, tensile stress is generated in the part, as well as a compressive stress on the upper side of the base plate and a tensile stress in the lower part of the base plate. With each newly applied layer, a new stress profile will be induced into the base plate and in the underlying solidified layers (*Figure 6, right*). In addition, the following additional assumptions are made:

- The induced stress in the last exposed layer is equal to the yield stress Y, since the stress resulting from the shrinkage ($\varepsilon_{th} = \alpha\Delta T$) would exceed the yield strength of the material.
- The stress in x-direction is independent of the y coordinate.
- The classical beam bending theory (Euler-Bernoulli) holds true.
- There are no external forces.

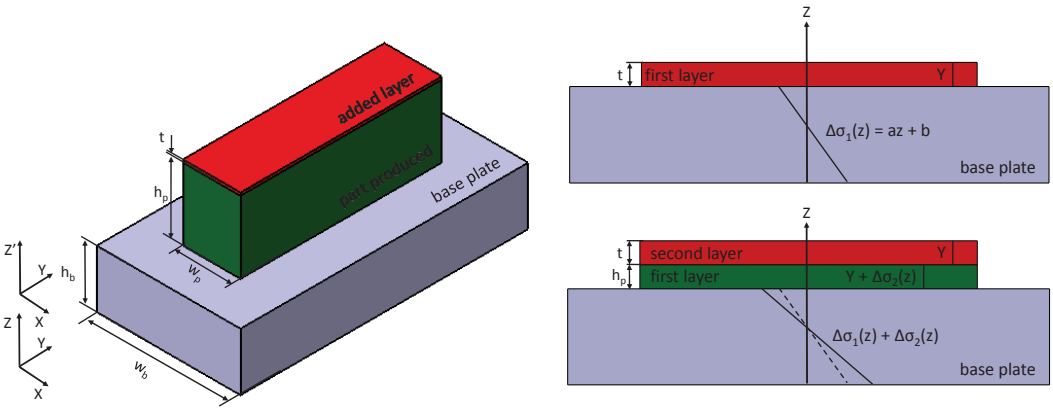

Figure 6 Left: Schematic representation of the SLM part on a base plate (modified from [27])
Right: Illustration of the resulting stress profile (modified from [27])

For each layer a linear stress function (*Formula 3.1*) is applied.

3.1 $$\sigma_{xx(z)} = az + b$$

The equilibrium of forces and moments must be met at any time. Also, no external forces are applied.

3.2 $$\int \sigma_{xx(z)} dz = 0$$

3.3 $$\int \sigma_{xx(z)} z dz = 0$$

The unknown coefficients *a* and *b* in *Equation 3.1* can be calculated by plugging *Equation 3.1* in *Equation 3.2* and *3.3*. The parameter

$m = E_b w_b / E_p w_p$ in *Equation 3.4* and *3.5* takes the different Youngs moduli of part and base plate into account.

3.4
$$\int_0^{h_b} m(az+b)dz + \int_{h_b}^{h_b+h_p} (az+b)dz + \int_{h_b+h_p}^{h_b+h_p+t} \sigma_Y dz = 0$$

3.5
$$\int_0^{h_b} m(az+b)zdz + \int_{h_b}^{h_b+h_p} (az+b)zdz + \int_{h_b+h_p}^{h_b+h_p+t} \sigma_Y z dz = 0$$

The coefficients *a* and *b* from *Equation 3.1* follow by simultaneous solution of *Equation 3.4* and *3.5*:

3.6
$$a = -6\sigma_Y t \frac{2mh_b h_p + mh_b t + h_p^2 + h_p t + mh_b^2}{4mh_b^3 h_p + h_p^4 + m^2 h_b^4 + 6mh_b^2 h_p^2 + 4mh_b h_p^3}$$

3.7
$$b = \sigma_Y t \frac{2mh_b^3 + 6h_p mh_b^2 + 3mh_b^2 t + 6h_b h_p^2 + 6h_b h_p t + 2h_p^3 + 3h_p^3}{4mh_b^3 h_p + h_p^4 + m^2 h_b^4 + 6mh_b^2 h_p^2 + 4mh_b h_p^3}$$

This calculation process is repeated again successively for each layer. The consequence is that for each new layer a stress increment is induced in the base plate as well as in the underlying layers. The result is a compressive stress in the upper part of the base plate and a tensile stress in the lower part (*Figure 7*). In the SLM part a stepwise stress distribution is introduced, wherein the maximum stress is always in the top layer due to the assumptions previously mentioned (*Figure 7*).

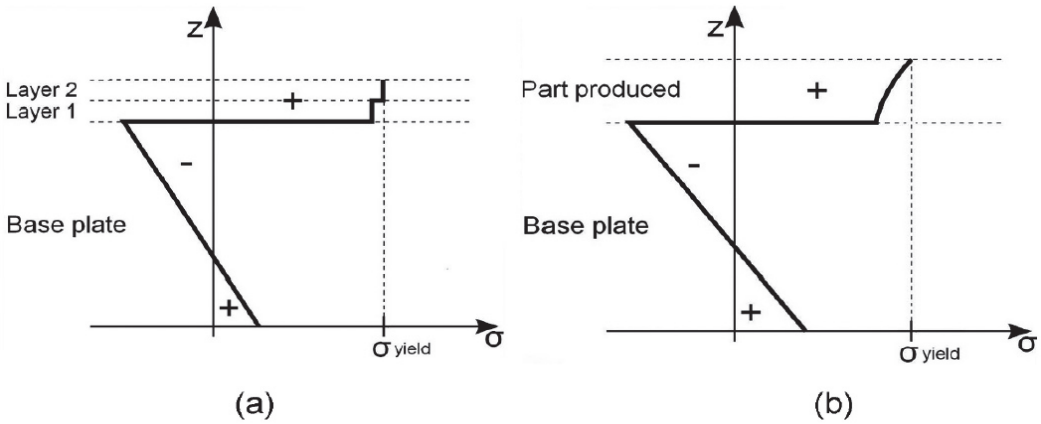

Figure 7 Example of a stress profile in the base plate and in the part according to the simplified theoretical model [26]
a) Residual stress after adding two layers on the base plate
b) Residual stress in a part after melting more or all layers

This residual stress profile was experimentally confirmed in the works of Mercelis and Kruth [27] and Shiomi et al [28]. In addition, the influence of the height of the substrate plate and the number of melted layers on the residual stress field was examined. Furthermore, the effect on the residual stress field of separating the printed part from the base plate was studied.

3.2.4 Influence of Process Parameters on the Delay due to Residual Stresses

In Kruth et al [26], Over [29], and Buchbinder et al [30], the influence of different scan strategies and process parameters on the deformation in z-direction of printed parts due to residual stresses is investigated. The materials used in the studies are Ti-6Al-4V [26], X38CrMoV5-1 [29], and AlSi10Mg [30]. The exact composition of the utilized powder materials as well as further process conditions can be reviewed in [26], [29], and [30].

Influence of Scan Strategy:

- Scan vector length and orientation: According to Kruth et al [26], the shorter the scan vector, the shorter the resulting deformation due to smaller temperature gradients. By shortening the scan vector to 10% of the original length (from 20 mm to 2 mm), a reduction of the deformation by 13% is achieved. Also, the orientation of the scan vectors has an impact on the deformation of the printed parts. The deformation can be significantly reduced (by about 59%) by a scan vector orientation in y-direction (*Figure 8a, left*) compared to a scan vector orientation in x-direction (*Figure 8b, left*). It should be noted that a change of the scan vector orientation only moves the problem to a different axis. The alternation of scan vectors layer-by-layer (*Figure 8b and c* alternating) leads as well to a significant reduction of the deformation by approximately 47% [26]. Nearly identical results were obtained in [29]. Here, a reduction of approximately 53% was achieved with scan vectors in x-direction compared to parts built with scan vectors oriented in y-direction. Due to an alternating scan strategy, a reduction in deformation of approximately 44% is achieved [29].

- Island Scanning: Another way to reduce residual stresses in SLM, according to Kruth et al [26], is a scan strategy named "island scanning" (*Figure 8, right*). The size of the island has no significant effect on the deformation. A rotation of the

scan vectors by 45° causes again a reduction in deformation in z-direction by approximately 36% [26].

- Post Scanning: Repeated exposure of the last solidified layer causes a reduction in deformation in z-direction to a maximum of 6-8%. At low scan speeds, a minimal reduction of the deformation in z-direction is achieved [26].

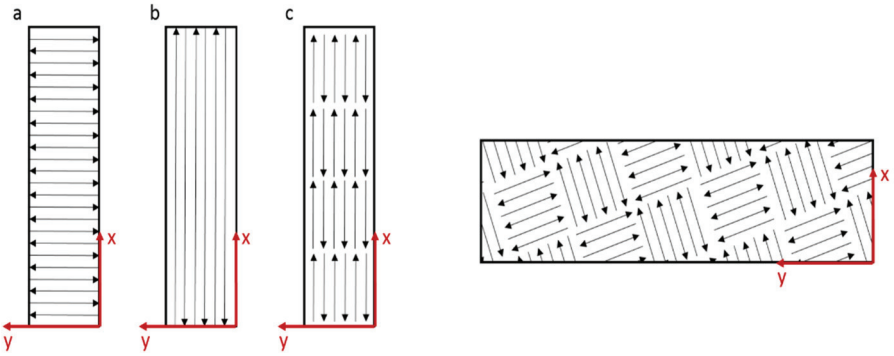

Figure 8 Left: different orientation of scan vectors.
Right: isle scan strategy

Influence of Scan Parameter:

- Preheat: A preheat temperature of 180°C causes a reduction of the deformation in z-direction by approximately 10% for Ti-6Al-4V according to Kruth et al [26]. Per Buchbinder et al [30], the deformation in z-direction of SLM samples built out of AlSi10Mg can be completely eliminated at a preheat temperature of 250°C.

- Layer thickness: By increasing the layer thickness from 30 to 100 µm, the deformation in z-direction can be reduced by 72% [29]. However, the validity of this test must be questioned, because process parameters such as the laser power and scan velocity employed were kept constant. At the same time, the layer thickness is increased, which leads to a significant reduction in the volume energy. Consequently, the porosity of the components increases. According to Vrancken et al [25], pores are stress-free areas that contribute to the relaxation of the component.

- Laser Power: By increasing the laser power from 60 to 90 W, the deformation in z-direction can be reduced by 28% [29].
- Scan Speed: Increasing the scan speed from 50 to 200 mm/s results in no significant reduction in the deformation in z-direction [29].

3.2.5 Interim Conclusion

The parameters, strategies, and their potential to reduce the deformation in z-direction due to residual stresses in SLM as used in works [26], [29], and [30] are grouped in *Figure 9*. Each graph shown in the diagram in *Figure* 9 is related to a different reference value, which makes the comparison of the potential each method has to reduce residual stresses very difficult. Nevertheless, *Figure* 9 gives a nice overview of different methods to reduce residual stresses. A depiction of the effect of scanning vector orientation and layer thickness is omitted here due to the problems described above. Furthermore, as scan velocity has only a minor impact on the deformation in z-direction caused by residual stresses, it is not presented in the diagram.

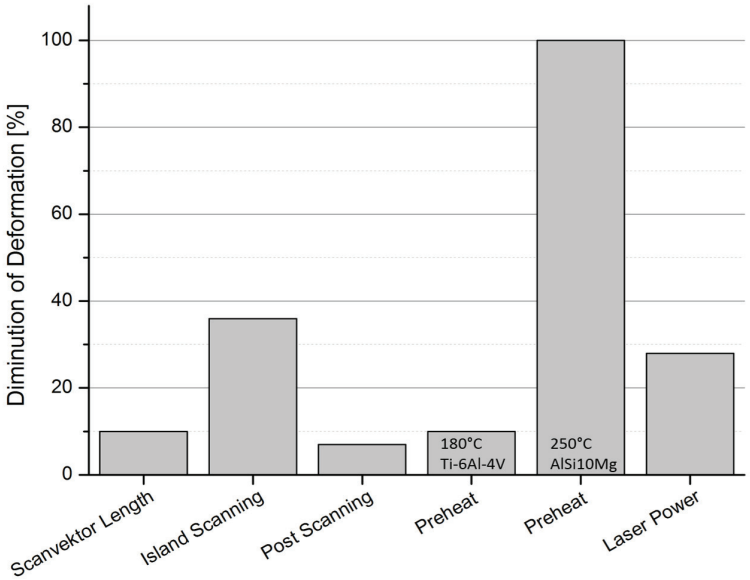

Figure 9 Comparison of different methods to reduce the deformation in z-direction due to residual stresses (with data from [26], [29], and [30]).

3.2.6 Influence of Residual Stresses on Mechanical Properties

As previously mentioned, residual stresses can affect the material properties in a positive way but also in a negative way. According to Künne [31], residual stresses mostly have a negative effect on material properties. If residual stresses in a part, for example, are just below the tensile strength, no macroscopic cracks are visible. Nevertheless, the existence of residual stresses in a part causes a reduction of loading capacity. The applied external stress may then be a maximum of $\sigma_{Load} = \sigma_{Max} - \sigma_{ResStress}$ so that no plastic deformation takes place. By looking at the equation, one recognizes the positive impact residual stresses could have, if residual stresses point in the opposite direction of the load.

3.3 Solidification and Melt Pool

3.3.1 Temperature Initiation and Distribution

During welding, as is the case with SLM, the material is locally melted. Both the weld zone and the adjacent area of the material are thermally affected. This causes a change in the microstructure of the material. Depending on the prevailing temperature and microstructure that is established, three regions can be distinguished: melting zone, heat-affected zone (HAZ), and thermally unaffected base material (*Figure 10*). In contrast to conventional welding, the entire part in SLM consists of weldment. Hence, unaffected base material is not present in SLM. The temperature distribution across the weld depends on the type of welding method (in SLM: pulsed or constant laser source), as well as on the energy introduced into the powder bed. The heat energy introduced into the material depends largely on process parameters such as laser power and scan velocity [23] [32].

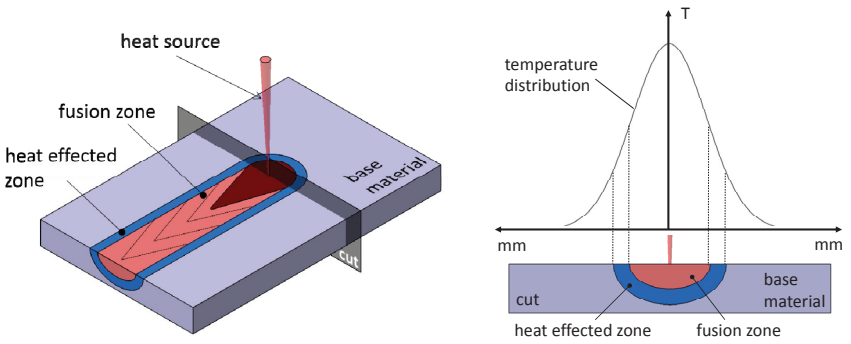

Figure 10 Fusion zone with HAZ (left). Temperature distribution across the fusion zone HAZ (right)

3.3.2 Solidification Variables

Due to the similarity between conventional welding and SLM, weld parameters such as solidification front growth rate, temperature gradient, cooling rate, and undercooling can be transferred from conventional welding to SLM. The resulting microstructure can be conditionally compared with that of a cast structure [33]. These parameters will be briefly summarized. The reader can find a more detailed description of the metallurgy of welding in the work of David and Vitek [33] and Schulze [34].

Solidification front growth rate *R*: The solidification front growth rate is the velocity with which the liquid-solid interface proceeds. The solidification growth rate is closely related to the scan velocity and has a big influence on the resulting microstructure. The relationship between the feed direction and scan speed of the heat source is:

3.8 $$|R| = \overrightarrow{v_L} \cdot \vec{n} = |v_L|\cos(\beta)$$

where β is the angle between the surface normal of the molten material and feed direction (*Figure 11a*). Consequently, the result is a varying solidification front growth rate as a function of the melt pool shape and, thus, a varying microstructure (*Figure 11*b). According to *Figure 11c*, *R* increases from the melt pool boundary until *R* reaches the value of the feed velocity *v* ($\beta = 0$). Accordingly, the solidification front growth rate *R* is zero at points A and B and reaches a maximum at point C (*Figure 11*) [33] [34].

Temperature gradient *G*: In addition to the solidification front growth rate, the temperature gradient plays a critical role in the resulting microstructure. It is very difficult to measure the temperature gradient in a weld. The temperature gradient depends mainly on the material used, the introduced heat, the welding technique, and the position within the weld [33]. According to David and Vitek [33], the temperature gradient increases if:

- the thermal conductivity is decreasing [33].
- the introduced energy density increases [33]. and/or
- the introduced heat decreases [33].

According to *Figure 11*, the temperature gradient *G*, in contrast to the solidification front growth rate, reaches its maximum at the

fusion line and has its minimum in the middle of the weld seam [34].

Cooling rate $\dot{T}$: The cooling rate is the product of solidification front growth rate R and temperature gradient G [33].

Undercooling ΔT: Undercooling is defined as the difference between the liquidus temperature of the material and the actual temperature of the material [33]. The undercooling will be discussed in more detail in *Chapter 3.3.3*.

The material-related parameters in SLM cannot be affected much if at all. Hence, various process parameters must be changed to influence the microstructure during solidification. *Figure 11b* shows the resulting microstructures depending on the temperature gradient and the solidification front growth rate R.

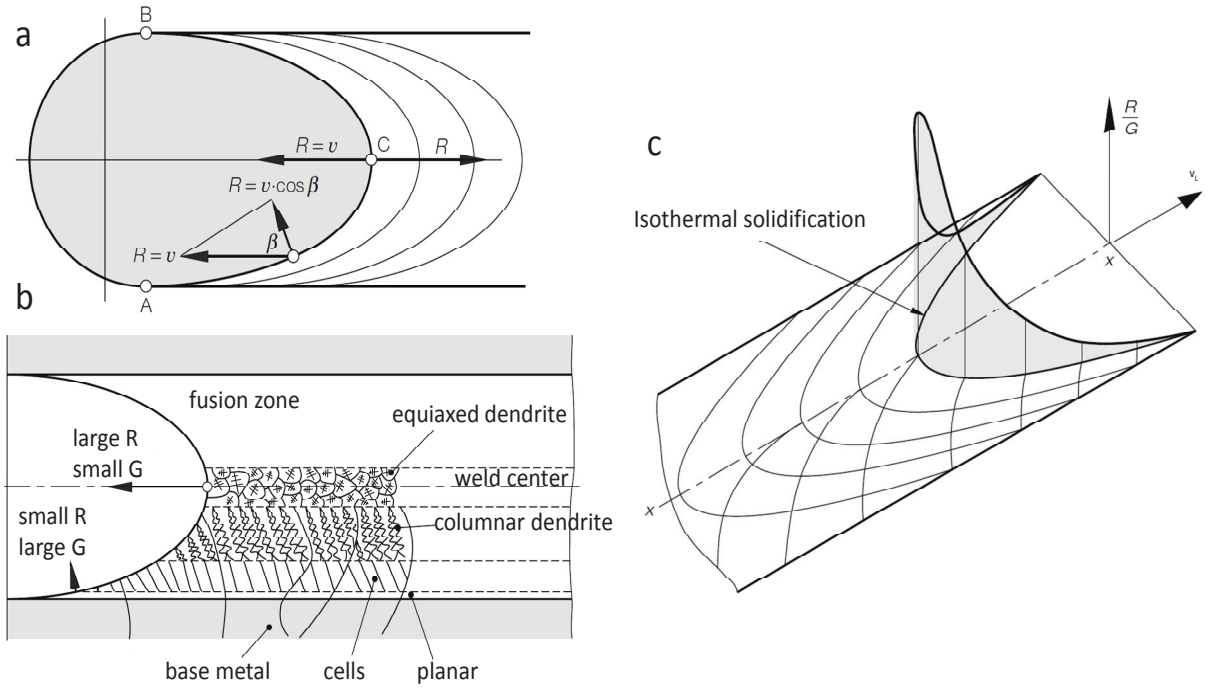

Figure 11 a) Solidification front growth rate at selected points [33]
b) Resulting weld metal microstructure due to varying solidification front rates [33]
c) Distribution of the parameter R/G along a isothermal line [34]

3.3.3 Microstructure in Welding

According to Roos and Maile [22] the activation energy ΔG (*Equation 3.9*) has to be met in order to start nucleation in the melt.

3.9

$$\Delta G = \frac{4\pi\gamma_{LK}^3 T_m^2}{3(\Delta H_m \Delta T_m)^2}(2 - 3\cos\theta + \cos^3\theta)$$

where T_m is the equilibrium melting temperature, ΔH_m is the latent heat of melting, ΔT is the undercooling, and θ is the contact angle due to surface tension between melt and substrate. As the substrate in SLM usually consists of the same material as the weld metal, the contact angle θ becomes zero. Correspondingly, the nucleation energy ΔG becomes zero as well. Hence, the nucleation in the weld occurs without the expenditure of the nucleation energy. The crystal nuclei arrange themselves according to the grains of the substrate materials (epitaxial grain growth) [23] [33] [34].

During welding, prevailing conditions like

- high temperature gradients,
- overheating of the melt pool,
- relatively small melt pool,
- high solidification front growth rates and
- non-uniform distribution of alloying elements,

are present and make a comparison with other solidification processes almost impossible. During cooling of the weld, the present segregation processes and solidification structures can be related to the undercooling. The constitutional undercooling of the melt pool results from a shift in concentration of alloying elements during solidification [23].

The solidification processes in welding can be explained by means of phase diagrams. If the temperature of the melt falls below the liquidus temperature T_0, the composition L_1 separates solid solution with a low B content c_1 (*Figure 12a*). The B atoms remaining in the melt are not distributed evenly in the liquid material immediately. Thus, the melt in the region of the phase boundary gets enriched with B atoms (*Figure 12b*). The B content of at the phase boundary drops from c_s to c_0. The result is a continuous decrease in the liquidus temperature (*Figure 12a*). Consequently, the actual temperature T_{Real} in the melt pool

substrate interface region Δx is lower than the liquidus temperature T_{Li}. The melt pool is therefore undercooled in the area Δx. The undercooling resulting from the dissolution is called constitutional undercooling. Since the temperature falls below the liquidus temperature, a spontaneous nucleation can take place in the area Δx. This is called epitaxial growth [23] [33] [34].

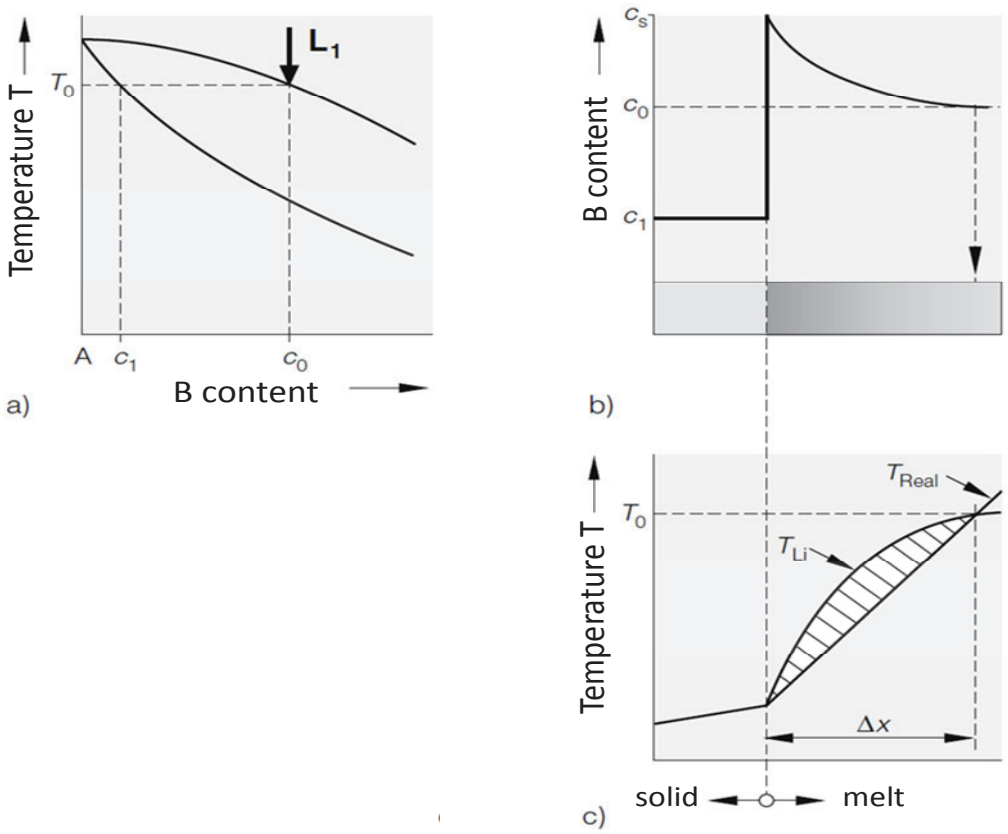

Figure 12 Constitutional undercooling of the melt [34]
a) phase diagram of a two component alloy
b) trend of the concentration c of the element B at the phase boundary
c) trend of the temperature in the range of the phase boundary

The constitutional undercooling depends to a great extent on the solidification front growth rate R and on the temperature gradient G. Based on the magnitude of G and R, significantly different microstructures can occur. If the solidification front proceeds very slowly, more B atoms can be dissipated in the melt by diffusion. This means that at a low solidification front growth rate the

constitutional undercooling is minimal and at a high solidification front growth rate the undercooling reaches a maximum. In addition, the undercooled region increases in the case of smaller temperature gradients (*Figure 13 right*). For example, at high temperature gradients and with only a small amount of dissolved alloying elements, there is no undercooled region. The consequence is a planar solidification front (*Figure 13*). Small constitutionally undercooled regions favor the formation of directed cell structures (*Figure 13*). As the magnitude of the constitutional undercooling rises, dendritic structures are more pronounced (*Figure 13*) [23] [33] [34].

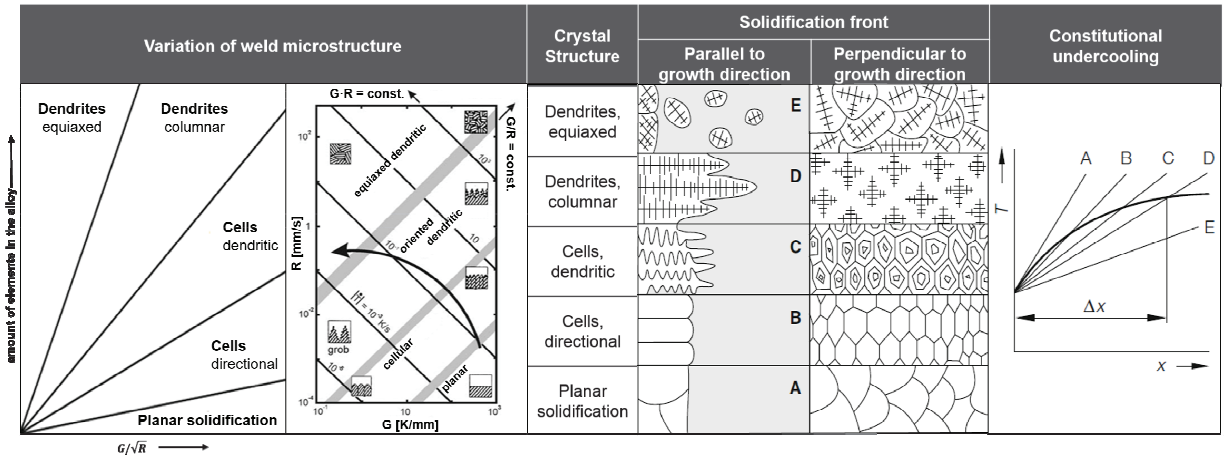

Figure 13 Influence of solidification growth rate R and temperature gradient G on the nature of the resulting microstructure [34] [35]

3.3.4 Melt Pool Shape

According to Yadroitesev et al [36] and Verhaeghe et al [37], the shape of the melt pool has a significant influence on the resulting microstructure and, hence, on the mechanical properties. The melt pool depth and the melt lens dimensions can be affected by the means of variation of the energy input in the powder, i.e. by means of variation of process parameters. Preheat temperature, laser power, and scan velocity have the greatest impact on the melt lens shape. The higher the volume of energy input, the higher are the melt pool depth and width [36] [37]. This means that melt pool width and melt pool depth increase by increasing the preheat temperature or the laser power or by decreasing the scan velocity.

3.3.5 Influence of the Microstructure on the Mechanical Properties

The solidification process influences the resulting mechanical properties significantly. In contrast to the irrevocable material composition, the solidification process can be influenced by the means of process parameter variation. Depending on the solidification process, different grain sizes and shapes occur. Furthermore, the solidification process influences the formation of precipitates and other lattice defects.

In the reviewed literature, comparable or better tensile strength properties are achieved with SLM specimens despite high anisotropic material properties. According to Kempen et al [38], this is due to the fine grain structures present in SLM specimens.

3.4 Process Parameters

The main focus in this work lies on the process parameters laser power P_L and exposure time t, or scan velocity. As well as on the volume energy, which is decisively determined by the last latter two parameters. The volume energy E_V is calculated as follows according to *Equation 3.10* (derivation in *Appendix A1*).

3.10

$$E_V = \frac{P_L \cdot t}{D_s \cdot \Delta y \cdot \Delta x}$$

where:	E_V	*volume energy*
	P_L	*laser power*
	D_S	*layer thickness*
	Δy	*hatch spacing*
	Δx	*point distance*

The parameters occurring in *Equation 3.10* and other important parameters are briefly explained in the upcoming Chapter.

Scan strategy: The exposure mode "stripes" is used in this study for the scan strategy. Thereby, the part is divided into stripes in which the width is defined by the scan vector length (*Figure 14*). After each layer is exposed, the strips rotate by 65°.

Laser power P_L: The laser power is the power that is provided to melt a powder layer. The maximal laser power of the SLM system used for this study (Renishaw) is 200 W.

Exposure time t: The exposure time is the time that the laser beam stays at a certain point.

Hatch spacing Δy: The distance between two adjacent scan vectors (*Figure 14*).

Point distance Δx: The distance between two exposure points (*Figure 14*).

Layer thickness D_s: The layer thickness is determined by the amount by which the substrate plate is lowered before the exposure begins. The laser exposure causes the power layer to melt, and the resulting density approaches approximately 100%. Consequently, the height of the melted layer compared to the powder layer is smaller. Accordingly, when applying the next layer, the powder layer thickness increases. The so-called "real" layer thickness is calculated according to Meiners [3] by *Equation 3.11*. The derivation of this equation is presented in *Appendix A2*. The fill factor required for *Equation 3.11* is determined experimentally (*Appendix A2*). For this reason, this work will distinguish between layer thickness $z = D_s$ (determined by the software and the amount by which the build platform moves down each layer) and real layer thickness d_{real} (depends on the filling factor of the used powder):

3.11

$$d_{real} = \frac{z}{a}$$

where: d_{real} *real layer thickness*
z *amount by which the build platform moves down*
a *filling factor of a powder layer*

Contour: The Contour exposure (*Figure 14*) primarily serves to improve the surface quality of generated parts. The contour exposure is mostly active in this work but not decisive.

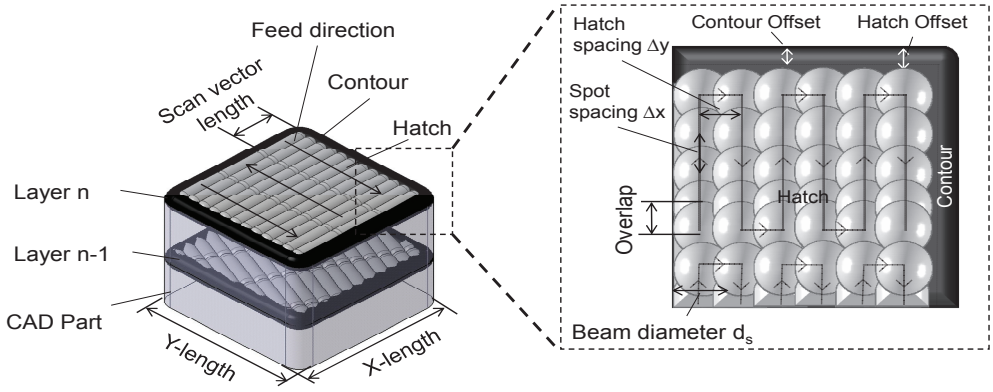

Figure 14 Schematic representation of a selection of process parameters in SLM

4 Experimental Procedure and Evaluation Methodology

4.1 SLM System

All experiments in this study were performed on the commercially available SLM machine Renishaw AM250 from the company Renishaw plc (*Figure 15*). The system is equipped with a pulsed (TTL trigger) SPI redPOWER ytterbium fiber laser, which has a nominal laser power of 200 W and beam diameter of 70 µm in focus. The wavelength is 1071 nm. The building area has a volume of 245x245x300 mm³ (X, Y, Z) and is equipped with a heater with a heat output of max 150°C. The building process takes place at an inert gas atmosphere (inert gas: Argon – 5 ppm or 99.9995% purity). The powder is applied by a silicon rod [39].

Figure 15 Left: Renishaw AM250 manufacturing system [39]
Right: Process chamber [40]

4.2 Strategic Approach

A schematic representation of the experimental line of action is presented in *Figure 16*. Basically, the work can be divided into five sections:

Section 1: First of all, a parameter window is detected with which it is possible to produce parts with a density of 99 – 100%. Concurrently, the parameters have to be process capable, which means that extensive warping my not occur during the build process. The results of *Section 1* provide the basis for all subsequent sections.

Section 2: The influence of the process parameters found in *Section 1* on the deformation in z-direction in 3D printed parts due to residual stresses is investigated qualitatively. This study uses experimental geometries developed especially for this purpose.

Section 3: Using the process parameters found in *Section 1*, single tracks are created to investigate the melt pool shape and dimensions.

Section 4: *Section 4* involves the analysis of the microstructure of the parts built with the process parameters found in *Section 1*.

Section 5: Finally, the parameters found in *Section 1* are used to generate tensile specimens to evaluate the mechanical properties yield stress, tensile strength, elongation, strain energy. An attempt is made to find a connection between the mechanical properties and melt pool shape or microstructure.

The Renishaw AM250 system enables broad user freedom in which a multitude of parameters can be varied. The parameters that can be held constant across all experiments are subsequently listed. The experimental methods, geometry build, and the evaluation will be discussed in detail in the following sections.

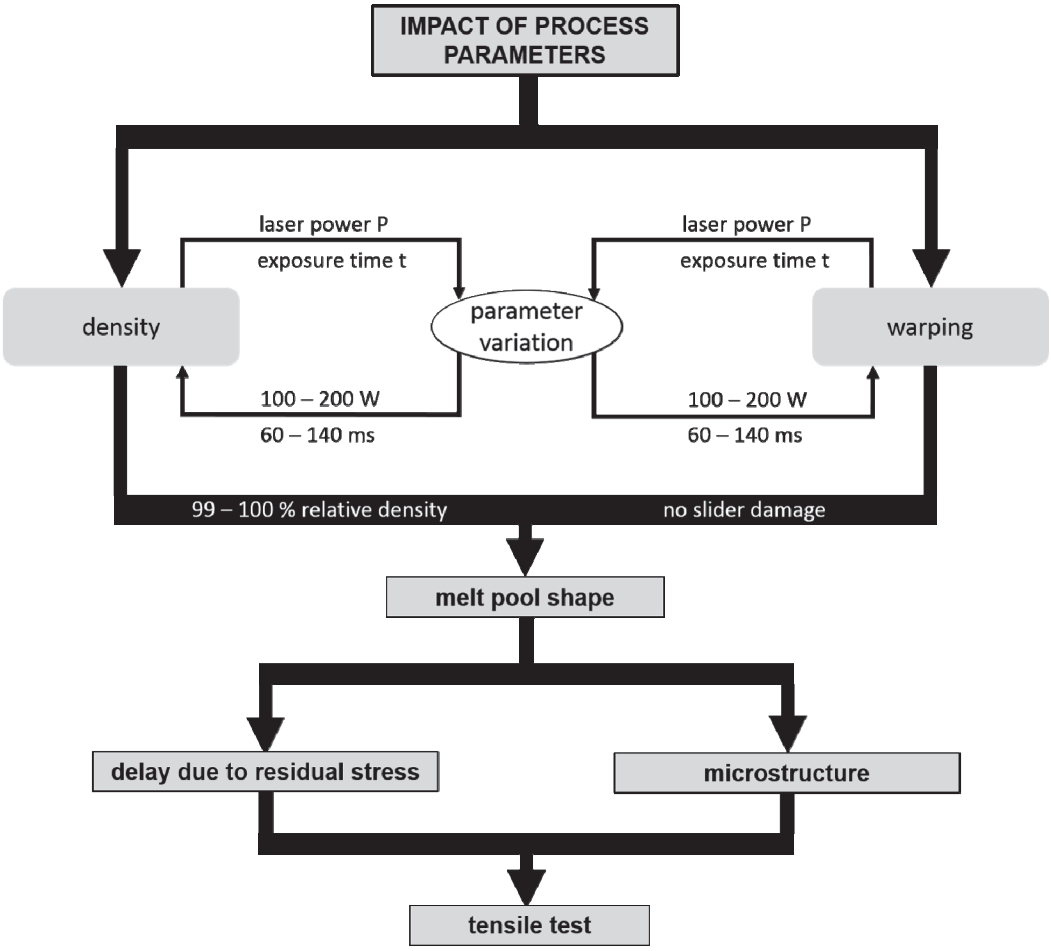

Figure 16 Schematic representation of the strategic approach used in this work

In order to keep the deformation in z-direction induced by process-related residual stresses marginal, all build constructions are conducted at a preheat temperature of $T_V = 150°C$. The layer thickness is held unchanged at a constant 30 µm. The scan strategy implemented is "stripes". In this case, the stripes have a width of 5 mm, and the individual stripes overlap one another by 0.05 µm. The hatch spacing is 125 µm. The spacing between the individual weld points is 70 µm. The processing is performed exclusively with a focused laser beam, whereby the focus offset is 0 µm. The inert gas implemented is Argon. *Table 8* depicts an

overview of the constant parameters utilized in this study. The substrate material is steel (A36).

Table 8 Overview constant process parameters

Constant Parameters	
Preheat Temperature T_V	150 °C
Layer thickness D_S	30 µm
Stripe width	5 mm
Stripe overlap	125 µm
Hatch overlap	125 µm
Point distance	70 µm
Focus offset	0 µm

4.3 Section 1: Density and Process Reliability

4.3.1 Approach

In the first section of this work, a process window will be detected. The goal is to find a variety of parameter combinations that allow one to reliably build dense parts.

The boundary conditions for the process window are determined as follows. Dense samples per definition have a density > 99%. The assessment of the process reliability is carried out by visual inspection. Process parameters are said to be unreliable if parts of a sample built with those parameters are not completely covered after the powder application. Warping during the building process can cause serious damage to the slider and can lead to abortion of the build process. Personal experience has shown that warping intensifies at overhang areas or sharp edges; hence, if warping occurs with simple cubic geometries such as those used in this section, it will probably be impossible to build complex geometries. Therefore, process parameters which lead to a sample with a density > 99 % or warping that could potentially damage the slider are discarded for all further investigations.

The density evaluation of the samples is assessed using cubic test geometries, which are built with supports on the substrate plate (*Figure 17)*. Laser power P_L and exposure time t are varied successively. Initial and final values for P_L and t are selected so that a minimal volume energy of *60% E_0* as a lower limit and maximum volume energy of *140% E_0* as an upper limit are achieved. Here, E_0 is the volume energy that is achieved with the process parameter provided by Renishaw. The Renishaw parameters will henceforth be referred to as standard parameters and are listed in *Table 9*.

In the first variation series, the volume energy is gradually escalated by increasing the exposure time from 60 to 140 µs by increments of 10 µs. The laser power remains constant ($P_L = 180$ W). The experimental geometries of this test series are called T1 – T9 and are marked red in *Figure 17*. In the second variation series, the volume energy is gradually escalated by gradually increasing the laser power from 100 W to 200 W in increments of 20 W. This time, the exposure time remains constant ($t = 100$ µs). In this case, only a maximum volume energy of *110% E_0* can be achieved, since the maximum laser power provided by the Renishaw machine is 200 W. The experimental geometries of this test series are called P1 – P6 and are marked green in *Figure 17*. The process parameters used for all of the variation steps are listed in *Table 9*. The corresponding experiment data sheets, as well as pictures of all the builds can be found in *Appendices A4* and *A5*. All test geometries are built twice to ensure reserve for the case it is needed.

Table 9: Process parameters used for the first build (corresponds to Figure 17).

Nr.	E [J/mm³]	≈E [% E_0]	t_{exp} [ms]	P_L [mm]	Nr.	E [J/mm³]	≈E [% E_0]	t_{exp} [ms]	P_L [mm]
T1	41.1	60	60	180	P1	38.1	60	100	100
T2	48.0	70	70	180	P2	45.7	70	100	120
T3	54.9	80	80	180	P3	53.3	80	100	140
T4	61.7	90	90	180	P4	61.0	90	100	160
T5	68.6	100	100	180	P5	68.6	100	100	180
T6	75.4	110	110	180	P6	76.2	110	100	200
T7	82.3	120	120	180					
T8	89.1	130	130	180					
T9	96.0	140	140	180					

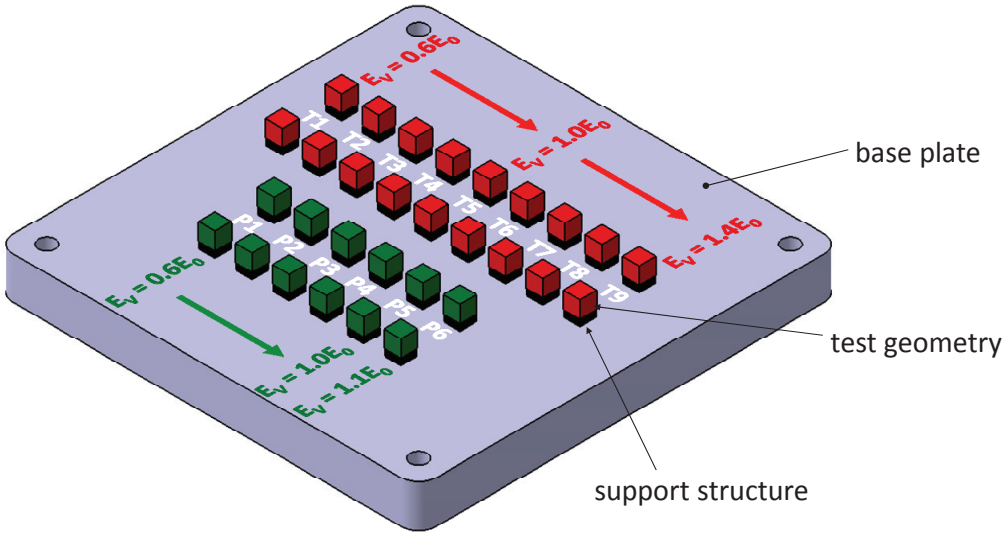

Figure 17 Arrangement of samples for the parameter variation on the base plate
Red: Exposure Time variation, P_L = const.
Green: Laser Power variation, t = const.

4.3.2 Sample Dimensions and Sample Preparation

The experimental geometries are 10x10x10 mm³ cubes built on 4 mm supports (*Figure 18*). Since preheat is used, the supports possess comparatively large wall thickness to ensure best possible heat transfer between substrate plate and part. For the same reason, the predetermined breaking points of the support structure are not segmented but continuous. The exact dimensions of the support structures and test geometries are given in *Appendix A6*.

After completion of the build, the samples are separated from the build plate by hammer and chisel, and the support structures are removed. The samples are cut in the middle, parallel to the build direction, using a water-cooled cutting blade (*Figure 18*). One half is again separated perpendicular to the build direction (*Figure 18*). Both parts are embedded in epoxy resin for microscopic analysis. The density analysis is performed on the cross-cut that was parallel to the build direction. After embedding, the cut surface is grinded and then polished for examination under the light microscope. The grit size of the emery paper used is gradually reduced from coarse to fine (grid size in µm: 80, 120, 240, 600, 800, 1200, 2400). This is followed by a diamond polish of the cut surface. The polishing cloths employed (by Struers) are listed from coarse to fine: MD-

Dur, MD-Mol, and MD-Nap. The polishing cloths are used in combination with a 9 µm, 3 µm, and 1 µm diamond suspensions, respectively.

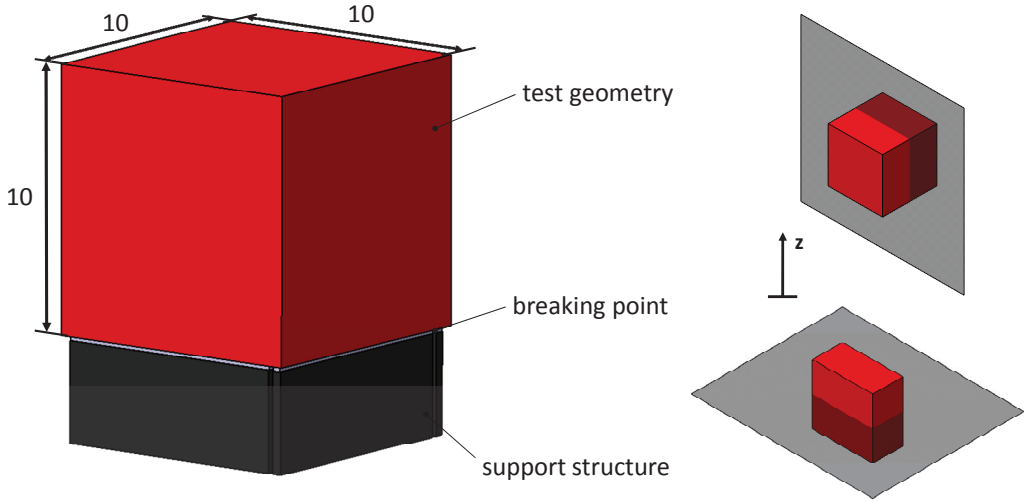

Figure 18 Experimental geometry (left) and cutting plane for analysis (right)

4.3.3 Evaluation Methodology

The density analysis is carried out by means of an optical light microscope (LEICA DM 4000 MLED). For each polished cross-section, nine images are made at 50x magnification. Thus, 45% of the cross-section are measured. Three images are taken in the upper section, the midsection, and the lower section of each sample, respectively (*Figure 19*). In this way, it is possible to additionally investigate the influence of preheating on the density with increasing build height. The software used to capture the images is LAS V4.5 Leica (basic version), and the images are stored in *.tiff* format. The evaluation is performed using the image analysis software *ImageJ 1.48v*. To determine the density, the picture is reduced to an 8 bit one color channel. Then, the picture is separated into light and dark areas in accordance with pre-established thresholds. The dark areas indicate defects, and the light areas represent regions of dense material (*Figure 19*). The density can thus be determined by the ratio of dark to light areas (*Equation 4.1*).

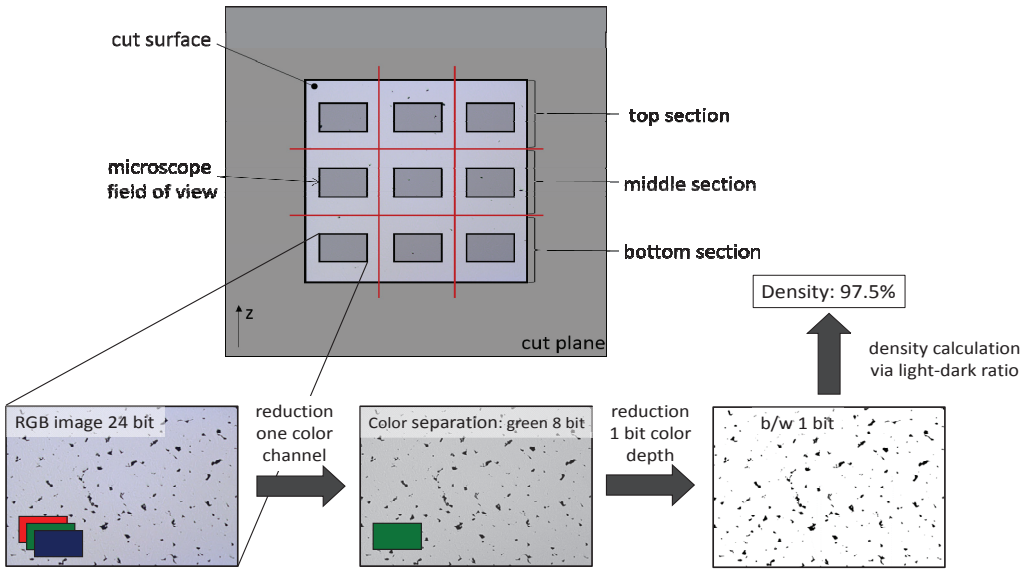

Figure 19 Schematic representation of the density analysis with *Image*J

4.1

$$\rho_{rel} = \frac{\Delta A}{A} = \frac{A - A_{black}}{A} \cdot 100\%$$

where: A *total area of the image*
A_{black} *area of pores*
ρ_{rel} *relative density*

The accuracy of this measurement method is determined by the contrast resolution, meaning the accuracy with which the software can separate between light and dark areas. The error of measurement is, therefore, dependent on the length of the lines separating light and dark areas. The length of those lines is, in turn, dependent on the porosity of the specimen. Empirical studies by Meiners [3] on samples with different densities have shown that the measurement error $\Delta\rho$ can be described in sufficient detail by the equation 4.2.

4.2

$$\Delta\rho_{measured} = \frac{1}{10}(100\% - \rho_{measured})$$

From this equation, it is apparent that the measurement error decreases with increasing density of the samples and is negligible as the density approaches 100%.

4.3.4 Interim Results

This section is a foretaste of the chapter "Results". However, this is necessary, because the results of the investigations carried out in *Section 1* for density and process reliability form the basis for further experiments and studies. The results found in *Section 1* are summarized in *Table 10*. A justification for the choice of these parameters can be found in the chapter "Results". The process parameters listed in *Table 10* are used for all the following builds.

Table 10 Process parameters found in Section 1

Nr.				E [J/mm³]	≈E [% E_0]	t_{exp} [ms]	P_L [mm]
T1	B1	S1	1	61.0	90	100	160
T2	B2	S2	2	68.6	100	100	180
T3	B3	S3	3	76.2	110	100	200
T4	B4	S4	-	61.7	90	90	180
T5	B4	S4	-	75.4	110	110	180
Twincantilever	Bridges	Single Tracks	Tensile Blocks				

4.4 Section 2: Melt Pool Shape

4.4.1 Approach

In the second section, single tracks are generated based on which the meld pool shape is investigated.

Due to the difficulty inherent to the change in layer thickness during the build process (described in *Chapter 3.4*, subsection: Layer thickness), the filling factor of the powder is experimentally determined (*Appendix A2*). Then the real layer thickness can be calculated by means of *Equation 3.11*. Subsequently, a mini substrate plate is built (*Figure 20*). The mini base plate has the

greatest build height on the base plate. After the build is finished, the surface of the mini base plate is the only part not covered by powder. The build platform is lowered manually by the value calculated with *Equation 3.11*. This is followed by manual powder application and the generation of the single tracks on top of the mini base plate. The arrangement of the single tracks, as well as their position on the mini base plate, is shown in *Figure 22*.

4.4.2 Sample Dimension and Sample Preparation

In *Section 2*, single tracks are printed, which are used to evaluate the melt pool shape depending on the process parameters. Finally, the melt pool shapes of the single tracks are compared with those of the last melted layer of the cubic specimens built in *Section 1*.

The preparation of the single tracks is analogous to the preparation of the cube geometries in *Chapter 4.3.2*. After the build is completed, the mini base plate is separated from the base plate and cut in the middle. One half is embedded in epoxy resin, grinded, and polished as described previously. In order to make the melt pools visible, the etching is carried out with 5 ml HNO_3, 200ml HCl, and 65g $FeCl_3$. The samples are immersed for a few seconds (Figure *20*). The etching must be performed within a few hours after polishing. Otherwise, an oxide layer is formed which protects the microstructure of the sample from etching.

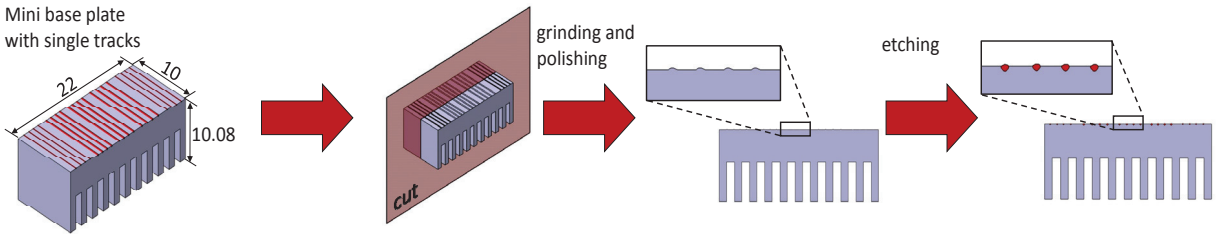

Figure 20 Test geometry for single tracks (left) and preparation for melt pool analysis (right)

4.4.3 Evaluation Methodology

The evaluation of the melt pools is performed by an optical light microscope and the image analysis software *ImageJ*. First, the melt lens is cut free and separated from the rest of the image (*Figure* 21). In order to distinguish the characteristics including shape of

the various melt pools, the melt pool area of the lenses, the width in the x-direction, and the height in the y-direction are measured. The x-axis is in this case defined for each melt lens and is congruent to the substrate material. The y-axis is centered on the x-axis at a 90° angle (*Figure 21*). Furthermore, circularity, roundness, and solidity of each melt pool are measured. The description and explanation of theses parameter can be found in *Appendix A3*. For each parameter combination, four melt pools are analyzed.

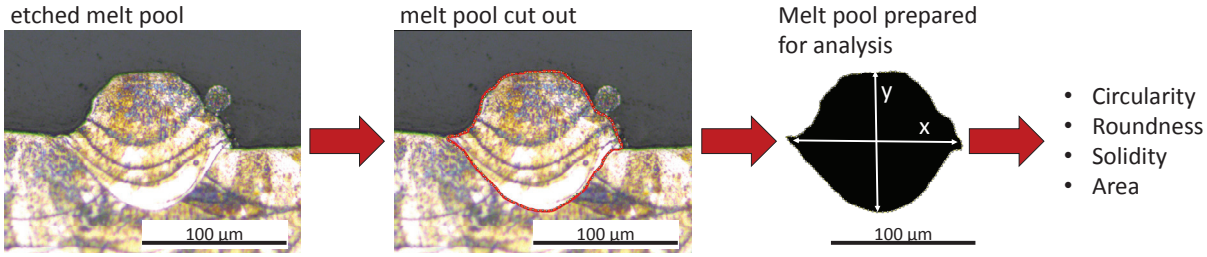

Figure 21 Schematic representation of the melt pool analysis by means of the software *ImageJ*.

Finally, the cubic samples in *Section 1* are prepared and evaluated in the same way. The relatively large hatch spacing allows for a good view of the melt pools of the last layer.

4.5 Section 3: Delay Due to Residual Stresses

4.5.1 Approach

The deformation due to residual stresses induced during the build process is studied. The study is performed on parts designed especially for this reason. The results are qualitative in nature. The mini base plate discussed in the previous chapter is also built on the same plate for organizational reasons. The build plate with all the samples used in this section is shown in *Figure 22*. Pictures of the build plate can be seen in *Appendix A5*.

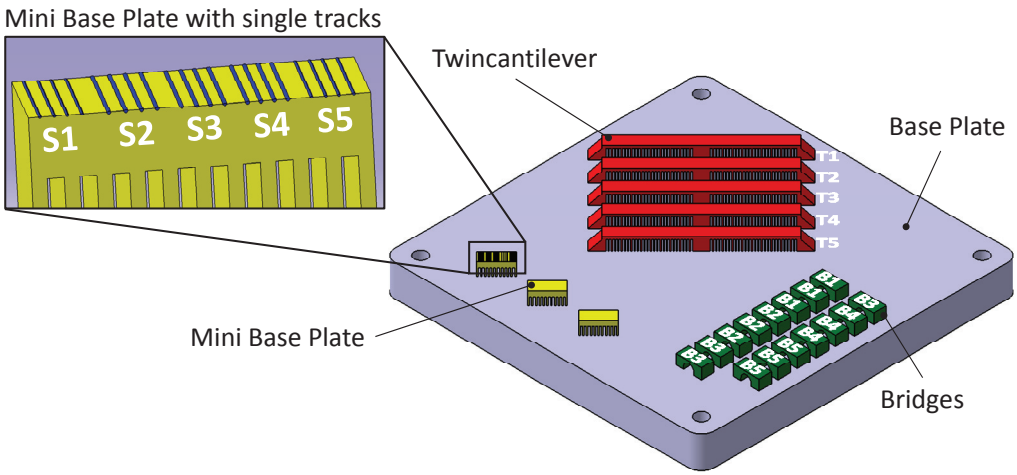

Figure 22 Build plate with the samples used in *Section 3*: Twincantilever (red), Bridges (green), and Mini Base Plate (yellow).

To make the deformation due to residual stresses that is induced in the part during the SLM process visible, so called "twincantilevers" (*Figure 23*) and "bridges" (*Figure 24*) are printed. The exact dimensions of the geometries are given in *Appendix A6*. For both experimental geometries, the goal is to be able to draw a conclusion as to the level of the prevailing residual stresses present in the part by measuring the deformation of the part. Since the available space in the substrate plate is limited, only one twincantilever can be built per process parameter combination. After completion of the build, the height of the un-deformed twincantilevers are measured. Then, the solid twincantilever arms are detached from the supporting structure via wire EDM. The twincantilever arms bend upward due to residual stresses and are measured again (*Figure 23*).

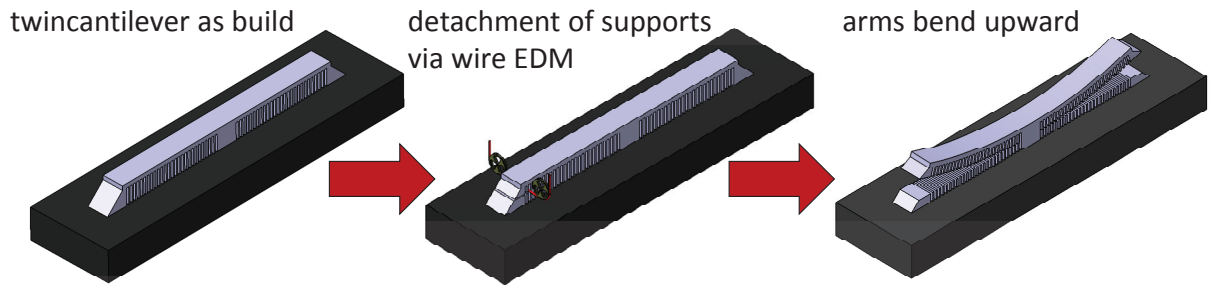

Figure 23 Schematic view of the Twincantilever approach.

The "Bridge Curvature Method" (BCM) is another very similar and also qualitative approach. This method is employed in [26]. As with the twincantilevers, one can draw conclusions as to the residual stresses present by the level of distortion of the parts. For this reason, bridge geometries are built on the substrate plate. Following the end of the build process, the bridges are completely separated from the substrate plate. This constitutes an interference in the equilibrium of forces and moments, which leads to a distortion of the bridge (*Figure 24*). The delay is measured and applied to a stress-free part by means of FEM software. The resulting stress state provides qualitative information of the residual stresses present in the part before deformation.

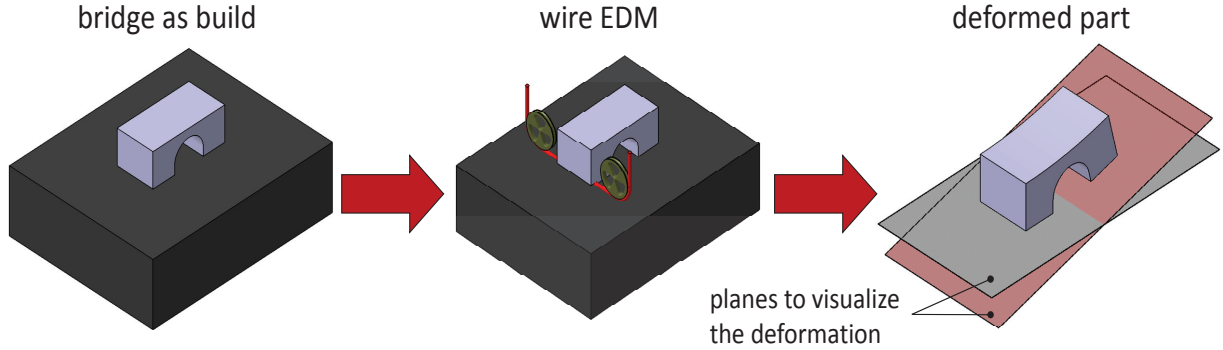

Figure 24 Schematic view of the Bridge Curvature Method (BCM).

4.5.2 Sample Dimensions and Sample Preparation

The central element of the twincantilever is the horizontal bar (*Figure 25*). During the build process, the horizontal bar should not move in position. Therefore, triangle blocks are attached to the ends of the twincantilever to avoid distortion of the component during construction. The beam thickness is 2 mm. Personal experience has shown that this is a good compromise, on the one hand, to produce an area moment of inertia that is not too large and, thus, to ensure a significant upward bend. On the other hand, a sufficiently large area must be provided in order to avoid the present state of residual stress exceeding the tensile strength of the twincantilever.

The dimensions for the bridge geometries are taken from [26]. In [26], reproducibility with respect to distortion of the parts as a function of the bridge dimensions is examined. The bridge geometry found to have the maximum reproducibility is used in this work (*Figure 25*).

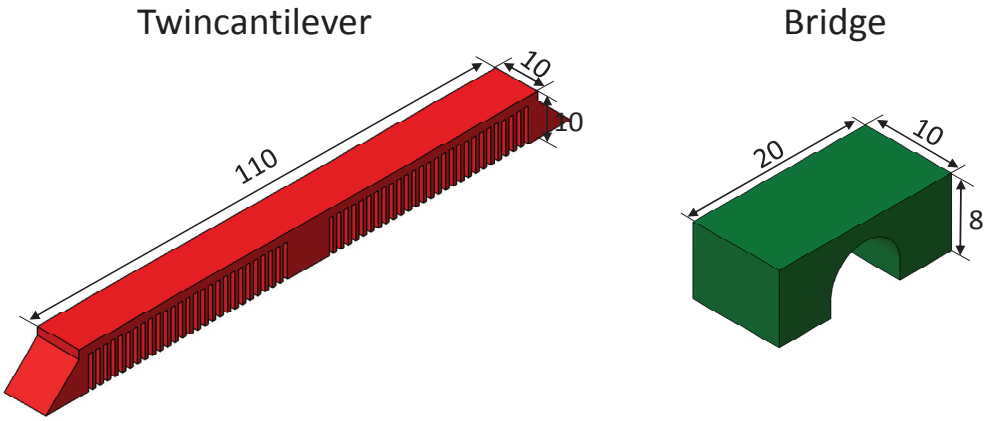

Figure 25 Experimental geometries used in *Section 3*: Twincantilever (left) and Bridge (right).

4.5.3 Evaluation Methodology

The first measurement of the un-deformed twincantilevers takes place right after the build is completed. For this purpose, a 3D coordinate measuring system called *FaroArm* by the company FARO is used. The twincantilevers are scanned contactless. The software *Geomagic Control 2014.1.0* is used for measurements. A schematic view of the measuring point or measuring plate is presented in *Figure 26.* Measured is the average z-position over the entire twincantilever width with reference to the substrate plate (*Figure 26*). The height in z-direction is measured at six positions in intervals of 10 mm along each side of the twincantilever arm (*Figure 26*). The difference in the measured values before and after separation of the supports is the resulting measure of the deformation in the z-direction. The values obtained will be summarized graphically in a diagram to be found in the "Results" section. The measurement of error specified by the manufacturer is accurate within 50 µm and is therefore more than sufficient for the purposes of this study.

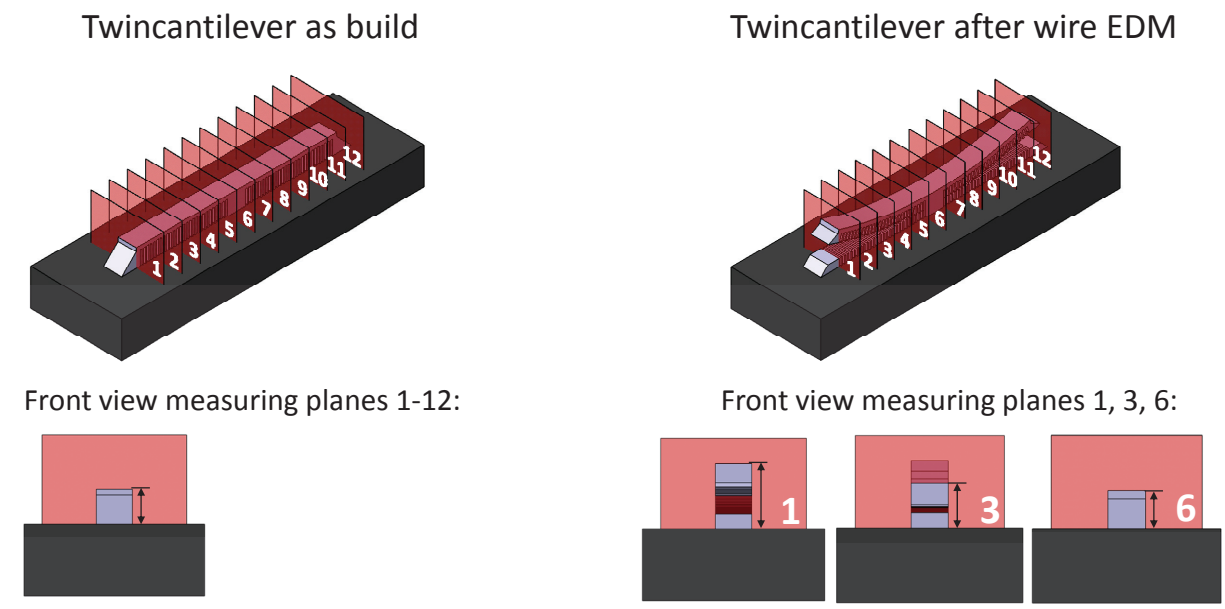

Figure 26 Schematic representation of the evaluation of the twincantilever
Left: Before wire EDM of the supports
Right: After wire EDM of the supports

In contrast to the twincantilevers, the bridges are scanned in only once, specifically after separation from the substrate plate (i.e. in the deformed state). The measurement system used is again *FaroArm*, and the software to measure the distortion is again *Geomagic Control*. The unformed CAD component is used as a reference. The measured angle between the bridge pillars is transferred to the un-deformed part by the FAE software *Abaqus*. As a result of the bending, a compressive stress acts on the upper side of the bridge and a tensile stress on the lower side. The difference between the compressive und the tensile stress is a qualitative measure for the amount of the residual stress state present in the part before the deformation took place.

4.6 Section 4: Microstructure

4.6.1 Approach

In *Section 4*, the influences of the various parameters included in the parameter window are investigated in relation to the microstructure. For the microstructure investigation, the same samples are used as in *Section 1* (*Figure 17*) for the density measurement. For a more detailed description of the parameters

used, as well as the orientation of the samples on the substrate plate, see *Chapter 4.3.1*. By means of microscopy, the microstructure of the etched specimen is studied. The cross-sections are examined with an optical microscope and a scanning electron microscope (SEM). Electron backscatter diffraction (EBSD) is used in order to obtain clear conclusions as to the grain shape, crystal orientation, and grain boundaries.

4.6.2 Sample Dimensions and Sample Preparation

The dimensions of the samples, as well as the preparation of the cross-sections are described in detail in *Chapter 4.3.2* and are applied unchanged in this section. To make the microstructure and the melting traces for subsequent light microscopy and SEM visible, the cross-sections are polished and etched with 100 ml HCl and 5 ml H_2O_2 (30%) (immersion time ca. 10 s). Prior to examination by SEM, the sample is sputtered with a thin carbon layer in order to prevent charging of the sample.

The preparation for the EBSD analysis is performed as described in *Section 4.3.2*. In order to guarantee the smoothest possible surface for EBSD analysis, the last polishing step is an oxide polish with colloidal silica.

4.6.3 Evaluation Methodology

Light Microscope: By means of optical microscopy (LEICA DM 4000 MLED), the cross-sections parallel to the build direction (z-x-plane) and normal to the build direction (x-y-plane) are examined.

Scanning Electron Microscope (SEM): Similar to the description under "Light Microscope" above, two cross-sections are examined for each sample: one cross-section parallel to the build direction and one normal to the build direction. In comparison to optical microscropy, examination with SEM has the advantage that larger magnifications are possible. This allows insight into the microstructure of the samples and inferences as to the solidification behavior, as well as conclusions based on solidification parameters such as the temperature gradient and solidification front growth rate (see Chapter *Basics*). The microscope used is a HITACHI S-4800. The accelerating voltage is 15 kV, and the probe current is 15 µA.

Furthermore, an EDS analysis was performed to determine the elemental composition of the microstructure. Special emphasis is

placed on the main alloying elements Cr and Mo. The analysis of the elemental composition of the transverse cross-section takes place at the cellular grain boundaries and is centered within the cellular grains (*Figure 27*). There are three measurements performed in the intracellular region and in the cellular boundary, respectively (*Figure 27*). In addition, the elemental composition of the complete image is determined as a reference. The software used for this purpose is *EDAX Genesis*.

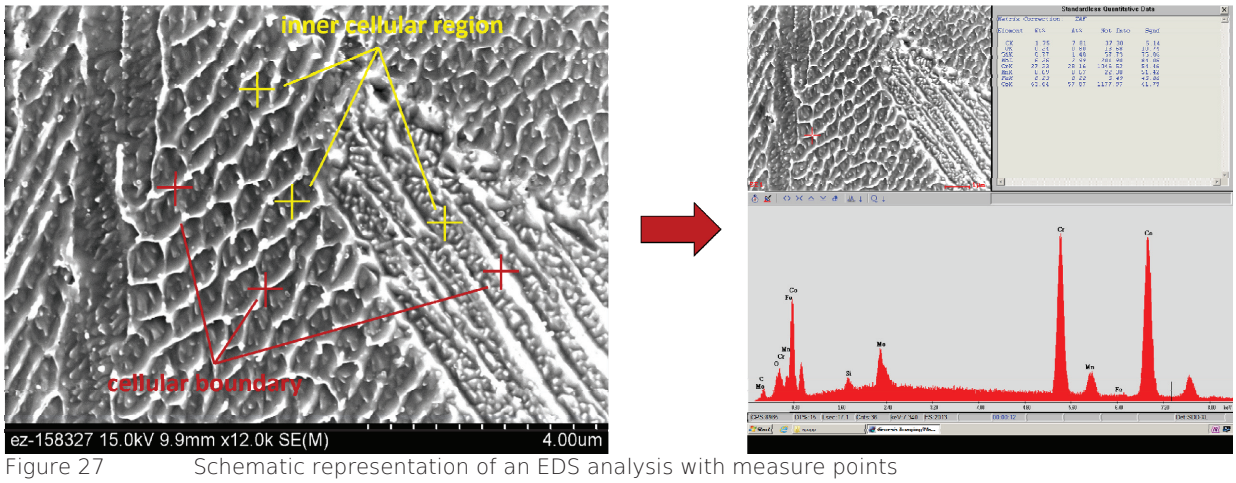

Figure 27 Schematic representation of an EDS analysis with measure points

EBSD and Grain Size: Due to the high expenditure of time entailed, only the cross-section parallel to the build direction is investigated via EBSD. The microscope used is JEOL JSM-6500F. Since the image size should exceed the height and width of the melt pool, the spot size is approximately 150x150 µm². The accelerating voltage is 15 kV, and the probe current is 4 nA. A step size of 0.3 µm was found in this study to offer a good compromise between relatively high resolution and an acceptable measuring time. The confidence interval is always greater than 0.3. The software *Orientation Imaging Microscopy v7* is used to create inverse pole figure maps and unique grain color maps. In addition, the grain size is measured.

Finally, the measurement of the grain size according to the ASTM E112 standard is performed by means of the line intercept method. The cross-sections are measured in the x- (horizontal) and y- (vertical) direction by means of a freely available *Matlab* code [41].

For this purpose, the unique grain color map image recorded by means of EBSD is used. Similar to the density evaluation in *Chapter 4.3.3*, the grain boundaries are determined by the software according to the difference in contrast. First, the RGB image is reduced to an 8 bit (HSB stack) image by the means of the Software *ImageJ 1.48v*. The grain boundaries are turned into solid black lines by the *ImageJ* plugin "Edge Detection". For the edge detection, a Canny-Deriche filter is used with an alpha value of 0.3. The final analysis of the grain size is carried out with *Matlab*. For this purpose, the image processed in *ImageJ* is loaded into *Matlab* GUI. Then, 10 grid lines in x- and y-direction are placed over the image. The intersection points of the lines and with the grains are marked. The software calculates the grain size, the number of grains, and the cumulative distribution of grain size (*Figure 28*).

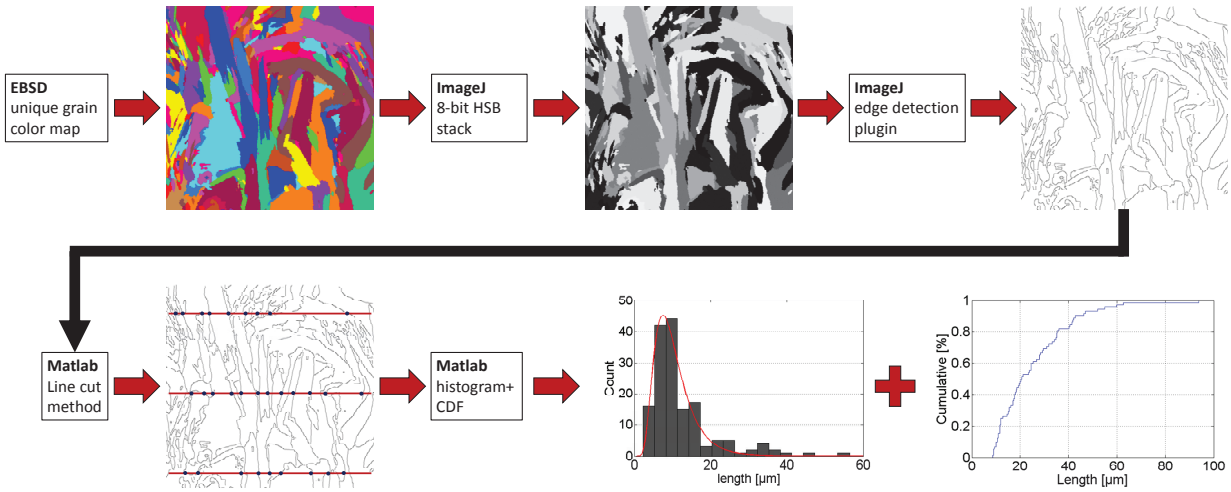

Figure 28 Schematic view of grain size measurement with *Matlab* and *ImageJ*

4.7 Section 5: Tensil Test

4.7.1 Approach

In *Section 5*, tensile specimens are built by means of the parameters from the parameter window (*Section 1*). These serve for the analysis of mechanical properties such as yield stress, tensile strength, elongation, and strain energy. For each parameter combination, three specimens are built in three different build

directions (*Figure 29*). The corresponding experimental data sheet can be found in the *Appendix A4*.

To ensure a reliable construction, massive blocks are build. The tensile specimens are machined out of those blocks later on. To identify possible anisotropy of the sample with relation to the build direction, blocks of different angles (0°, 45°, and 90° to the build direction) are built. After completion of build, the tensile blocks are put into a machine shop where the final shape is acquired by means of wire EDM and milling.

Due to their relatively large height of 75 mm and volume, the building of standard tensile specimens would usually require more than ten days. However, this is not possible within the realm of this study because of organizational and scheduling reasons. Consequently, some of the parts must be suppressed. To save as much time as possible, the parts used for the investigation of the influence of the exposure time are suppressed at a build height of 3.8 mm. This reduces the construction time from approximately ten days to approximately five days. Thus, instead of 45 tensile specimens, only 27 are built. The tensile test specimens for the investigation of the effect of exposure time on the mechanical properties are therefore omitted.

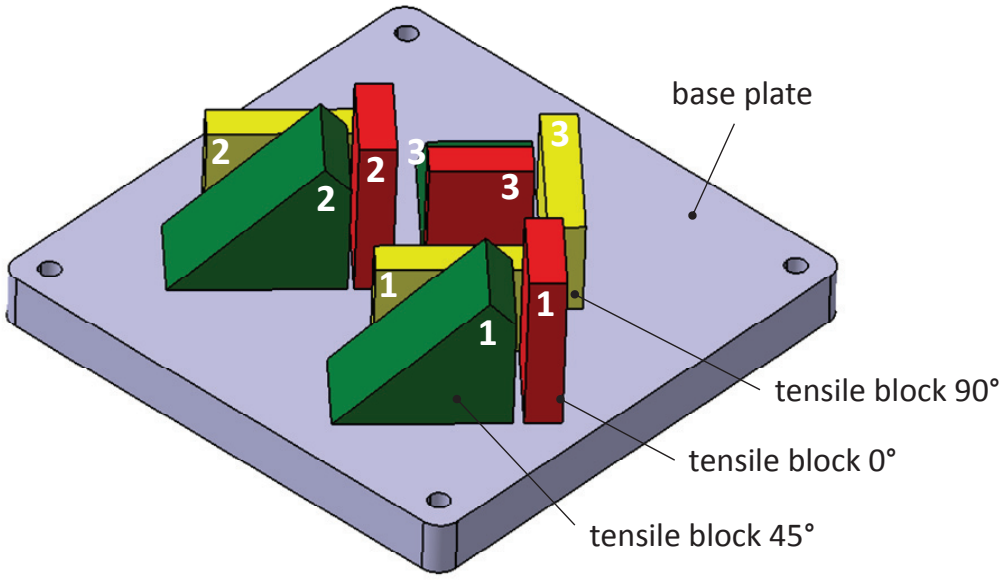

Figure 29 Arrangement of samples for the tensile blocks on the base plate

4.7.2 Sample Dimension and Sample Preparation

The dimensions of the tensile blocks are demonstrated in *Figure* 30. Tensile blocks are built parallel to the build direction at a 0° angle, at a 45° angle to the build direction, and at a 90° angle to the build direction. Detailed dimension data is provided in *Appendix A6*. After completion of the build construction, tensile specimens are manufactured from the tensile blocks according to standards E8M – 04. According to standards, the required gauge length of the tensile specimens is 75 mm. With regard to the SLM process and the associated long build times, this is not practical. Hence, a proportional tensile specimen with a gauge length of 24 mm is used instead. The total length of the tensile specimens is dependent on the tensile test machine used for the evaluation and amounts to 72 mm. Detailed dimension data pertaining to the final shape of tensile specimens are to be found in *Appendix A6*.

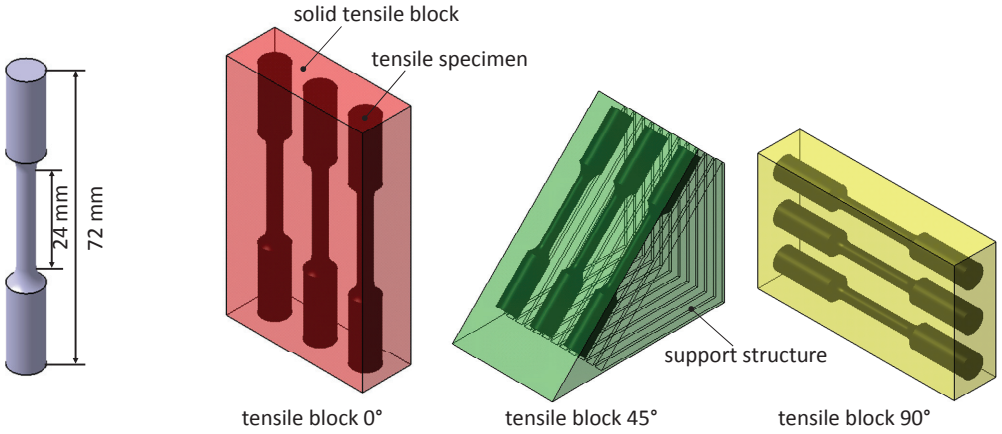

Figure 30 Schematic view of the tensile blocks and the tensile specimens that are machined out of the block

4.7.3 Evaluation Methodology

The tensile test is carried out at room temperature. The strain rate is $3 \times 10^{-4}\ s^{-1}$. The strain is measured by an extensometer. The stress-strain curves are recorded, and the yield strength, tensile strength, elongation, and strain energy are measured (*Figure 31*).

The analysis of the stress-strain curves is carried out with the software *OriginPro 8.5*.

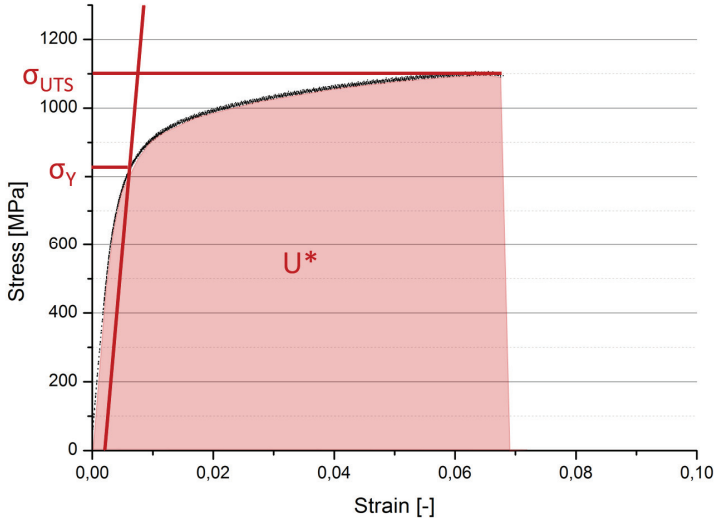

Figure 31 Schematic representation of the evaluation of the tensile test

5 Results

5.1 Section 1: Density and Process Reliability

As described in *Chapter 4.3*, cubic geometries are printed (*Figure 32*). The influence of laser power and exposure time on the density and process reliability is investigated. All specimens can be built. However, warping is observed with some of the high energy input samples. In some cases, warping get so intense that the samples are not completely covered after the application of the new layer of powder, and the slider tool is slightly damaged during the build process. The influence of the laser power on the density is shown in *Figure 33* (left). The influence of the exposure time on the density is shown in *Figure 33* (right). In addition, the standard deviation is shown as an error indicator.

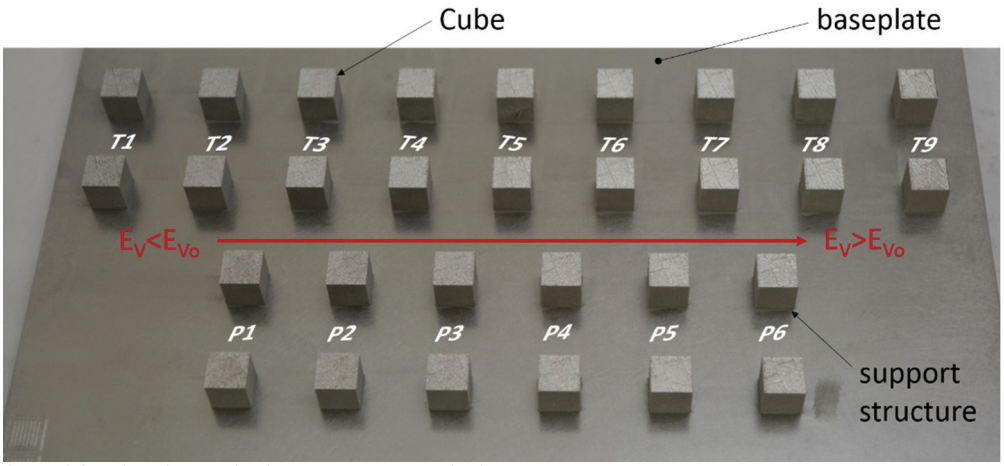

Figure 32 Build used for density and microstructure analysis

Influence of Laser Power (t = 100 µs = const.): At a laser power of P_L = 160 W, a density > 99% is achieved (*Figure 33*, left). The density achieved by this parameter is approximately 99.1%. Hence, the laser power of 160 W is the lower boundary for the parameter window. With the standard process parameters provided by Renishaw (P_L = 180 W and t = 100 µs), a density of

only 99.6% can be achieved. By increasing the laser power to 200 W, the density can be further increased to 99.8% (*Figure 33*, left). This is the upper boundary of the parameter window, since 200 W is the highest laser power the Renishaw system provides. Warping does not occur in this case.

Influence of Exposure Time (P_L = 180 W = const.): A density > 99%, i.e. approximately 99.1%, is achieved with an exposure time of 90 µs and, thus, forms the lower limit of the process window (*Figure 33,* right). An increase in the exposure time to 110 µs causes the initiation of warping (*Figure 33,* right). Although there is no need to abort the build at this exposure time in the case of simple builds, there may be amplification of the warping effect with more complex geometries, as in thin-walled or overhanging parts. Thus, an exposure time of 110 µm is defined to be the upper limit for the process window.

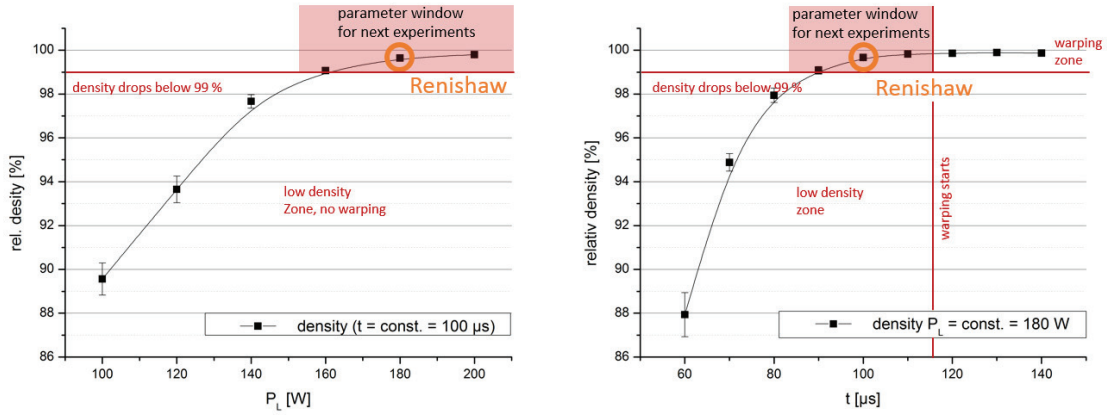

Figure 33 Influence of laser power (left) and exposure time (right) on the relative density. The red lines indicate the boundaries of the process window. The Renishaw standard parameter is orange.

Influence of Height of Construction: In addition, the density with regard to the height of construction of the components is determined. Since all experiments are performed with a preheat temperature of 150°C and all specimens are built on supports, thermal conductivity changes with the height of construction. This may have an influence on the density of the samples. However, the experimental results (*Figure 34*) show a nearly constant density independent of the height of the samples.

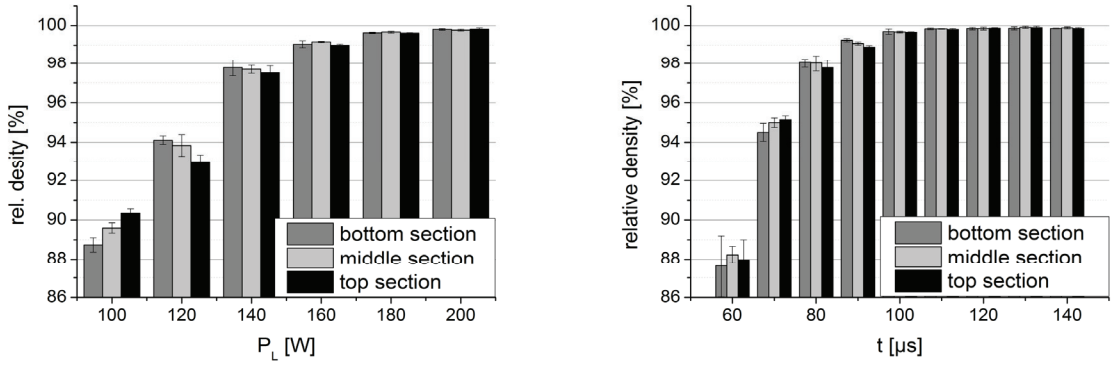

Figure 34 Influence on laser power (left) and exposure time (right) on the density with regard to the height of construction

Interim Conclusion: In general, the density of the samples increases if the volume energy is increased, but warping begins if the energy introduced into the powder exceeds a certain level. The parameter window is thus limited on one hand by a density of 99% and on the other hand by the onset of warping (*Figure 33*, marked red). The relatively large standard deviations for the specimens with comparatively low densities are due to the increasing measurement error at low densities described in *Chapter 4.3.3*. To compare the laser power variation outcome with the exposure time variation outcome, the volume energy is used (*Figure 35*).

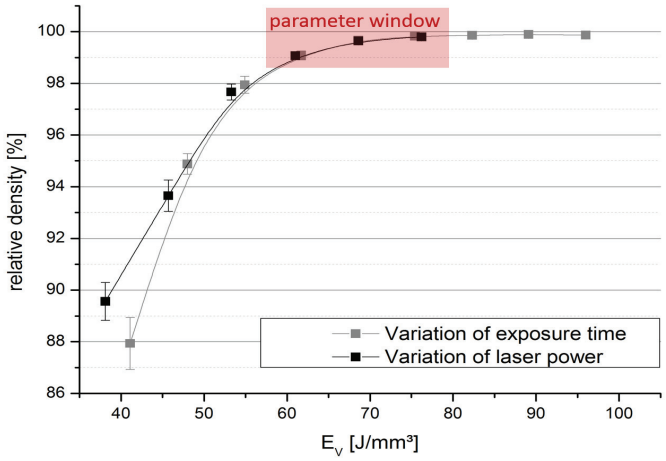

Figure 35 Relative density vs. volume energy for the laser power and the exposure time variation

It is worth mentioning that nearly identical densities can be achieved with the same energy input by varying the different parameters. Consequently, different microstructures should arise.

Finally, a selection of polished cross-sections is presented in *Figure* 36. The process parameters used for subsequent experiments (hence, the parameters that comprise the parameter window) are summarized in *Table 11*.

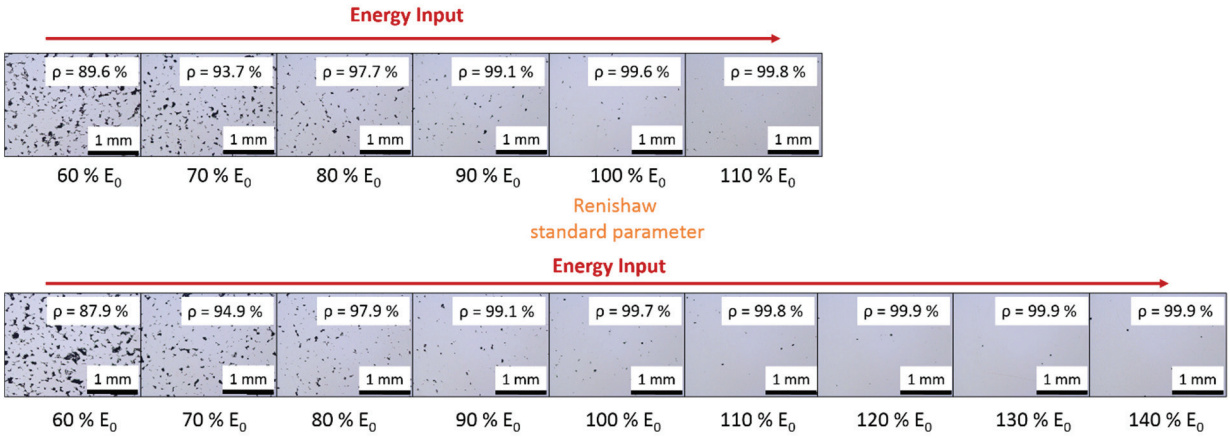

Figure 36 Collection of cross-sections used for density analysis

Table 11: Parameter window with parameters used for subsequent experiments

	Laser power [W]	Exposure time [µs]	Relative density [%]
Combination 1	160	100	99.1
Combination 2	180	100	99.6
Combination 3	200	100	99.8
Combination 4	180	90	99.1
Combination 5	180	110	99.8

5.2 Section 2 Melt Pool Shape

As described in *Chapter 4.4*, four single tracks are printed on a mini substrate plate (hereafter referred to as single tracks). In this section, the influence of the scanning speed and laser power to various quality parameters characterizing the melt pool are investigated. In addition, the melt pools of the last exposed layer of the cube geometries built in *Section 1* are investigated (hereafter referred to as skin tracks).

Influence of Laser Power on Single Tracks (t = 100 µs = const.): The influence of laser power on the area, width, and height of the resulting melt pool are presented in *Figure 37*. With increasing laser power, that is, with the increase of the introduced volume of energy input into the powder bed, as expected, the surface of the melt pool, as well as of the melt pool width and height increases. With an increase of the laser power from 160 to 180 W, the surface of the melt pool increases by approximately 33% from 6000 to 8000 µm. With a further increase of 180 to 200 W, the area increases only very slightly and remains almost constant (*Figure* 37*,* top left). Strikingly, however, are the extremely large standard deviations that indicate a large uncertainty.

The influence of laser power on the circularity, roundness, and solidity is shown in (*Figure* 37*,* bottom left). With an increase in the laser power from 160 to 180 W, there is an initial increase in the roundness, circularity, and solidity. This means that the melt pool in the first iteration is more round, circular, and compact. With further increase of the laser power from 180 to 200 W, circularity and solidity remain almost constant; the roundness, however, drops. This means with increasing laser power, or increasing volume energy, the melt pool becomes increasingly compact and more circular. In addition, the melt pool becomes more elliptical if a high laser power (200 W) or a low laser power (160 W) is used.

Influence of Exposure Time on Single Tracks (P_L = 180 W = const.): The influence of exposure time on the area, width, and height of the resulting melt pool is shown in *Figure* 37*,* top right. The melt pool area initially increases with increase in the exposure time from 90 to 100 µs and then again decreases with further increase in the exposure time to 110 µs (peak melt pool area at exposure time of 100 µs). However, the large standard deviation could also be an indication of measurement uncertainties. The melt pool height and width remain relatively constant (*Figure* 37*,* top right).

The influence of exposure time on the circularity, roundness, and solidity is shown in *Figure* 37 (bottom right). As previously described in the section pertaining to the investigation of the influence of laser power, if the exposure time is increased from 90 to 100 µs, the roundness initially increases and then decreases with further increase in exposure time. The situation is similar with the circularity. The solidity increases with increase in the exposure time without showing a similar decrease with further rise in exposure time. However, both parameters solidity and circularity do not change significantly in the investigated exposure time interval of 90 to 110 µs (*Figure* 37, bottom right).

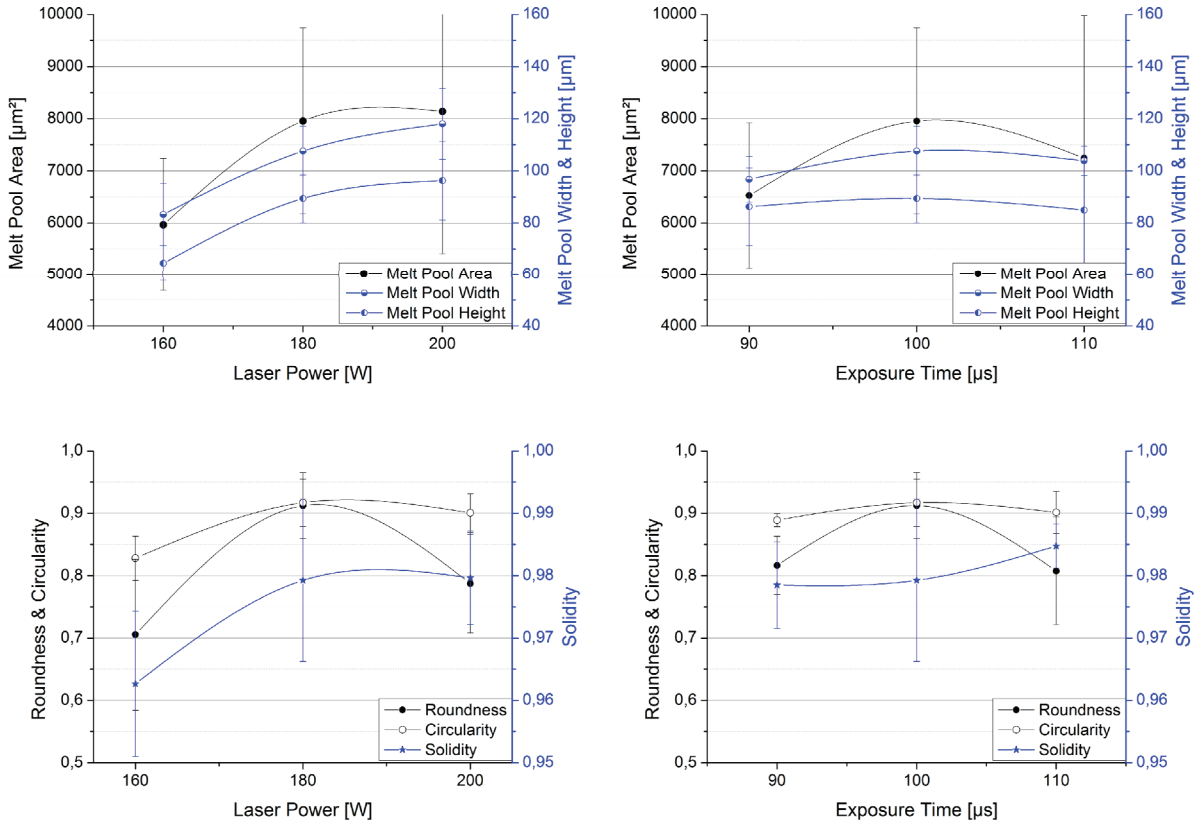

Figure 37 Left: Laser power vs. melt pool area, length, and width (top). Laser power vs. roundness, circularity, and solidity (bottom) single tracks (t = 100 µs = const.)
Right: Exposure time vs. melt pool area, length, and width (top). Exposure time vs. roundness, circularity, and solidity (bottom) single tracks (P = 180 W = const.)

Influence of Laser Power and Exposure Time on the Skin Tracks: Due to the high standard deviations for the single track investigation, an evaluation of the skin tracks is performed and presented in *Figure 38*.

There is a greater quantity of melt pools available for measurement, which results in a much smaller standard deviation. The curves for the laser power variation and exposure time variation (*Figure 38,* top) are very similar. In both cases, an increase in the volume energy results in a larger melt pool width, height, and area. Roundness, circularity, and solidity remain constant within the framework (*Figure 38,* bottom).

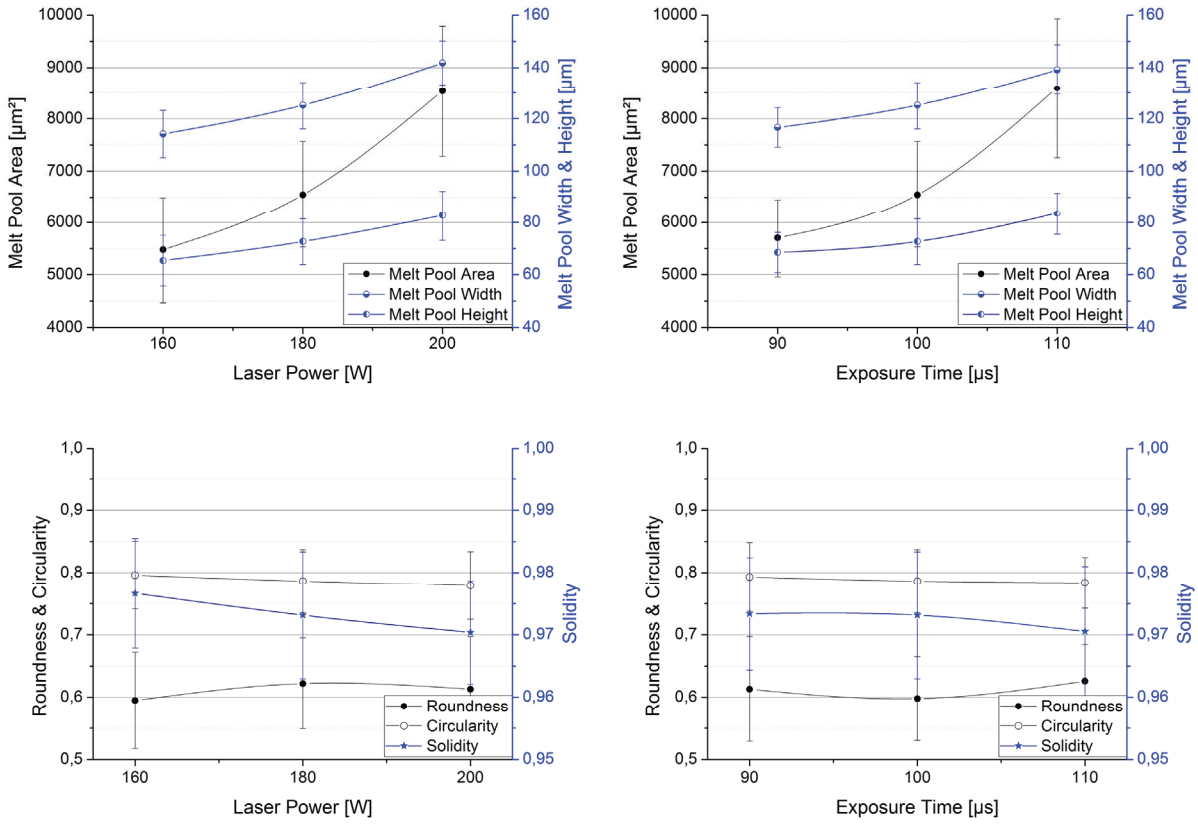

Figure 38 Left: Laser power vs. melt pool area, length, and width (top). Laser power vs. roundness, circularity, and solidity (bottom) skin tracks (t = 100 µs = const.)
Right: Exposure time vs. melt pool area, length, and width (top). Exposure time vs. roundness, circularity, and solidity (bottom) skin tracks (P = 180 W = const.)

Interim Conclusion: In the case of the skin tracks, the curves of the laser power variation and exposure time variation are almost identical. The single track curves sometimes differ widely. This is due in part to the very different melt pool shapes. Two characteristic melt pool shapes are shown in *Figure 39*. The melt pool shape of the single tracks are more rounded; the tracks of the skin tracks tend to be rather elliptical.

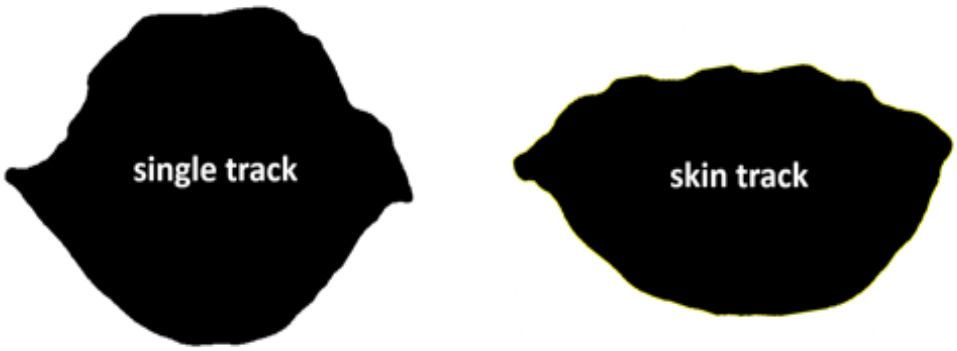

Figure 39 Characteristic melt pools for single tracks (left) and skin tracks (right)

Some major differences become evident upon comparison of the results for the single tracks with those of the skin tracks. In the case of the skin tracks, the melt pool area increases continuously for both variations (laser power and exposure time). In contrast, the melt pool areas of the single tracks reach a maximum at a medium energy input (medium laser power and medium exposure time) and decrease again with exposure time variation. However, the melt pool area remains almost constant with variation in laser power. For both variations, the melt pool width is greater for the skin tracks than the single tracks. In contrast, the melt pool height for the skin tracks is lower than for the single tracks (*Figure 40,* top). This difference can be explained by the melt pool shape (*Figure 40,* bottom). The large difference to be noted with regard to the parameter "roundness" between the single tracks and the skin tracks is remarkable. Single tracks have a much higher value for roundness, which means that the melt pools are more round than those of the skin tracks. In comparison, a lesser roundness value means a more elliptical shape. This explains the relatively closely spaced curves for melt pool width and melt pool height for the single tracks, as well as the further apart curves for the skin tracks

(*Figure 40* blue top). The circularity of the single tracks is higher than that of the skin tracks. However, this is due to the elliptical shape of the skin tracks and not secondary to any roughness peaks or microscopic irregularities. The solidity of all investigated melt pools is invariably greater than a value of 0.95, which indicates a very large concavity of the melt pool and, hence, the absence of convex surfaces.

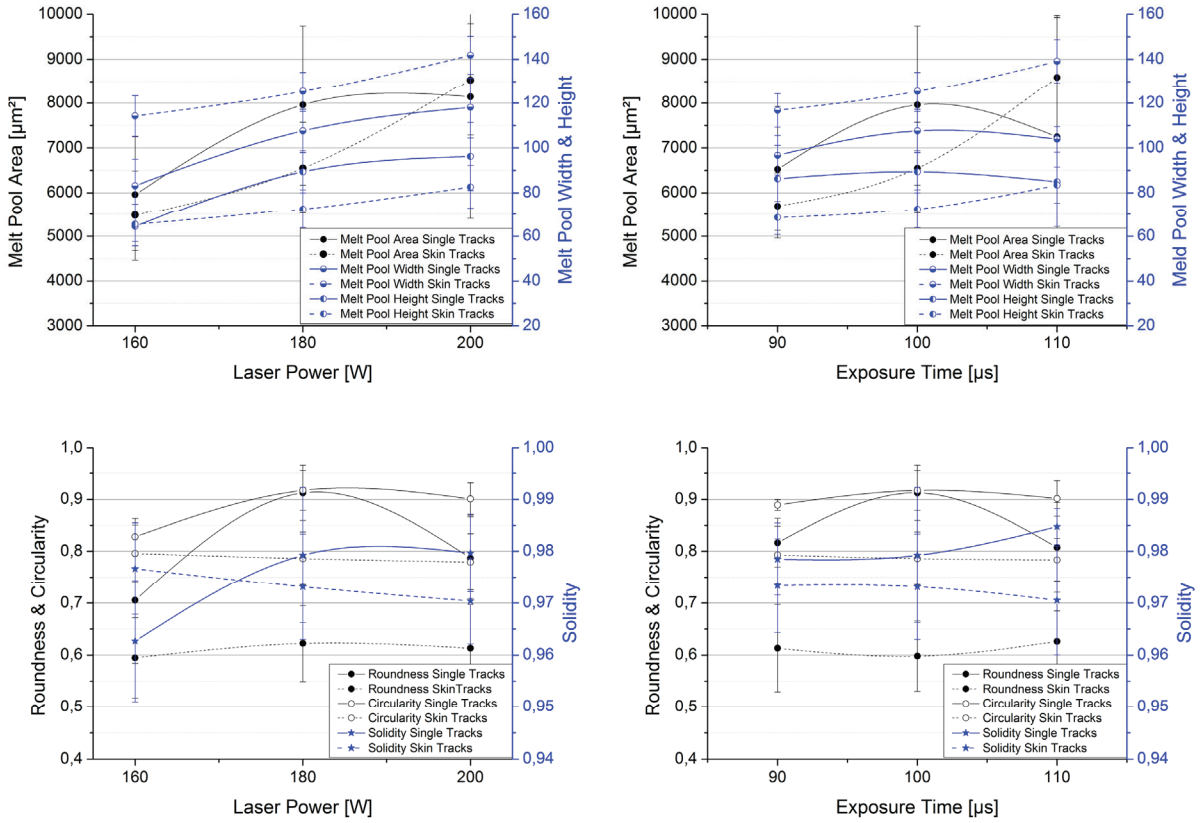

Figure 40 Comparison of single tracks and skin tracks
Left: Laser power vs. melt pool area, length, and width (top). Laser power vs. roundness, circularity, and solidity (bottom) (t = 100 µs = const.)
Right: Exposure time vs. melt pool area, length, and width (top). Exposure time vs. roundness, circularity, and solidity (bottom) (P = 180 W = const.)

5.3 Section 3: Deformation Due to Residual Stress

5.3.1 Deformation of Twincantilevers

All of the twincantilevers used in these experiments were built without issue. Macroscopic defects such as cracks or separation of the twincantilever arm from the supports were not observed. After wire EDM, the twincantilever arms bent upwards as expected (*Figure 41*).

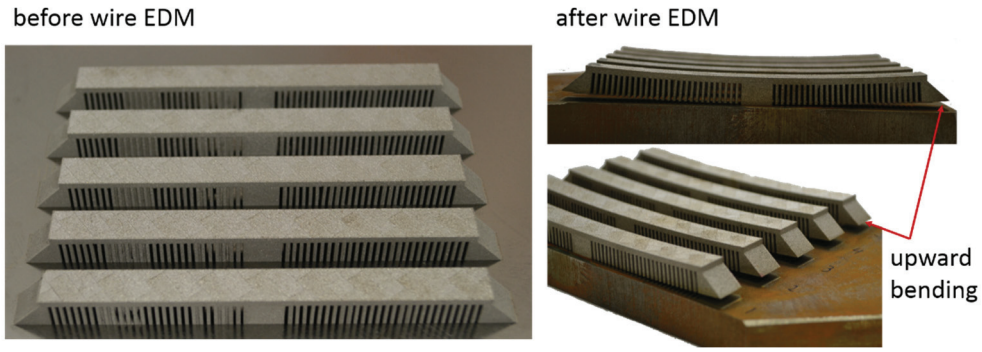

Figure 41 Twincantilever before (left) and after (right) wire EDM

The maximum deformation in z-direction on the very edge of the twincantilever arm amounts to 2.1 mm on average. The difference between the lowest and the highest deformation in z-direction is 300 µm and is, therefore, very low.

Influence of Volume Energy: The impact of the volume energy is shown in *Figure 42*. In order to improve clarity, the twincantilevers built with high energy input (E_V = 110% E_{V0}) are shown in red. The twincantilevers built with a medium energy input (Renishaw Parameter: E_V = 100% E_{V0}) are shown in orange, and the twincantilevers built with low energy input (E_V = 90% E_{V0}) are shown in blue. As depicted in *Figure 42,* no clear trend can be identified. The smallest deformation in z-direction is achieved at an energy input of E_V = 100% E_{V0}, which is the medium energy input.

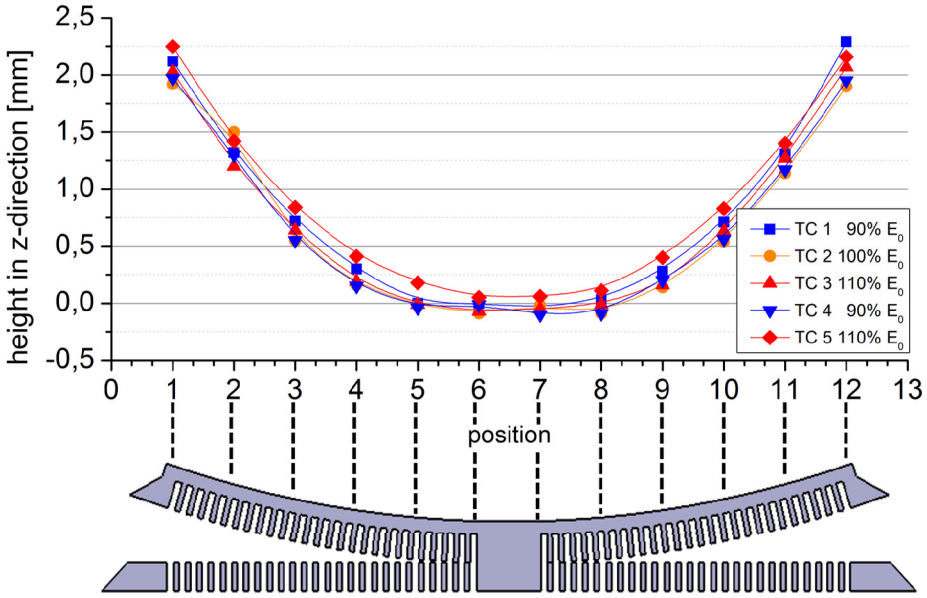

Figure 42 Influence of volume energy on the deformation in z-direction

Influence of Laser Power (t = 100 µs = const.): The influence of laser power on the deformation in z-direction is presented in *Figure* 43. The exposure time is kept constant at t = 100 µs, and the laser power is advanced in three steps from 160 to 180 to 200 W. Again, no clear trend can be distinguished, since the deformation in z-direction achieved is nearly uniform.

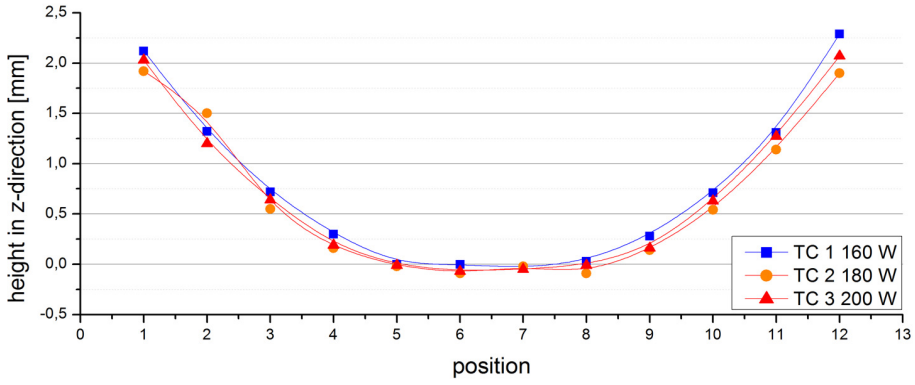

Figure 43 Influence of laser power on the deformation in z-direction (t = const. = 100 µs)

Influence of Exposure Time (P = 180 W = const.): The influence of exposure time on the deformation in z-direction is presented in *Figure 44*. In this case, the laser power is kept constant at P_L = 180 W. The exposure time is advanced in three steps from 90 to 100 to 110 µs. According to *Figure 44*, the twincantilever build with an exposure time of 110 µs (red), meaning a low scan velocity, stands out. The other two twincantilevers have almost identical upward bending curves. The difference in deformation at the outermost point of the cantilever arm in every case is 300 µm, thus, comparatively small.

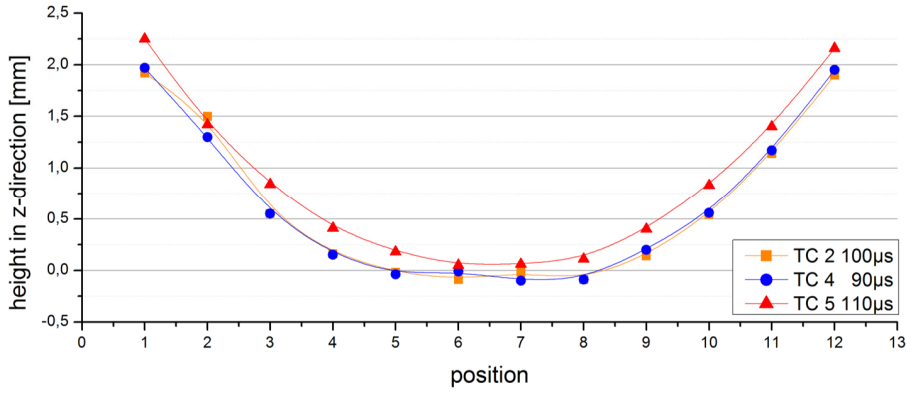

Figure 44 Influence of laser power on the deformation in z-direction (P = const. = 180 W)

Bridges: Due to a necessary recalibration of the FARO LaserArms, the measurement of bridge geometries cannot be performed for this study. Therefore, the evaluation of the bridge geometries is omitted.

Interim Conclusion: Due to the small difference in deformation in z-direction, it is not possible to determine a trend. The clearest result that hints at a trend is obtained in the investigation of the influence of exposure time. In this case, the deformation in z-direction is achieved at maximum exposure time. It should be noted, however, that the difference in deformation of the upward arm is a maximum of 300 µm and, thus, is very small. The influence of laser power seems to play a minor role when it comes to deformation

due to residual stress. Furthermore, there is no trend identifiable for different volume energies in this investigation.

5.4 Section 4: Microstructure

5.4.1 Optical Microscopy

Figure 45 shows an example of the etched cross-section of a cube sample. The laser power used to build this sample is 180 W, and the exposure time is 100 µs (Renishaw default parameters). The cross-section parallel to the build direction is shown in *Figure 45* (left), and the cross-section normal to the build direction is shown on the right. The cross-sections of the other samples can be found in *Appendix A7.* The melt pools, which are typical for the SLM method, are clearly visible.

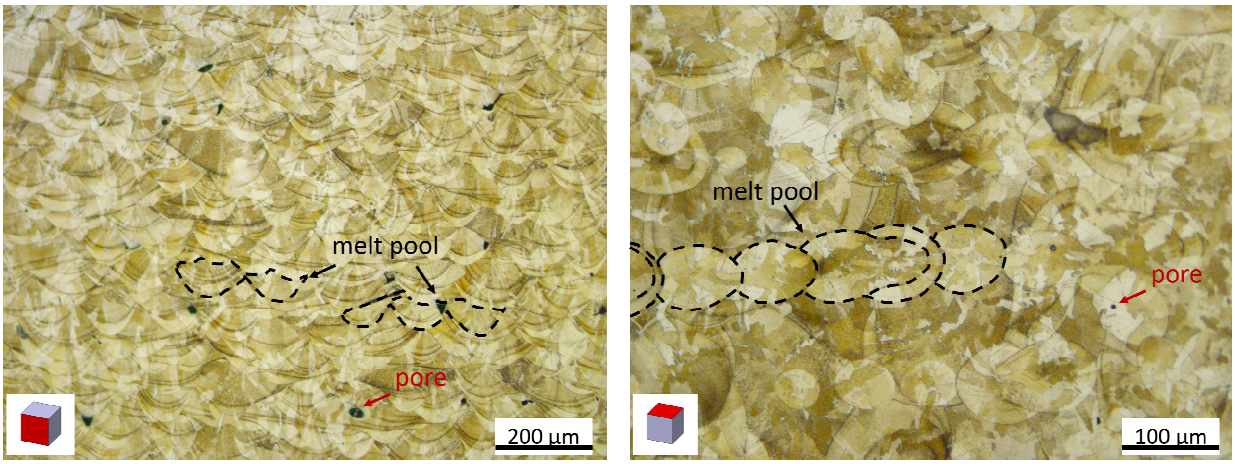

Figure 45 Etched transverse cut of a sample; Left: z-y-plane; Right: x-y-plane (P = 180 W and t = 100 µs)

5.4.2 Scanning Electron Microscopy (SEM)

A fine metallic structure is created within the melt pool as a result of the high cooling rate. This metallic structure is investigated by means of scanning electron microscopy. *Figure 46* shows an SEM image of a sample built with the Renishaw standard parameters. In *Figure 46* it can be seen that the material has solidified in a cellular manner. The cellular grains are to be seen as the dark spots in *Figure 46*. The cellular grains are separated by the light cellular

boundary (*Figure 46*). The orientation of the cells and, thus, their orientation in the cross-section varies. However, the elongated cells are predominant in the z-x-plane. Due to the cutting angle, the honeycomb structure is predominant in the x-y-plane (*Figure 46*). At the melt pool boundaries, a coarser grain structure is often observed. The growth of cells is usually epitaxial oriented to the cells of the previously solidified layer (*Figure 46*). The SEM images using different laser power and exposure times within the parameter window do not show significant differences. For this reason, only the SEM images of the Renishaw standard parameter are shown (*Figure 46*).

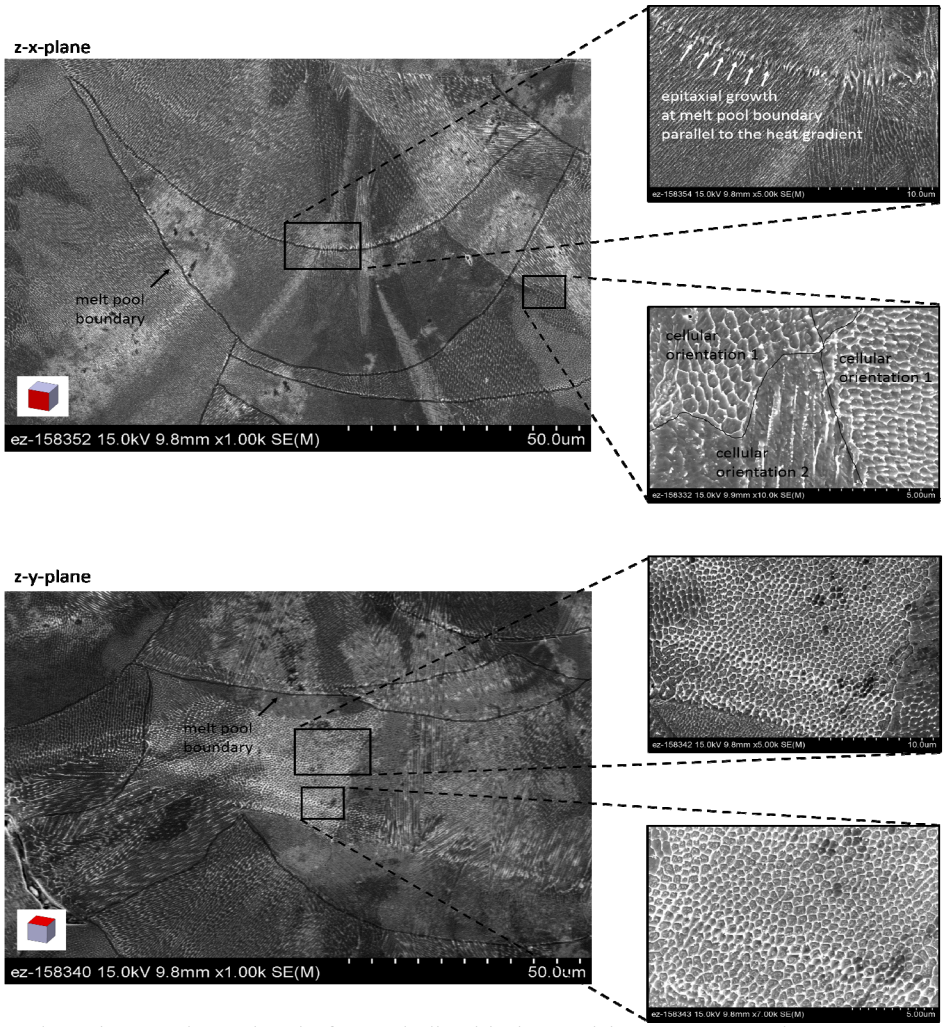

Figure 46 SEM images (z-x-plane and x-y-plane) of parts built with the Renishaw parameter (P = 180 W; t = 100 µs)

Finally, an EDS analysis is performed. The composition of the structure is measured in the intercellular region and at the cellular grain boundaries. The focus of the EDS analysis is on the elements Cr and Mo.

Influence of Laser Power (P4 – P6): The influence of the laser power on the chemical composition is shown in *Figure 47* (samples P4 - P6). In addition, the wt% portion measured over the whole picture is presented as a black column and is used as a reference. The fluctuations are always less than 1 wt% and are, therefore, very low. A clear trend is thus not identifiable. In comparison with the Mo content of the entire sample, the Mo content in the center of the cellular grain is always larger. The Mo content in the cellular grain boundaries varies. In contrast, the Cr content within the cellular grain is always smaller than that of the entire sample. The situation is similar with the Cr content in the cellular grain boundaries. Comparing intracellular regions of the grains with the cell boundary regions, the cell boundaries are poorer in Mo than the center of the cell, but richer in Cr (*Figure 46*, P4 - P6).

Influence of Exposure Time (T4 – T6): The influence of the exposure time on the chemical composition is shown in *Figure 46* (samples P4 - P6). As before, the wt% portion measured over the entire picture is presented as a black column and is used as a reference. As with the studies on the influence of the laser power on the microstructure, the fluctuations are always less than 1 wt%. Consequently, a trend is also difficult to identify in this case. The Mo-content of the entire specimen is always less than the Mo-content of the center of the cell, with exception of the specimen T5 (180 W; 100 µs). The same applies to the Cr-content with the exception of sample T6. The Mo-content and the Cr-content in the cellular boundary is always greater than the Cr-content of the total area. A comparison of cell centers with the cellular boundaries demonstrates a Mo-enrichment in the boundary areas and chromium-enriched cell centers.

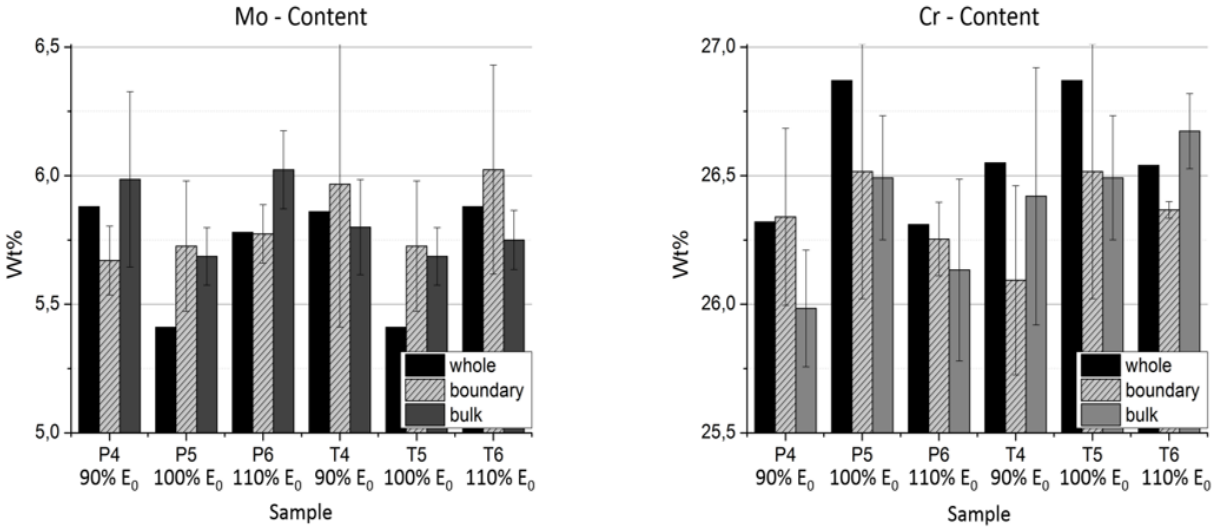

Figure 47 Chrome and Molybdenum content of the investigated sample measures at the cellular boundary and bulk. P4 – P6: exposure time = const. = 100 µs; T4 – T6: Laser Power = const. = 180 W

5.4.3 EBSD and Grain Size

Influence of Laser Power (*t*= 100 µs = const.): The influence of the laser power on the grain size is shown in *Figure 48*. The EBSD analysis shows that the grains grow in build direction with different crystal orientations. In some cases, the grains expand beyond the melt pool and layer thickness. Due to the growth of grains elongated in the direction of construction, the grain boundaries are also mainly in build direction. A preferred direction of the crystal orientation is not clearly identifiable (*Figure 46*). It is noticeable that the grains, depending on the laser power, grow in the direction normal to the build direction. This means the grains become wider with increase in laser power. A statistical evaluation of the area fraction vs. grain size is shown in *Figure 46* on the right.

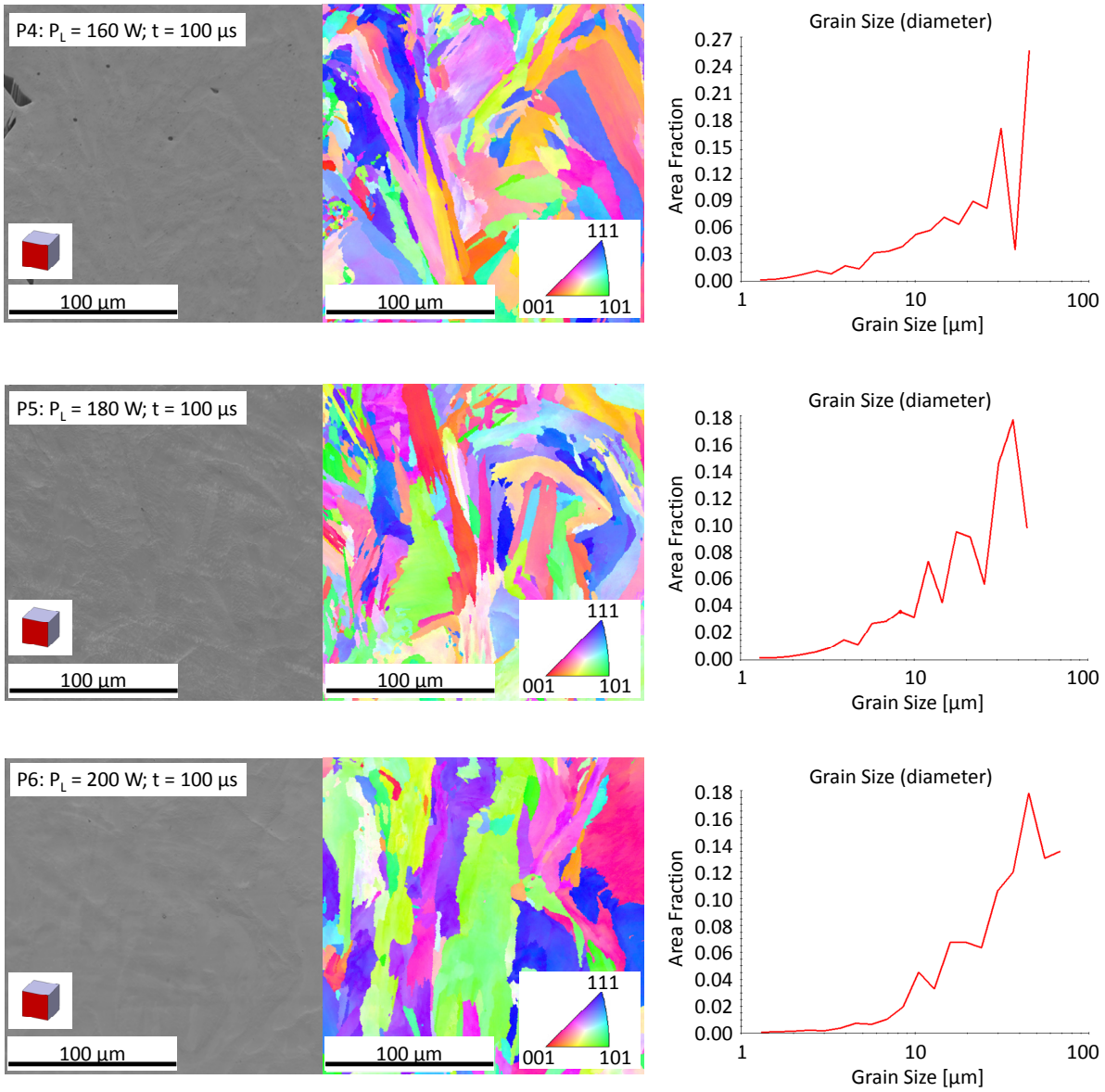

Figure 48 Influence of the Laser Power: SEM image (left) and EBSD inverse pole figure map (middle) and grain size distribution (right) (t = 100 µs = const.)

In addition, the cumulative distribution of the grain size in the horizontal and vertical planes is measured by the line cut method and shown in *Figure 49*. Furthermore, the minimum, maximum, and mean grain size, as well as the median grain size and the standard deviation are listed in *Table 12*. As visually recognizable,

the grain size increases with increasing laser power. The increase in grain size between 180 W and 200 W is significant.

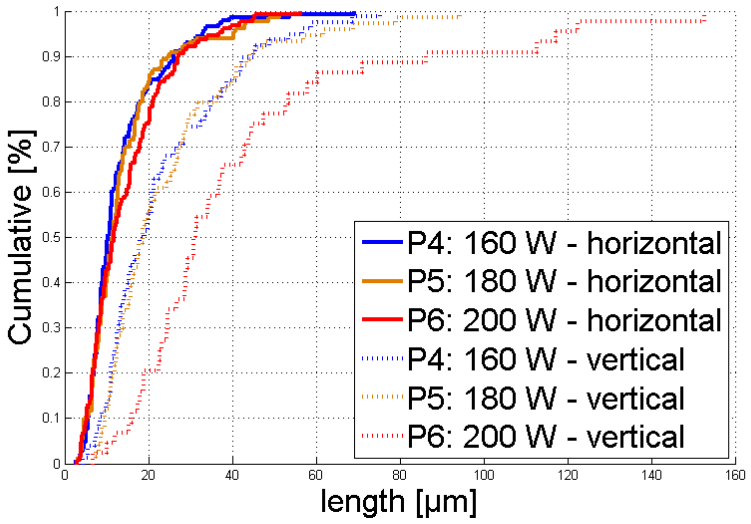

Figure 49 Cumulative grain size distribution. Exposure time constant t = 100 µs

Table 12 Max, min, mean and median grain size depending on the laser power (t = 100 µs = const)

No.	P_L [mm]	Min horizontal [µm]	Min vertical [µm]	Max horizontal [µm]	Max vertical [µm]	Mean horizontal [µm]	Mean vertical [µm]	Median horizontal [µm]	Median vertical [µm]	Std Horiz. [-]	Std vertical [-]
P4	160	2.76	4.51	69.11	75.39	13.48	23.18	10.44	18.62	9.72	15.28
P5	180	2.96	6.70	55.09	94.33	14.04	24.34	11.40	18.63	10.02	17.01
P6	200	3.00	6.84	56.39	152.72	14.77	41.63	11.70	31.10	10.00	31.78

Influence of the Exposure Time (P = 180 W = const.): The influence of the exposure time on grain size and crystal orientation is shown in *Figure 50*. Again, the EBSD analysis shows growth of elongated grains in build direction with different crystal orientations. Similar to the studies of the influence of the laser power, an increase in the exposure time leads to larger grains and higher growth than a single melt pool height. Also, as before, grain growth is mainly horizontal to the build direction.

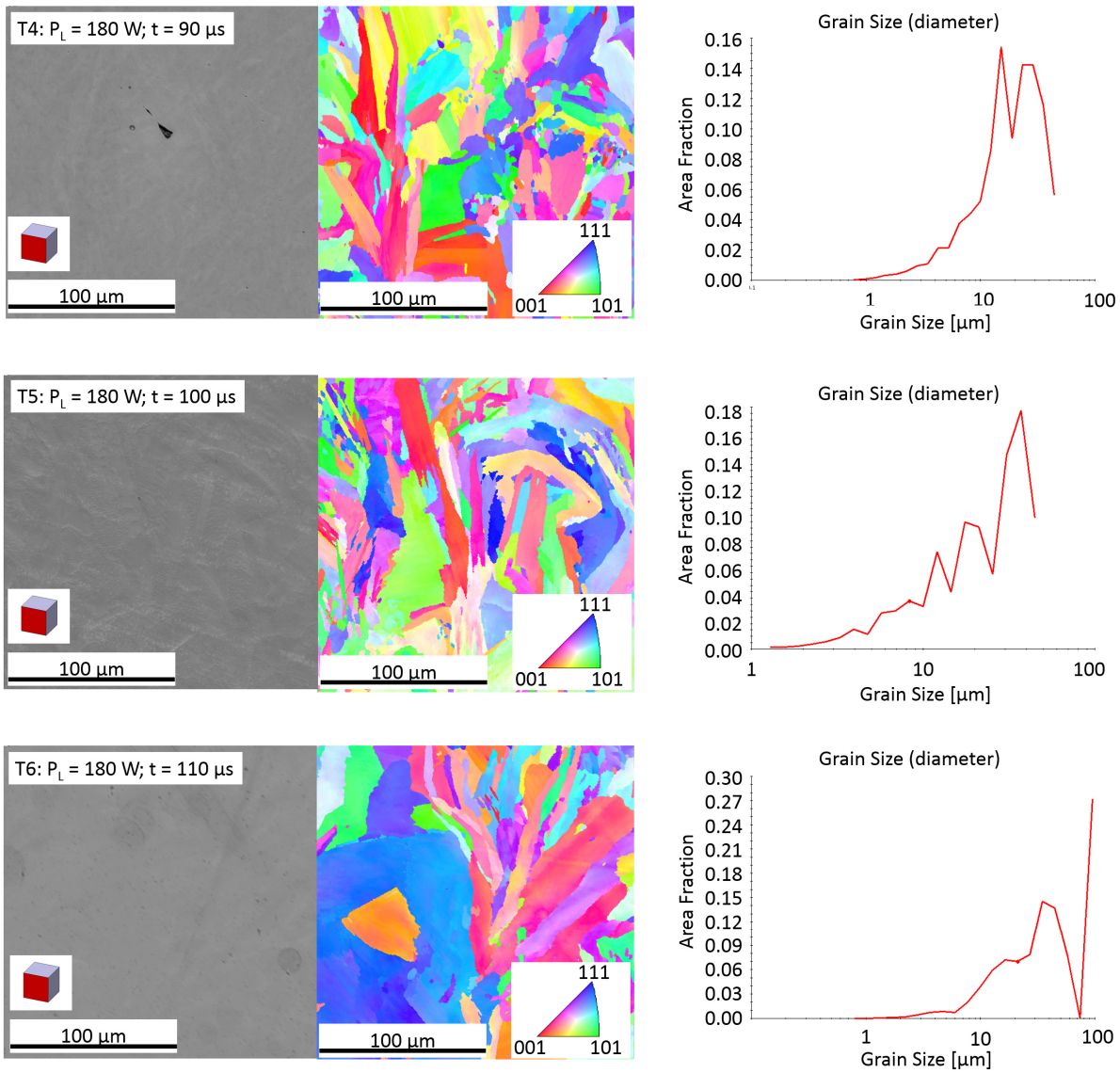

Figure 50 Influence of the exposure time: SEM image (left), EBSD inverse pole figure map (middle), and grain size distribution (right) (P = 180 W = const.)

The cumulative grain size distribution with relation to the exposure time in horizontal and vertical direction is measured and shown in *Figure 51*. Similarly, as previously, the minimum, maximum, and average grain diameter is listed in *Table 13*, as well as the median and the standard deviation. The increase in grain size can be

clearly seen. The grain size increases with increase in exposure time (*Figure 51*).

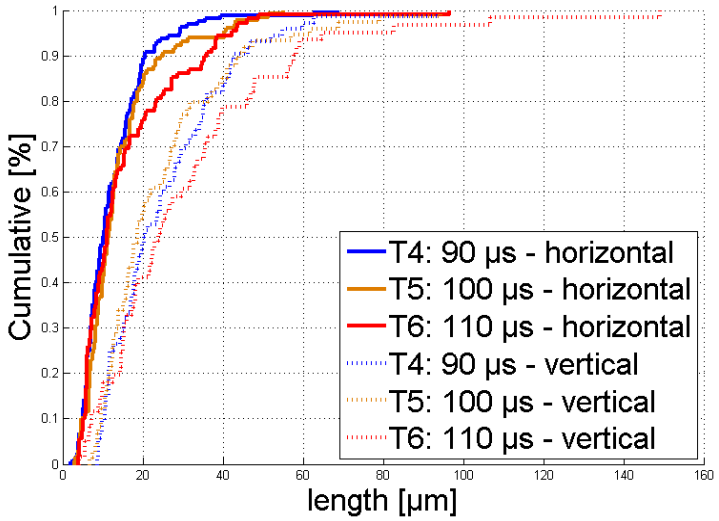

Figure 51 Cumulative grain size distribution. Laser Power constant $P = 180$ W

Table 13 Max, min, mean and median grain size depending on the laser power ($P = 180$ W = const)

No.	t_{exp} [ms]	Min horizontal [µm]	Min vertical [µm]	Max horizontal [µm]	Max vertical [µm]	Mean horizontal [µm]	Mean vertical [µm]	Median horizontal [µm]	Median vertical [µm]	Std horiz. [-]	Std vertical [-]
T4	90	2.13	8.68	68.62	93.85	12.50	25.40	10.02	20.41	9.16	15.63
T5	100	2.96	6.70	55.09	94.33	14.04	24.34	11.40	18.63	10.02	17.01
T6	110	3.97	4.25	96.59	149.28	15.73	30.71	11.00	23.85	13.70	25.31

Interim Conclusion: It should be noted that the measuring range may be too small for a statistically reliable statement regarding the grain size. Nevertheless, the analysis provides at least an indication of value.

The grain growth occurs mainly parallel to the build direction. Increasing the volume energy input increases the grain size in general. At low volume energy, the result is small elongated grains. With increasing volume energy, elongated but broader grains are

present. The variation of the exposure time has a greater influence on the grain size change.

5.5 Section 5: Tensile Test

Irregular spark development can be observed during the build process (*Figure 52*) depending on the position of the part in relation to the baseplate. The tensile block number 1 with an angle of 0° to the build direction and the tensile block number 2 with an angle of 45° to the build direction are affected (*Figure 52*). A significant difference in spark development can be observed as presented in *Figure 52* during exposure. This indicates the possibility of locally reduced input of volume energy in these areas. The relatively high standard deviations depicted in the upcoming diagrams can be explained by this fact. This phenomenon is discussed in more detail in the "Discussion" chapter.

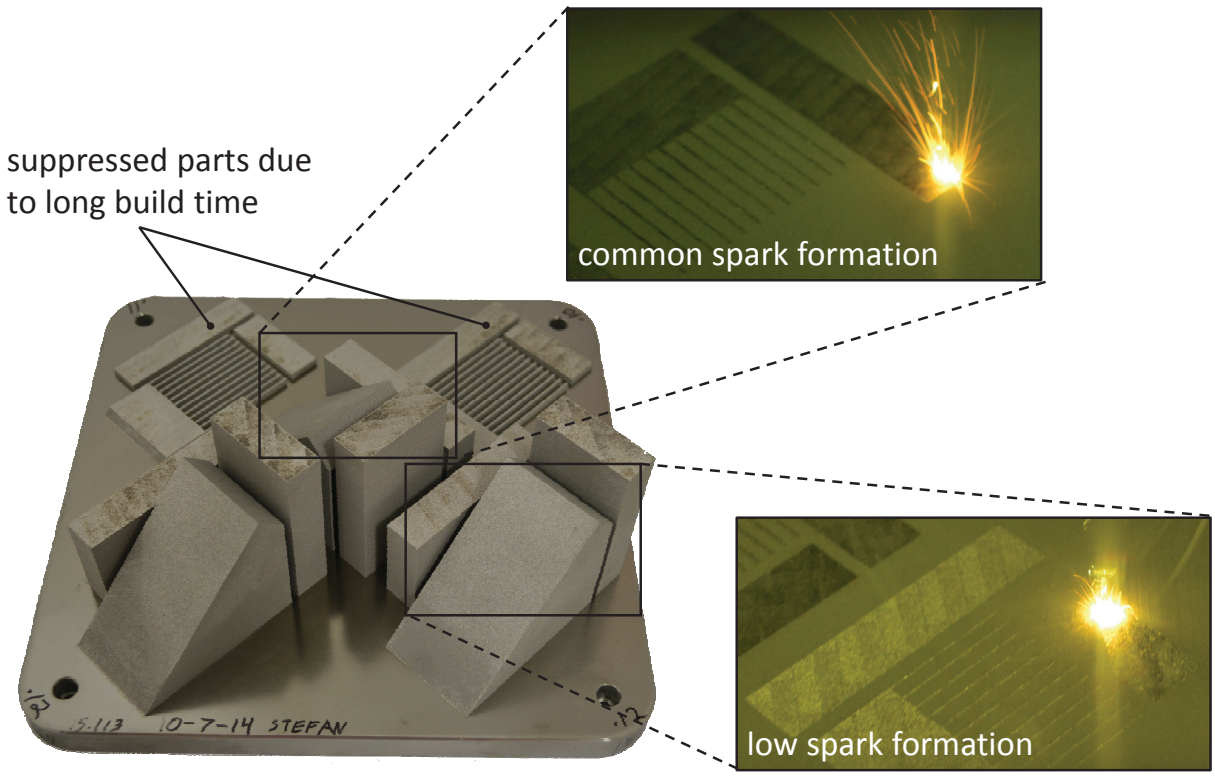

Figure 52 Tensile specimen build after completion and spark formation at a build height of 20 mm

As discussed previously, it was not possible to build all samples due to time constraints. Consequently, only the influence of the laser power and the influence of the angle to the build direction on mechanical properties are examined. The Young's modulus is 204 GPa on average. The stress-strain curves of all examined tensile test specimens can be found in the *Appendix A7*.

Influence of Laser Power (t = 100 µs = const.): Yield strength, tensile strength, elongation and strain energy depending on the laser power are shown in *Figure 53*. The black graphs represent the different build directions. The red graph represents the average of all tensile specimen built with the same laser power

For all investigated tensile specimens, the yield stress increases with increasing laser power, i.e., increasing volume energy input. The largest yield strength of 1000 MPa is achieved with a specimen build at an angle of 45° to the build direction. For specimen with an angle of 90° or 0° to the build direction a yield stress of 850 MPa or 650 MPa is achieved respectively (*Figure 53,* top left).

Similar results are achieved for the tensile strength. Again, large tensile strengths are obtained for large laser powers. The greatest tensile strength of approximately 1200 MPa, is achieved in the direction of 0° and 45° to the build direction. The minimum tensile strength is achieved with a specimen with an angle of 90° to the build direction and is approximately 980 MPa (*Figure 53*, top right).

Increasing the laser power increases the elongation. The greatest elongation is obtained at a laser power of 200 W and is approximately 9.8%. The smallest elongation is obtained at a laser power of 160 W and is approximately 1.5% (*Figure 53*, bottom left).

The strain energy increases with increasing the laser power. Here is the largest strain energy is achieved with specimen build with an angle of 90° with respect to the build direction. The lowest strain energy is achieved with specimen build with an angle of 45° and 0° with respect to the build direction (*Figure 53*, bottom right).

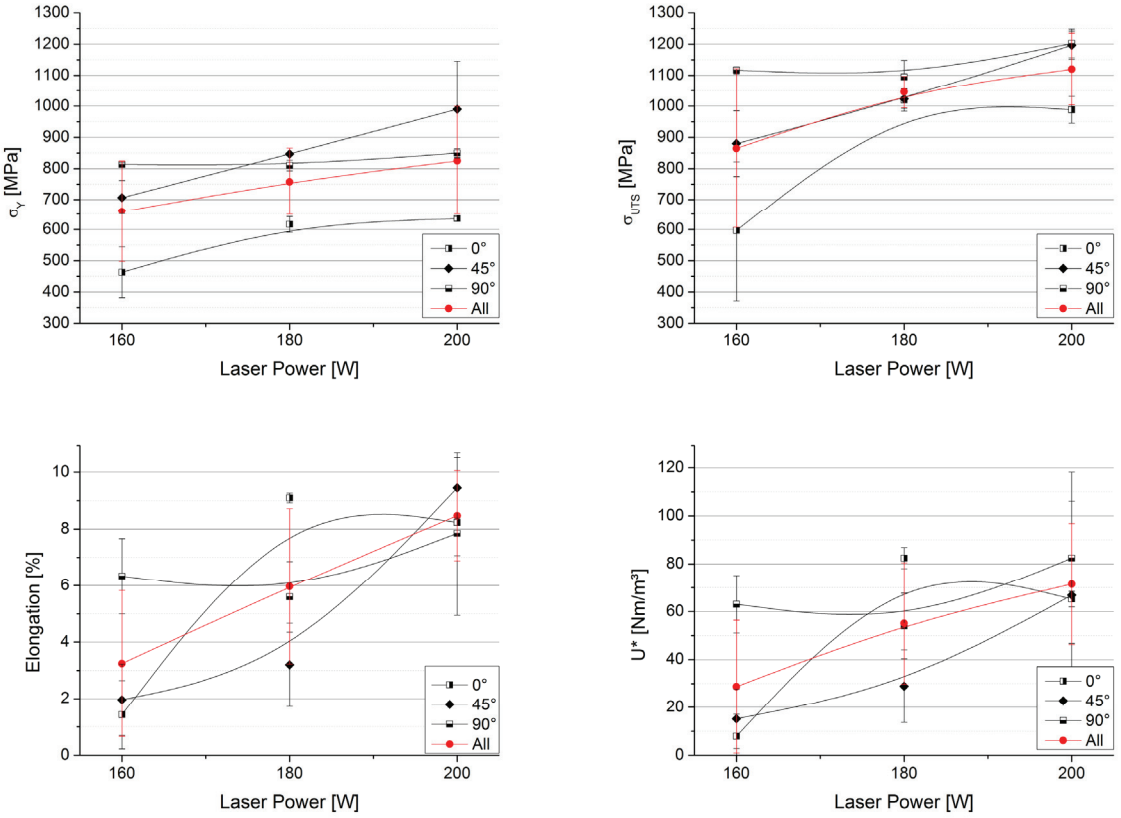

Figure 53 Tensile test results: Yield Strength (left), Tensile Strength (middle), Strain Energy (right) (t = 100 µs = const.)

Influence of Angle to the Build Direction (t = 100 µs = const.): The respective courses of the yield stress, tensile strength, elongation, and strain energy as a function of the angle to the build direction are shown in *Figure 54*. Graphs for specimens built with low, medium, and high volume energy are presented in blue, orange, and red, respectively.

The yield stress increases if the angle to the build direction increases (*Figure 54*, top left). The largest yield stress is obtained at an angle of 90° to the build direction, and the smallest yield stress is achieved for specimens with a 0° angle to the build direction. Also, it can be seen that with greater input of volume energy, the yield stress increases (*Figure 54,* top left).

In *Figure 54* (top right), it can be seen that the tensile strength increases with increasing angle to the build direction. The largest tensile strengths are obtained with specimens with an angle of 90° to the build direction. In addition, with a greater input of volume energy, a greater tensile strength is achieved (*Figure 54*, top right).

In the studies examining elongation as a function of the angle with respect to build direction, no clear trend is observed. The elongation of the specimens built with 200 W laser power remains almost constant. The elongation of the 160 or 180 W components falls or rises with increase of the angle to the build direction, respectively (*Figure 54*, bottom left).

With exception of one outlier at an angle of 0° to the build direction and a laser power of 180 W, the strain energy increases continuously with increasing angle to the build direction. Here, it can again be observed that a larger strain energy can be achieved with greater energy input (*Figure 54*, bottom right).

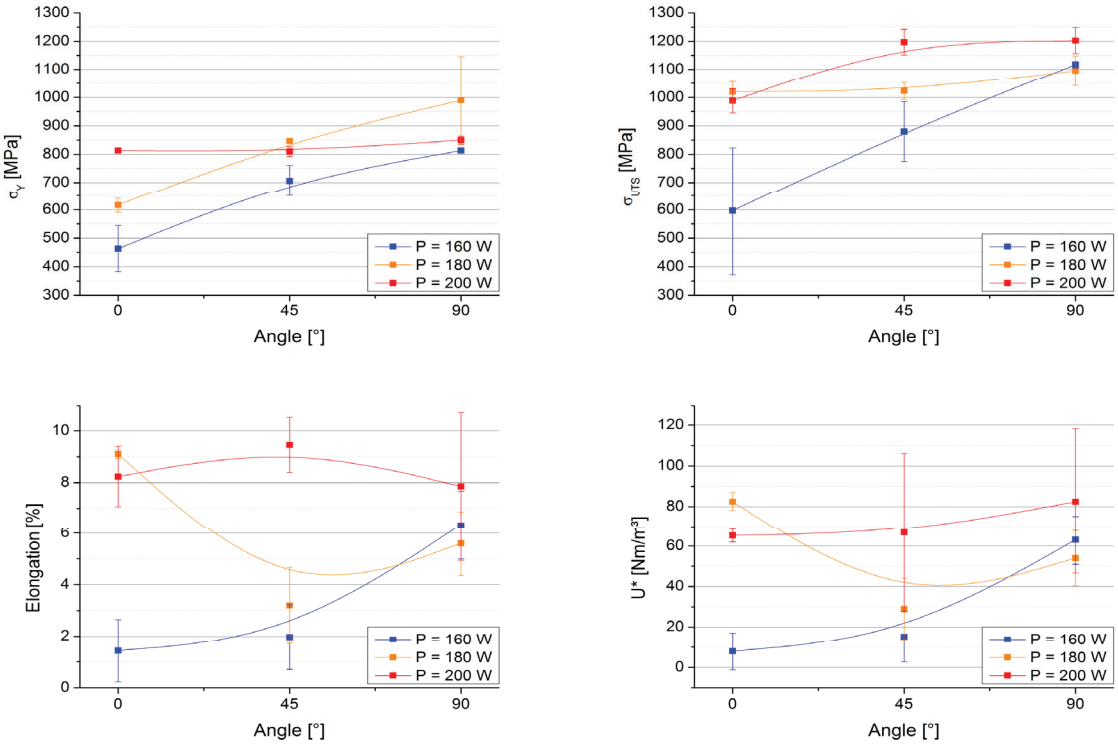

Figure 54 Tensile test results: Yield stress (left), Tensile Strength (middle), Strain Energy (right) (t = 100 µs = const.)

Interim Conclusion: The results of the tensile test show a significant dependence of yield stress, tensile strength, and strain energy on the input energy and angle to the build direction. Increasing the laser power results in an increase of yield stress, tensile strength, and strain energy, as well as an increase in volume energy. Increasing the angle to the build direction results in a significant increase in yield strength, tensile strength, and strain energy. No clear trend is identifiable for the elongation of the specimen.

6 Discussion, Conclusion and Recommendations

6.1 Section 1: Density and Process Reliability

Reliability: Warping during the build process takes place almost exclusively at the outermost region of the parts along the edges (contours). It is usually observed on the side of the part which is facing the slider. Little is known about the origin and the exact cause of warping during SLM. One possible cause of this effect is a thickening of the powder on the side facing the slider and an associated larger melt pool. The molten material adheres to the previously solidified layer due to adhesive forces (*Figure 55*, left). The large melt pool volume leads to a local elevation in the contour regions of the layer. This effect is further enhanced in the contour regions, since surrounding powder particles are drawn into the melt [29]. In addition to a local densification of the powder, this further increases the size of the melt pool. Moreover, this effect can be superimposed by delay of the parts due to residual stresses.

Density: The density of the parts obtained depends primarily on the volume energy introduced into the powder bed. Based on the shape of the resulting pores in the parts, it can be concluded whether there was a surplus of volume energy or a volume energy deficit during the build process. Small round pores indicate a volume energy surplus, while large jagged pores indicate a volume energy deficit (*Figure 55,* middle and right). In order to produce a closed compound material, it is necessary to completely melt the present layer, as well as to at least partially melt the underlying layer. This is not possible if the amount of input of volume energy is insufficient. The result in that case are jagged pores with sintered powder particles (*Figure 55,* right). If the amount of volume energy input is too great, it results in the evaporation of alloy elements that melt at low temperatures and, thus, rounded pores with a smooth inner surface (*Figure 55*, middle).

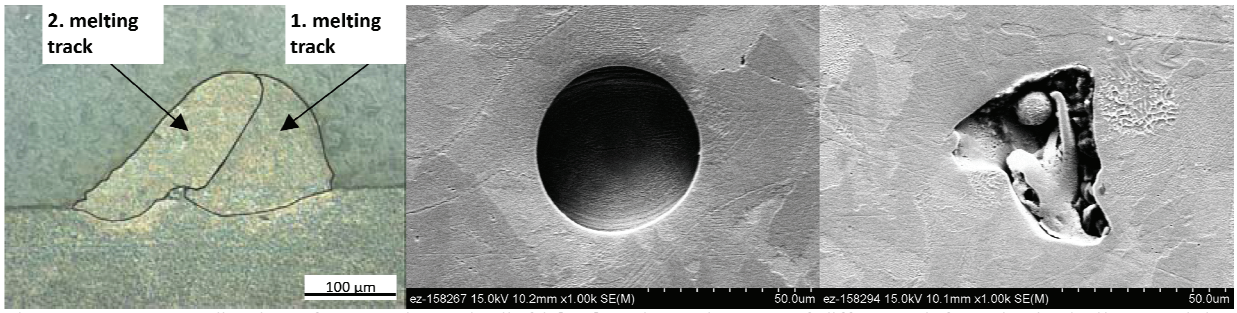

Figure 55 Adhesion of two melt tracks (left) [29] and SEM images of different defects in the bulk material (high energy input: middle; low energy input: right)

Parameter Window: Contrary to expectations, the identified parameter window is relatively small. The predefined boundary conditions for density and process reliability only omit a volume energy variation of ± 10% with respect to the Renishaw standard parameter. This is due to the fact that a silicone rod is used as a powder applicator tool. Silicone rods are sensitive to warping of parts during the build process. Consequently, parts that demonstrate relatively small amount of warping must be classified as hazardous. Thus, these components are outside of the defined parameter window.

Another reason for the unexpectedly small parameter window is the relatively low density (99.6 - 99.7%) achieved with the Renishaw standard parameter. This density in not typical for the SLM process. This is due to the incorrect hatch spacing chosen by Renishaw. The hatch spacing is 125 µm by default. Investigations of melt pools have shown that when using the Renishaw standard parameters, a maximum melt pool width of approximately 125 µm and a melt pool height of no more than approximately 70 µm can be achieved. This not enough to ensure complete melting of the powder layer including the underlying layer (*Figure 56*). The consequence is a relatively high porosity of the samples. In addition, this effect is enhanced by the high surface roughness present in SLM. Large surface imperfections affect the local layer thickness and can even triple it (*Figure 56*, top left). Thus, the melting of the underlying layer is made more difficult.

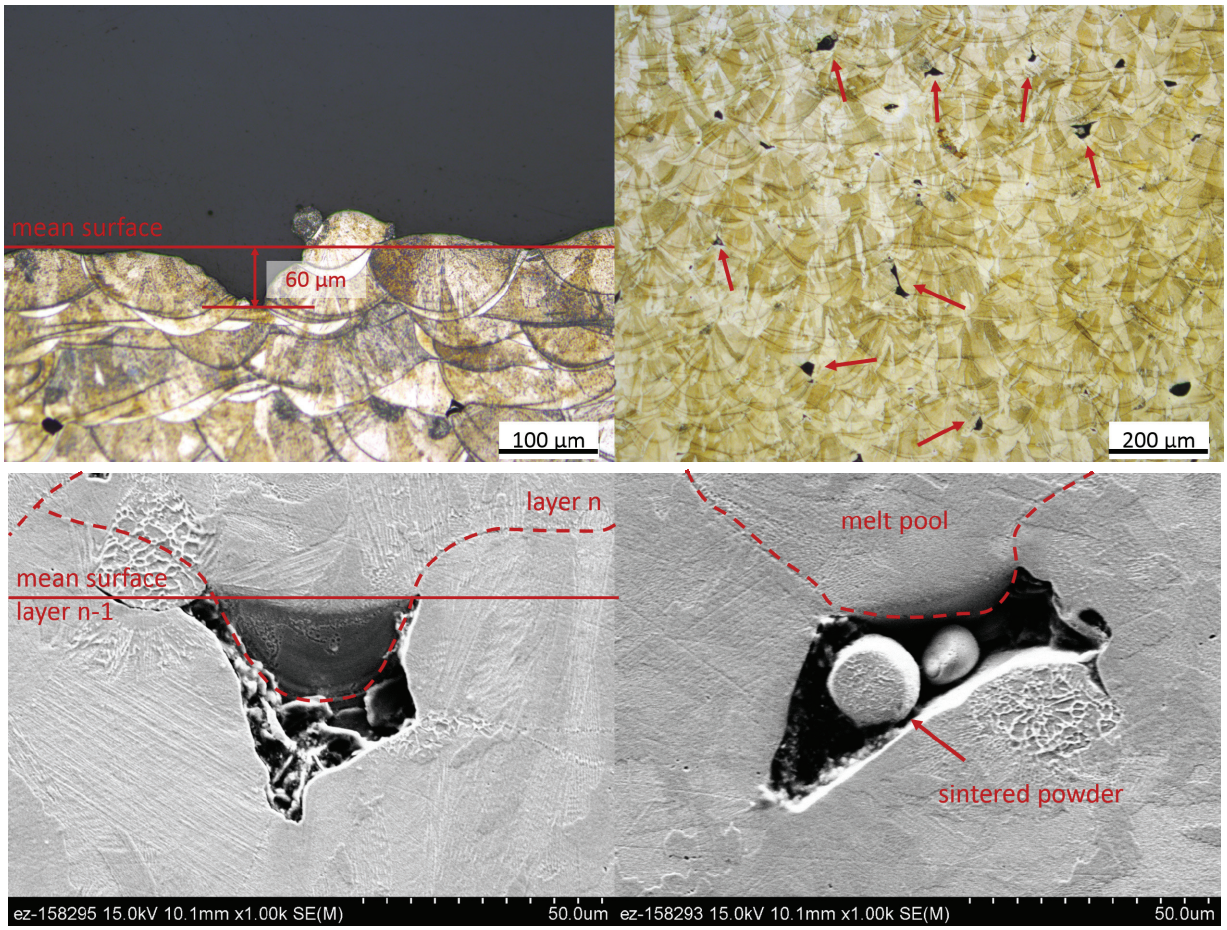

Figure 56 Origin of pores with the Renishaw standard parameter ($P = 180$ W; $t = 100$ µs)
Top: Rough SLM surface (left) and etched surface (right) with pores visible between two melt pools
Bottom: SEM images of pores resulting from low energy input

Recommendation: To make the process less sensitive to warping, it is recommended to replace the silicone rod with a carbon fiber brush. Since use of a carbon fiber brush entails exertion of little to no force on the parts during powder application, the process reliability can be significantly increased. In addition, the parameter window can be increased significantly for following investigations, since a carbon fiber brush is not as prone to warping as a silicone rod. To print parts with a density of 99.9 - 100%, the hatch spacing should be reduced to a value of approximately 100 µm or less. It should be noted that a reduction of the hatch spacing increases the build time. To determine optimal hatch spacing, a parameter variation is required.

6.2 Section 2: Weld Pool Shape

Single Tracks: The large standard deviations, especially in the measurements for melt pool area, indicate a high level of variance. This is likely related to the surface roughness, as discussed in the previous section. Since the single tracks are exposed on a mini substrate plate previously generated using SLM, considerable local variations in layer thickness can also occur here due to surface roughness. The layer thickness largely determines the amount of molten powder particles and, thus, the melt pool area. The position at which the melt pool in the x-y-plane is measured is also important. Assuming a melt pool width of 100 µm and point spacing of 70 µm, the melt pool width can differ up to 28 µm due to the point-wise exposure depending on the position of measurement (*Figure 57*). In addition, the number of melt pools available for evaluation (four per parameter combination) is relatively low. The discussed measurement error could also be the cause of the fluctuations of the curves for the melt pool shape.

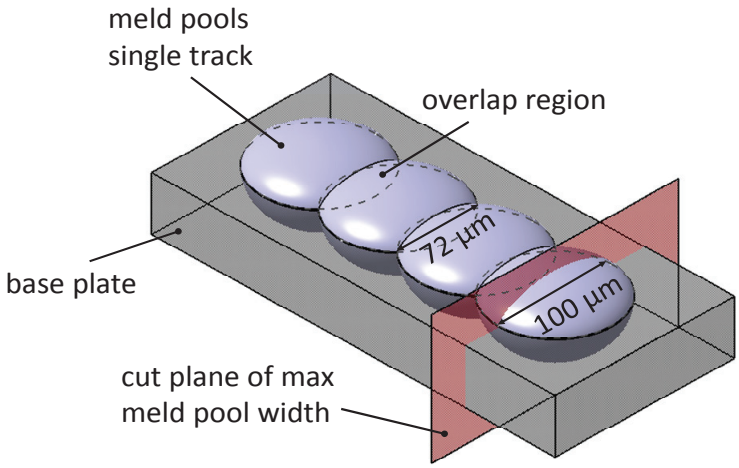

Figure 57 Schematic view of the measurement error due to the point-wise exposure

Skin Tracks: The evaluation of the skin tracks does not help in terms of the measurement errors described in the previous section. However, the standard deviation is decreased in comparison to that of the measurements for the single tracks. This is due to the fact that a larger number of melt pools can be evaluated (25 - 35 pieces). Therefore, the results of the skin tracks

are more reliable. Also, the resulting graphs make more sense, since the melt pool dimensions constantly increase with increase in the volume energy. The melt pool shape, in contrast, stays constant, independent of the volume energy input.

Comparison of Single Tracks and Skin Tracks: Due to the previously discussed measurement error present in the evaluation of single tracks, a comparison of single track and skin tracks in terms of melt pool area, melt pool height, and melt pool width will be omitted. In contrast, the shape of the melt pool should be insensitive, because they are dimensionless. However, a relatively large difference between the melt pool shape of the single tracks and skin tracks is observed. The melt pool shape of single tracks is more circular, while that of the skin tracks is more elliptical. One possible reason for this could be the different exposure strategies between skin tracks and single tracks.

As determined by the Renishaw machine, the exposure of the single tracks is carried out manually after completion of their actual construction, which requires a cool down of the components before they can be printed manually. The exposure of single tracks, therefore, takes place at room temperature. In contrast, the exposure of skin tracks takes place at a preheating temperature of 150°C and is completed by the system automatically (last exposed layer). The hatch spacing of the scan vectors in the case of single track exposure is approximately 1 mm. In contrast, the hatch spacing of skin tracks is only 125 µm. Consequently, the exposure of the single tracks and skin tracks occurs at significantly different temperatures. The temperatures present in the part could have an impact on the surface tension, viscosity, and Marangoni flow in the melt. This, in turn, affects the shape of the solidifying melt pool.

According to Schulze [34] and Czerner [41], the viscosity and the surface tension decreases in the pure materials but also in a number of alloys with increasing temperature. That means the surface tension temperature gradient $d\gamma/dT$ is negative. Hence, the surface tension in the melt pool boundaries is relatively large if the solidified material surrounding the melt pool is relatively cold. The resulting force is calculated as:

6.1

$$\gamma = \gamma_0 + \left(\frac{d\gamma}{dT}\right) \cdot T$$

This positive, i.e. outward, force is the cause of a flow (Marangoni convection), which is referred to as "divergent". The heat transported to the melt pool boundaries by the intense divergent flow causes a wide, flat melt pool (*Figure 58*, top). Various surface-active elements that are present in the solute segregate in the surface region of the melt pool and often extremely reduce the surface tension. With increase in temperature, the solubility of these elements is reduced, which again increases the surface tension. The resulting force and, therefore, also the convergent melt flow is now directed inward and produces a deep, considerably narrower melt pool (*Figure 58*, bottom) [34].

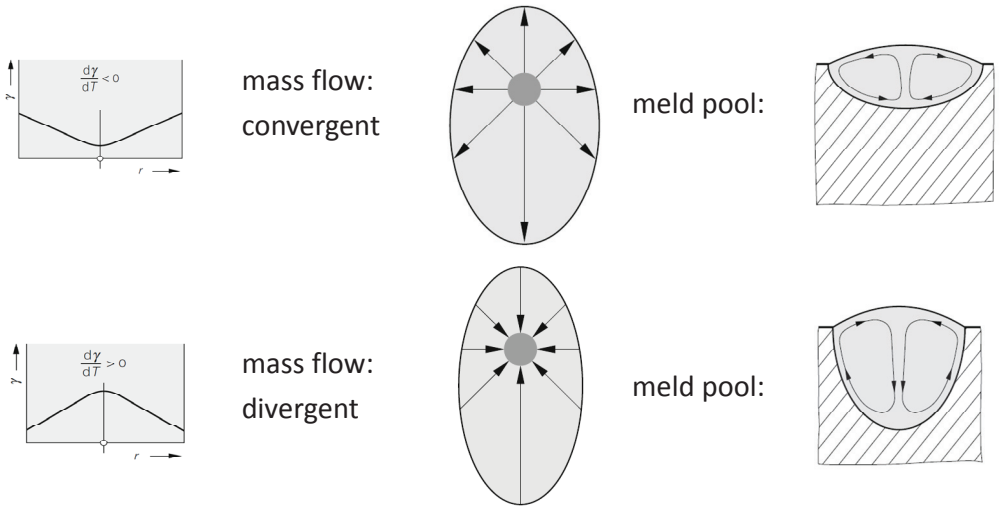

Figure 58 Meld pool shape depending on the direction of the Marangoni convection [34]

6.3 Section 3: Deformation due to Residual Stress

Twincantilevers: The upward bending of all twincantilevers is almost identical. It follows that the scan velocity (defined by the exposure time, among other parameters) and the laser power have relatively little influence on the resulting residual stresses in the SLM process. Similar results have been reported by Kruth et al [26] and Shiomi et al [28]. The alloy used by Kruth et al [26] is a chromium-molybdenum steel (JIS SCM440) and by Shiomi et al [28] is a Ti-6Al-4V and AISI 316L stainless steel. Furthermore, it can be shown that the melt pool dimensions (*Section 2*) likely have no effect on the residual stresses in SLM parts, since a significant

change in the melt pool dimensions is found in *Section 2*. However, this is not reflected in the upward bending height of the twincantilever.

Cause of the Upward Bending: The upward bending in z-direction can be explained by the temperature gradient model (TGM) or the cool down model (CDM). Both models are described in detail in the chapter "Basics". Residual stress profiles as a function of the build height in the x-direction were determined experimentally by Mercelis and Kruth [27] and Shiomi et al [28]. In these works, the residual stress distribution of rectangular blocks built with SLM is studied. Shiomi et al [28] report a high internal tensile stress of the same magnitude as the tensile strength in the uppermost layers of the components followed by a sharp drop to a small tensile stress in the middle of the part. Tensile stress is again present close to the substrate plate (*Figure 59*, left).

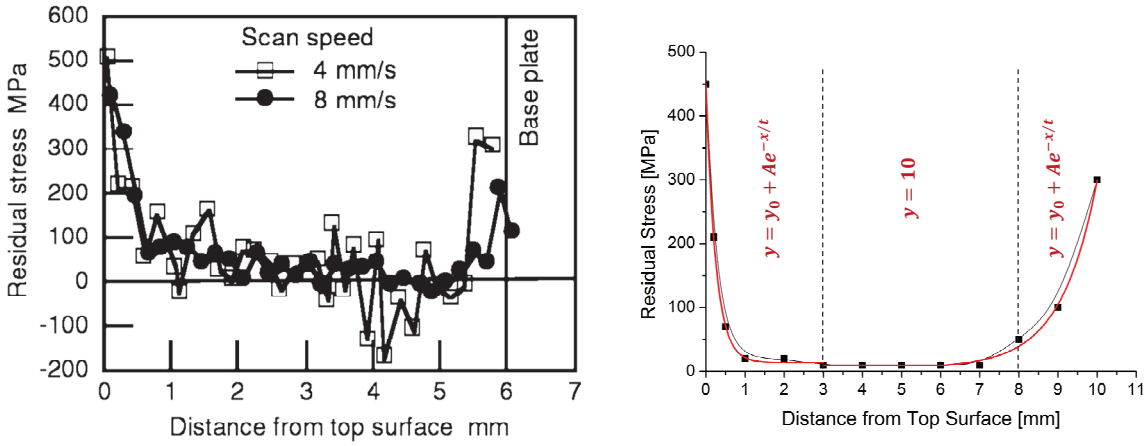

Figure 59 Residual stress distribution of a SLM model according to [28] (left); Fit curve for mathematical use (right)

In order to mathematically prove the bending of the twincantilever in z-direction of the residual stress, the distribution shown in *Figure 59* (right) is assumed. Furthermore, the following additional assumptions are made:

- The residual stress profile is similar to that shown in *Figure 59* (left).

- The maximal tensile stress in the uppermost layers corresponds to the average tensile strength of 750 MPa found in *Section 5.5*.

- The triangular block at the end of the twincantilever arm is neglected.

In order to use the residual stress distribution in *Figure 59* (left) for mathematical calculations, the residual stress distribution has to be replaced by mathematical functions *Figure 59* (right). For this purpose, fit functions are used. In the range x = 0 to x = 3, an exponential fit curve of the form:

6.2 $$y_{1(x)} = y_{3(x)} = y_0 + Ae^{-x/t}$$

is used. Where $y_0 = 3.43$, $A = 752.63$, and $t = 0.493$. The range of x = 3 to x = 6 is replaced by a horizontal fit function of:

6.3 $$y_{2(x)} = 10$$

The range of $x = 6$ to $x = 10$ is approximated by an exponential fit curve again (*Equation 6.3*). Where $y_0 = -253.57$, $A = 58.43$, and $t = -4.02$. The approximate residual stress curve is shown in *Figure* 59 (right).

In order to calculate the deformation in the positive z-direction, the center of gravity of the twincantilever in the z-y-plane is needed. In addition, the force application point due to the residual stresses must be calculated. If the center of gravity is located above the force application point, a positive moment results, and an upward bending in positive z-direction is the consequence.

Since the dimensions of the twincantilever varies in x-direction, the center of gravity is calculated by smearing the center of gravity of the twincantilever arm and the twincantilever arm plus supports. Distributed over the length of the twincantilever, there are 27 supports with a width of 1 mm and 26 spaces with a width of 0.8 mm. Assuming a cut height of 1 mm, the center of gravity in the x-z-plane is $x_c = 2.54$ mm starting from the upper edge of the twincantilever.

The point of force application is calculated by using the previously discussed fit curves according to *Equation 6.4*. It should be noted

here that the *x* coordinate is counted in a positive direction from the top of twincantilevers.

6.4

$$x_L = \frac{\int_A x dA}{\int_A dA} = \frac{\int_0^3 \int_0^{y_{1(x)}} x dy dx + \int_3^6 \int_0^{y_{2(x)}} x dy dx + \int_6^{10} \int_0^{y_{3(x)}} x dy dx}{\int_0^3 y_{1(x)} dx + \int_3^6 y_{2(x)} dx + \int_6^{10} y_{3(x)} dx}$$

By plugging *Equations 6.2 and 6.3* into *Equation 6.5*, the force application point is found to be $x_S = 6\ mm$. Thus, the force application point is below the center of gravity (*Figure 60*), and a delay in the twincantilever should be in positive z-direction.

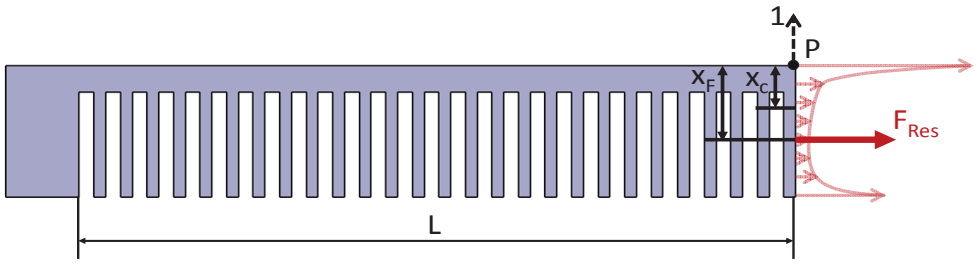

Figure 60 Schematic representation of residual stress distribution and resulting force on a twincantilever

The calculation of the displacement of point *P* is performed according to the principle of virtual force. Here, the unit of force is applied at the point *P* and points upward (in positive direction) (*Figure 60*). The upward bending can then be calculated with *Equation 6.5*.

6.5

$$v_P = \int_0^L \frac{Mm}{EI} dx$$

Here, *M* is the course of the moment due to the resulting force, and *m* is the course of the moment due to virtual force. The courses for *M* and *m* are:

6.6

$$M = \left(\int_0^3 y_{1(x)} dx + \int_3^6 y_{2(x)} dx + \int_6^{10} y_{3(x)} dx \right) \cdot b \cdot (x_F - x_c)$$

6.7

$$m = x$$

Here, b is the width of the twincantilever, and $(x_F - x_C)$ is the distance between force application point und center of gravity, hence the moment arm. To calculate the displacement in z-direction of point *P, Equations 6.6* and *6.7* are plugged into *Equation 6.5*:

6.8

$$v_P = \int_0^L \left(\frac{\left(\int_0^3 y_{1(x)} dx + \int_3^6 y_{2(x)} dx + \int_6^{10} y_{3(x)} dx \right) \cdot b \cdot (x_F - x_c) \cdot x}{EI} \right) dx$$

Where L is the length of the twincantilever arm. The following numerical values are used:

- The functions for $y_{1(x)}$, $y_{2(x)}$, and $y_{3(x)}$ are given in *Equations 6.2* and *6.3.*
- The length L of the twincantilever arm is 50 mm.
- The Young's modulus is 204 GPa according to the findings in *Section 5.*
- Since the twincantilever arm varies in x-direction, a similar strategy as that used as for calculating the center of gravity is used to calculate the area moment of inertia. Hence, the area moment of inertia is smeared for the whole twincantilever length. Again, a cutting height of 1 mm is assumed. Thus, the area moment of inertia for the twincantilever arm $I = 271\ mm^4$.

Substitution of these numerical values in *Equation 6.8* results in a displacement of point P of $v_P = 1.85$ mm. This result reflects the experimental results of *Chapter 5.3* pretty well. However, it should be noted that some strong assumptions have been made. In the experiments described in *Chapter 5.3,* a maximum deformation of the twincantilever in z-direction of 2.1 mm on average was measured.

Reason for Small Deformation in z-Direction: Contrary to expectations, the deformation in z-direction of the twincantilevers is only 2.1 mm and, therefore, relatively small. The small deformation can be explained by the low cut height of only approximately 1 mm right above the substrate plate. The lower the cut height, the higher the area moment of inertia and, thus, the resistance to bending. Usually the cut height is approximately 5 mm in the middle. The cut height of the twincantilever in this work

was only 1 mm due to a misunderstanding with the technician. The effect of different cut heights on the deformation in z-direction is illustrated by Castigliano's second theorem [42]. In the case of beams, Castigliano's Theorem is:

6.9

$$v_i = \int_0^L \frac{M_{(x)}}{EI_i} \frac{\partial M_{(x,P)}}{\partial P} dx$$

If a constant area moment of inertia is assumed, it can be taken out of the integral. Furthermore, it is assumed that the moment curves are identical for both cut heights. Consequently, the ratio of the deformation in z-direction of two twincantilevers built with the same material but different cut heights is only dependent on the area moment of inertia (*Equation 6.10*).

6.10

$$\frac{v_1}{v_2} = \frac{I_2}{I_1}$$

The area moment of inertia of the twincantilever at a cut height of 1 mm is approximately $I_2 = 271$ mm^4. The area moment of inertia at a cut height of 5 mm is approximately $I_1 = 50$ mm^4 and, thus, is less than one-fifth. If the previously calculated deformation in z-direction $v_2 = 1.85$ mm is used, the resulting deformation in z-direction for a cut height of 5 mm is approximately $v_1 = 10$ mm. Thus, the relatively low deformation in z-direction at a cut height of 1 mm is secondary to the five times higher area moment of inertia.

Recommendation: Since the low deformation in z-direction of the twincantilever is due to the low cut height, the cantilever beam thickness of 2 mm is appropriate and should not be reduced. As shown, the cut height has a significant impact on the amount of deformation in z-direction. If the beam thickness is reduced and simultaneously the cut height is increased, there is a risk that the residual stress will exceed the tensile strength, and the twincantilever arms will break during wire EDM. However, it should be ensured in the future that the proper cut height is maintained.

At first glance, the bridges seem to be a better alternative for a qualitative residual stress measurement. The height and volume are smaller in comparison to the twincantilever. Thus, the build time is shortened. Moreover, more parts can be produced during each build job, given the small size of the bridges. However, the disadvantage is the low deformation, which is visually not apparent. This can lead to measurement errors or make a

measurement with the FARO Laser Scanner impossible. For this reason, twincantilevers are recommended for qualitative residual stress measurement.

6.4 Section 4: Microstructure

According to Atushi et al [8], it is known that the γ-phase is dominant in CoCrMo SLM parts. Therefore, a phase analysis by means of x-ray diffraction is omitted. In contrast to the findings presented by Atsushi et al [8], no precipitates are found in the microstructure. A fine cellular microstructure ensues. The conditions for cellular growth are described in *Chapter 3.3.3* ("Basics") according to Dilthey [23], David and Vitek [33], and Schulze [34]. According to David and Vitek [33], the conditions for cellular grain growth are a high solidification front growth rate with an associated constitutional undercooling and a high temperature gradient. In general, it is difficult to draw a conclusion as to the solidification behavior, since it is not possible to identify the feed direction of the laser beam and exact position of the cutting plane relative to the melting trace in retrospect. In addition, the analysis of the microstructure is further complicated by the overlapping of melt pools of different layers.

Influence of Laser Power and Exposure Time (or Rather Scan Velocity): The influence of the laser power and the scan velocity is relatively low. Since a very fine microstructure with a cell spacing of only 0.4 – 0.6 µm is present, a relatively large uncertainty is expected for the EDS point analysis. For this reason, the discussion of the EDS analysis is omitted. Although precipitations or enrichment of grain boundaries with chromium or molybdenum would be theoretically possible (*Figure 61*).

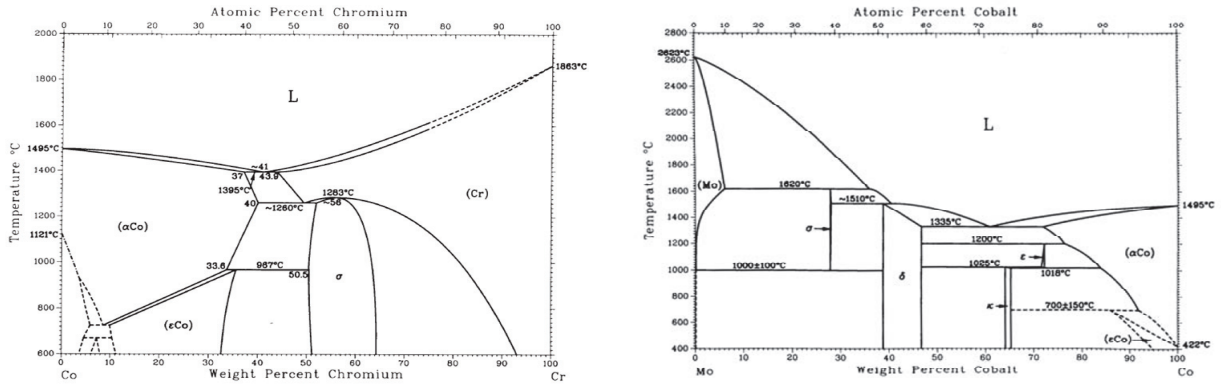

Figure 61 Binary phase diagrams of Co-Cr and Co-Mo alloys [1]

EBSD and Grain Size: The EBSD analysis shows elongated grain growth in build direction, i.e., in the direction of the largest temperature gradient. Here, a reduction in the exposure time leads to smaller grains. According to David and Vitek [33], rapid solidification conditions lead to greater supercooling of the melt and promote an increased nucleation. For this reason, solidification starts with a larger number of grains which grow in the direction of the largest temperature gradient. This results in a larger number of smaller or thinner grains.

The coarsening of the grains with the increase in laser power could be associated with the enlargement of the melt pool. If the melt pool is larger, the melt remains in liquid form longer, and the grains have more time to grow. However, when varying the laser power, the grain size difference is not as large as in the variation in the exposure time.

A preferred crystalline direction is not identifiable on the basis of the evaluated EBSD images.

6.5 Section 5: Tensile Test

Influence of Position on the Base Plate: The position of the tensile blocks on the base plate has a huge influence on the resulting yield stress, tensile strength, elongation, and strain energy. During the construction of the tensile blocks, a reduced amount of spark formation was observed locally. This is an indicator of low energy input into the powder bed. A very obvious change in spark formation was observed during the build of tensile block 1 with an angle of 0° to the build direction (*Figure 62*). This tensile block will be subsequently referred to as 1-0° for the sake of simplicity and further investigated. Tensile block 3 with an angle of 0° to the build direction is used as a reference, which is further referred to as 3-0° (*Figure 62*). Tensile block 3-0°, in contrast to tensile block 1-0°, shows ordinary spark formation during exposure. Tensile block 1-0° is built with a laser power of 160 W and an exposure time of 100 µs. Tensile block 3-0° is built with a laser power of 200 W and an exposure time of 100 µs. According to *Section 1*, the relative density of both tensile blocks should lay between 99.1 and 99.8%. The resulting stress-strain curves as a function of position on the base plate are shown in *Figure 62*. While the stress-strain curves remain relatively similar for tensile block 3-0°, the stress-strain curves of tensile block 1-0° differ greatly. The greater the distance from the center of the substrate plate, the lower the yield stress, tensile strength, elongation, and strain energy. For tensile block

1-0°, for example, the tensile strength falls from 825 MPa to approximately 375 MPa.

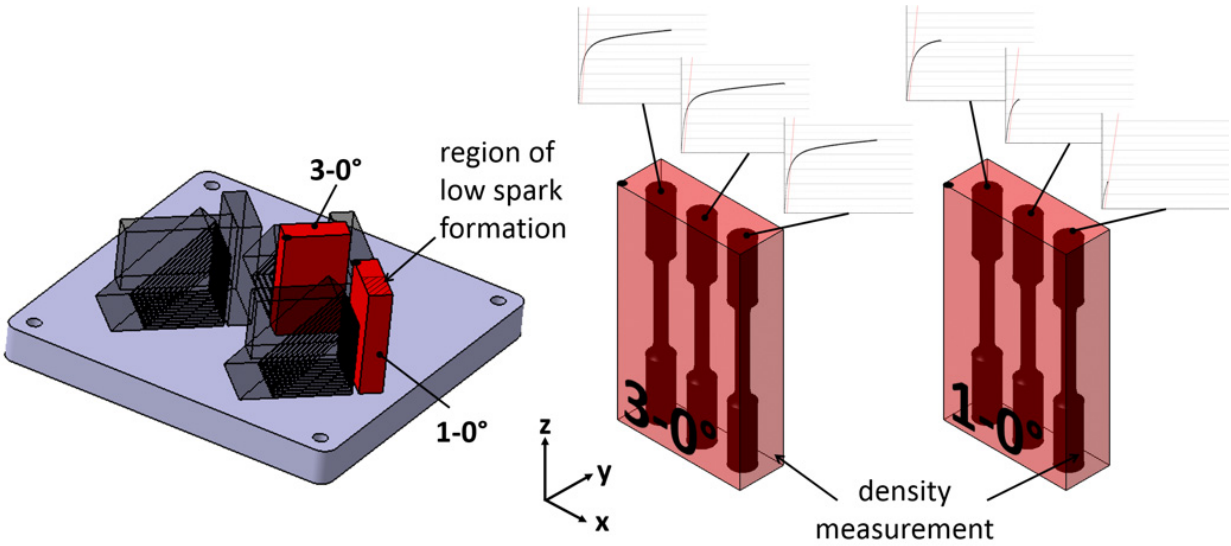

Figure 62 Position of the tensile blocks on the base plate (left) and stress strain curves corresponding to the blocks

For this reason, the densities of the two tensile blocks (1-0° and 3-0°) are determined as a function of height. As shown in *Figure 63* the density is measured at the outermost edge of the tensile block. In each case, 3 × 22 images (y-direction and z-direction) are taken and evaluated. The densities of the samples in *Section 1* are used for reference.

The density of tensile block 3-0° remains constant over almost the entire height and is 99.8%. At a height of approximately 70 mm, the density falls sharply to approximately 96.6% (*Figure 63*). However, the tensile specimens are not affected, because the density drop occurs only in the grip section. The density in tensile block 1-0° is 92% on average, which is 7% below the expected value from *Section 1* (99.1%). In addition, the density varies greatly and falls to a minimum of 88.8% at a height of about 40 mm (*Figure 63*). Due to the high porosity, the area of the specimen is reduced, which has a significant influence on the mechanical properties of the tensile specimen.

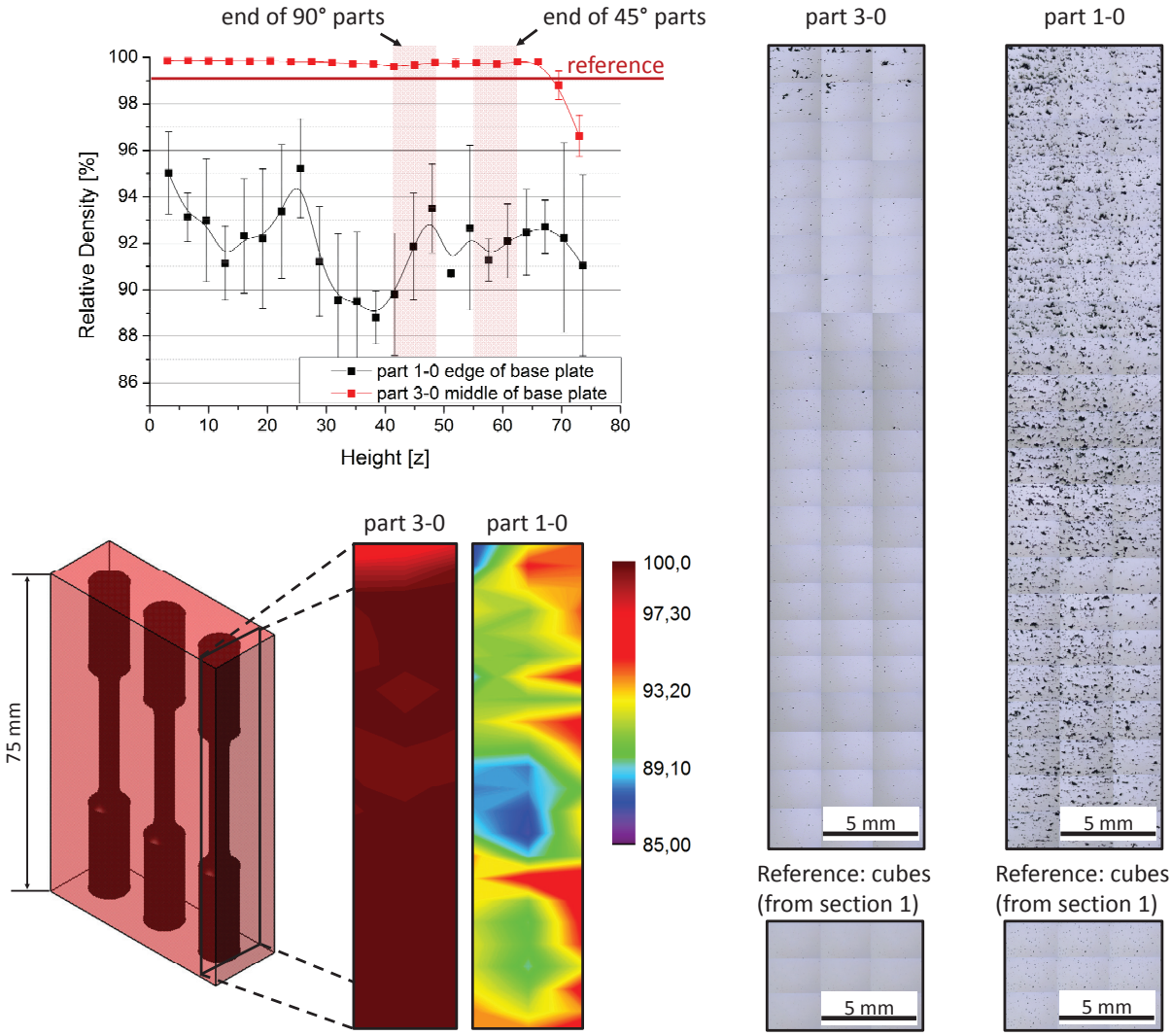

Figure 63 Relative density of the parts 3-0° and 1-0° vs. the build height (upper left); 2D density map of parts 3-0° and 1-0° (lower left); transverse cut of parts 3-0° and 1-0° (right)

One possible explanation for the low density and associated poor mechanical properties are the long construction time and resulting soot in the process chamber and the protective glass of the lens (*Figure 64*). Over time, more and more soot covers the protective glass in front of the lens, and the transmittance of the protective glass decreases. Since the laser beam is not focused directly on the lens, the energy is not sufficient to burn off the soot. Consequently, a part of the energy is coupled into the protective

glass and fails to melt the powder. However, it is not clear why there is no soot in the middle part of the protective glass.

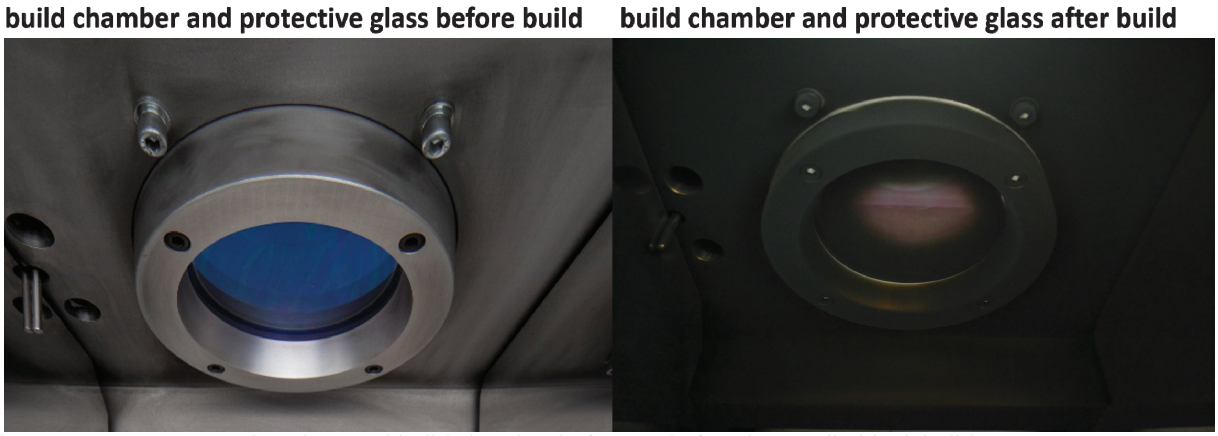

Figure 64 Protective glass and build chamber before and after the tensile block build

Influence of Laser Power (t = 100 µs = const.): With increasing laser power, yield strength, tensile strength, elongation, and strain energy are increased. According to the Hall-Petch relationship [24], a finer grain size increases the yield strength:

6.11

$$\sigma_Y = \sigma_0 + \frac{k}{\sqrt{d}}$$

with: σ_Y = *Yield stress*
σ_0 = *material constant*
k = *strengthening coefficient*
d = *average grain diameter*

The Hall-Petch relationship states that the movement of dislocations is prevented by grain boundaries. This results in a higher yield strength due to a larger number of grain boundaries.

This contradicts the results found in *Section 4* (EBSD and Grain Size). However, the results found in *Section 5* (tensile strength) can likely be ascribed to a superimposition of two effects, On the one hand, yield stress is increased by grain refinement. On the other hand, tensile strength is lessened by a significant reduction in

density depending on its position on the base plate. As the investigations demonstrate, the reduction in density can be as high as 10%. Consequently, the prevailing stress in the tensile specimen is significantly increased. This effect is probably stronger than the grain boundary strengthening of the material. Thus, the results of *Section 5* must be viewed critically.

Influence of Angle to the Build Direction: The influence of the build direction of the parts can also be explained by Hall-Petch relationship (*Equation 6.11*). The results from *Section 4* (microstructure) provide different grain sizes depending on the measurement plane (horizontal vs. vertical). This is caused by the growth of elongated grains in the build direction. The result is the anisotropic behavior of the printed parts.

Comparison with Other Works: Investigations with a similar CoCrMo alloy were performed by Atsushi et al [8]. Atsushi et al used a constant laser source. The influence of laser power and layer thickness on yield strength, tensile strength, and elongation was examined. A mean yield stress of approximately 507 MPa and a mean tensile strength of approximately 928 MPa were reached. The elongation was ca. 13.2% on average. In comparison, the yield strength and tensile strength for cast alloys is approximately 450 MPa or 655 MPa, and the elongation is approximately 10%. In this work, a mean yield stress of approximately 750 MPa and a mean tensile strength of approximately 1050 MPa were achieved. The elongation was approximately 6% in average. The values achieved in the work by Atsushi et al [8] and the values achieved in this work are summarized in *Table 14*.

Table 14 Comparison of the results of the investigations performed by Atsushi et al [8], this work, and the ASTM standards

	Condition	Yield Stress [MPa]	Tensile Strength [Mpa]	Elongation [%]
Popp	SLM (pulsed)	(450) **750** (100)	(600) **1050** (1200)	(1.8) **6** (9.5)
Atsushi [8]	SLM (const.)	(496) **507** (516)	(911) **928** (911)	(10.7) **13.2** (16.4)
ASTM F75 [1][13]	cast	**450**	**655**	**8**

7 Summary

In the present work, the correlation between SLM process parameters and the resulting microstructure and mechanical properties are studied. The material used for this purpose is a Co-based alloy with the main alloy components Co (ca. 65 wt%), Cr (ca. 28 wt%), and Mo (ca. 5.5 wt%).

The strategy used in this work involves the systematic investigation of SLM process parameters on the mechanical properties of SLM components. Furthermore, various factors that may have an effect on the mechanical properties are investigated. Possible sources of error include, for example, different densities, microstructures, or residual stress states. For a detailed examination of these error sources, the work is divided into five subsections.

To keep the potential error due to density differences low, a parameter window is determined in *Section 1.* All parameters found in the parameter window should have a density > 99%. The influence of laser power and the exposure time on the density is investigated. The greater the volume energy, the greater the density of the components. Parts with a density nearing 100% can be produced. However, if the volume energy exceeds a certain level, warping begins during the construction, and the silicon rod can be damaged. For this reason, the parameter window must be limited to parameter combination, with which a relative density of not more than 99.8% is achieved. In both cases (laser power variation and exposure time variation), a volume energy of 61 J/mm³ leads to a density of 99.1%, and a volume energy of 76 J/mm³ leads to a density of 99.8%. The results from *Section 1* form the basis for all further studies.

In *Section 2*, the influence of laser power and exposure time on the melt pool dimensions and the melt pool shape are examined. The melt pool increases if the volume energy is increased. Similar to the study of the density, it is irrelevant whether the increase in the volume energy is achieved by increasing the laser power or the exposure time. The melt pool width increases from approximately 120 to 140 µm with an increase in volume energy from 61 to 76 J/mm³. At the same time, the melt pool height increases from about 70 to 80 µm. The effect of volume energy on the shape of

the melt pool is not significant. All melt pools have an elliptical shape.

In *Section 3*, a qualitative measurement of residual stresses by the means of twincantilevers is carried out. The deformation of the twincantilever arms is 2.1 mm on average. The biggest difference between maximum and minimum deformation in z-direction is only 300 µm. Hence, the influence of laser power and exposure time on residual stresses is very small. Consequently, no trend can be seen, and it is assumed that the residual stress distribution in all components is similar.

In *Section 4*, the microstructure of the samples is examined by means of SEM. Due to the rapid solidification conditions in the SLM process, a fine cellular microstructure is formed. The orientation of the cells varies. Cell growth is usually epitaxial on previously solidified melt pools. The cell spacing is 0.4 – 0.6 µm.

For a more in-depth investigation, EBSD analysis is additionally applied. This makes the grain boundaries, which were previously not visible, evident. An increase in the volume energy results in an increase in the grain size. Variation in the exposure time has a greater influence than variation of the laser power. The grain growth takes place in build direction. During solidification, elongated grains occur, which are typical for the SLM process.

In *Section 5*, the study of the mechanical properties is performed by means of tensile testing. Due to time constraints, only the influence of the laser power (the influence of the exposure time is omitted) on yield stress, tensile strength, elongation, and strain energy can be investigated. In the tensile test, the predicted anisotropy (*Section 4*) is confirmed due to the presence of elongated grains in build direction. Parts with an angle of 0° (parallel to the build direction) have, on average, a lower tensile strength and yield strength than parts that possess an angle of 90° (normal to the direction structure). Increasing the laser power results in an increase in yield stress, tensile strength, elongation, and strain energy. However, it should be noted that the position on the baseplate has a significant impact on the density of the parts and, hence, on the mechanical properties. A maximum yield stress of approximately 1000 MPa and a maximum tensile strength of 1200 MPa is determined. The yield stress is on average 680 MPa, and the tensile strength is on average 1100 MPa.

8 Future Work

Since the available process parameters provided by Renishaw are not fully developed, further optimization of these parameters is recommended. A target density of 100% should be pursued. The investigations carried out in this work indicate that the hatch spacing chosen by Renishaw is much too large.

Furthermore, it would be appropriate to replace the silicone lip in the Renishaw machine with a carbon fiber brush. This would offer the advantage that the powder application tool would be less sensitive in the case of warping. At the same time, the parameter window could be further extended towards greater volume energy, which might be interesting from a scientific standpoint. Another advantage would be that microstructural changes may be more easily accomplished by process parameters that extend beyond the current possible parameter window.

In terms of residual stresses in SLM investigations, Kruth et al [26], Over [29], and Buchbinder et al [30] demonstrated that the preheat temperature and scan strategy have the biggest impact on residual stresses. Since the maximum possible preheat temperature is defined by the SLM machine implemented and, thus, cannot be increased in the case that a higher temperature is desired (particularly relevant for super alloys), a better way to reduce residual stresses in SLM would be a smart scan strategy. Kruth et al [26], Over [29], and Buchbinder et al [30] showed that the orientation of the scan vectors has a significant influence on the resulting residual stresses. For example, the delay of twincantilevers or bridges in z-direction is lower if the orientation of the scan vectors is the x-direction versus the y-direction (*Figure 8*). In my opinion, this is not directly related to a reduction in the residual stresses but due to a reorientation of the largest residual stresses towards the axis with the largest area moment of inertia and, hence, the highest resistance to bending. This could be used to develop software that sorts the scan vectors layer by layer so that they always point in a favorable direction in terms of the area moment of inertia. The purpose would be for the highest resulting residual stresses to always act in in the direction of the greatest area moment of inertia.

The studies pertaining to the tensile test reveal that the results are largely dependent on the position of the samples on the base plate. It would be interesting to investigate the cause of this in more detail in the future. As an initial point of study, it should be identified at which position on the base plate (xy plane) density variations occur. In addition, it would be worth investigating to what extent the build height effects the grain size of the specimens. This could not be accommodated in this work due to the enormous time expenditure it would require.

List of References

[1] J. R. Davis, Nickel, Cobalt and Their Alloys, Materials Park, OH 44073: ASM International, 2000.

[2] C. Flege, F. Vogt, S. Höges, L. Jauer, M. Borinski, V. Schulte, R. Hoffmann, R. Poprawe and W. Meiners, "Development and characterization of a coronary polylactic acid stent prototype generated by selective laser melting," *Journal of Materials Science: Materials in Medicine,* vol. 24, no. 1, pp. 241-255, 24 January 2013.

[3] W. Meiners, Direktes Selektives Laser Sintern einkomponentiger metallischer Werkstoffe, Aachen, Germany: Shaker, 1999.

[4] I. Gibson, D. W. Rosen and B. Stucker, Additive Manufacturing Technologies, New York, NY 10013: Springer, 2010.

[5] B. Vandenbroucke and J.-P. Kruth, "Selective laser melting of biocompatible metals for rapid manufacturing of medical parts," *Rapid Prototyping Journal,* vol. 13, no. 4, pp. 196-203, 2007.

[6] D. Jevremovic, T. Puskar, B. Kosec and D. Vukelic, "The analysis of the mechanical properties of F75 Co-Cr Alloy for use in selective laser melting (SLM) manufacturing of removable partial dentures (RPD)," *Metalurgija,* pp. 171-174, April 2012.

[7] A. Gatto, S. Bortolini and L. Iuliano, "Characterization of Selective Laser Sintered Implant Alloys: Ti6Al4V And Co-Cr-Mo," in *Global Product Development*, Springer, 2010, pp. 729-736.

[8] T. Atsushi, Suyalatu, N. Takayuki, J. Natsuka, N. Naoyuki, T. Yusuke, M. Satoshi, D. Hisashi, K. Shingo, C. Akihiko, W. Noriyuki, I. Yoshimasa and H. Takao, "Microstructures and mechanical properties of Co-29Cr-6Mo alloy fabricated by selective laser melting process for dental applications," *Jornal of the Mechanical Behaviour of Biomedical Materials,* no. 21, pp. 67-76, May 2013.

[9] X. Xian-Zhen, C. Jie, X. Nan and W. Bin, "Surface Properties and Corrosion Behavior of Co–Cr Alloy Fabricated with Selective Laser Melting Technique," *Cell Biochemistry and Biophysics,* vol. 67, no. 3, pp. 983-990, 2013.

[10] H. Yolanda, Q. Bin, S. Zhijian, V. Sannakaisa and W. Inger, "In vitro biocompatibility of CoCrMo dental alloys fabricated by selective laser melting," *Dental Materials,* vol. 30, no. 5, pp. 525-534, 2014.

[11] B. Ralf, Handbuch Hochtemperatur-Werkstofftechnik, Braunschweig, Germany: Vieweg, 2001.

[12] J. Giacchi, C. Morando, O. Fornaro and H. Palacio, "Microstructural characterisation of as-cast biocompatible Co-Cr-Mo alloys," *Materials Characterization,* vol. 62, no. 1, pp. 53-61, 2011.

[13] ASTM Standard, *Standard Specification for Cobalt-28 Chromium-6 Molybdenum Alloy Castings and Casting Alloy for Surgical Implants,* West Conshohocken, PA: ASTM International, 2012.

[14] 3T RPT Ltd, "http://www.3trpd.co.uk/," July 2014. [Online]. Available: http://www.3trpd.co.uk/wp-content/uploads/2014/07/Cobalt-Chrome-Alloy-Co28Cr6Mo.pdf. [Accessed August 2014].

[15] J. Giacchi, Morando, O. Fornaro and P. H.A., "Microstructural characterization of as-cast biocompatible Co-Cr-Mo alloys," *Materials Characterization,* vol. 62, no. 1, pp. 53-61, 2011.

[16] M. McCelland, Interviewee, *MEng*. [Interview]. 20 August 2014.

[17] E. M. U. Wolfstieg, "Ursachen und Bewertung von Eigenspannungen," *Chemie Ingenieur Technik,* vol. 45, no. 11, pp. 760-770, 1973.

[18] J. Gibmeier, Zum Einfluss von Last- und Eigenspannungen auf die Ergebnisse instrumentierter Eindringhärteprüfung, Kassel: Kassel Univ. Press, 2004.

[19] K. H. Kloos, "Eigenspannungen, Definitionen und Entstehungsursachen," *Zeitschrift für Werkstofftechnik,* vol. 10, no. 9, pp. 293-332, 1979.

[20] T. Blaß, "http://www.metalle.uni-bayreuth.de," January 2004. [Online]. Available: https://view.officeapps.live.com/op/view.aspx?src=http%3A%2F%2Fwww.metalle.uni-bayreuth.de%2Fde%2Fdownload%2Fteaching_downloads%2FPrakt_Materialcharakterisierung_H4a%2FPrakt_H4a__Eigenspannungsmessung.doc. [Accessed 29 August 2014].

[21] F. Mücklich, "www.uni-saarland.de," October 2006. [Online]. Available: http://www.uni-saarland.de/fak8/wwm/praktika/PR_Methodik_I/MeI%20Anleitung%20V7%20-%20Eigenspannungsmessung.pdf. [Accessed 28 August 2014].

[22] E. Roos and K. Maile, Werkstoffkunde für Ingenieure, Stuttgart: Springer, 2004.

[23] U. Dilthey, Schweißtechnische Fertigungsverfahren 2, Aachen: Springer, 2005.

[24] G. Dieter, Mechanical Metallurgy, New York: McGraw-Hill, 1961.

[25] B. Vrancken, R. Wauthle, J. Kruth and J. Van Humbeek, "Study of the Influence of Material Properties on Residual Stress in Selective Laser Melting," *LayerWise NV,* vol. N/A, no. N/A, pp. 393-407, 2013.

[26] J.-P. Kruth, J. Deckers, E. Yasa and R. Wauthle, "Assessing and comparing influencing factors of residual stresses in selective laser melting using a novel analysis method," *Jornal of Engineering Manufacturers,* vol. 226, no. 6, pp. 980-991, 2012.

[27] P. Mercelis and J.-P. Kruth, "Residual stresses in selective laser sintering and selective laser melting," *Rapid Prototyping Journal,* vol. 12, no. 5, pp. 254-265, 2006.

[28] M. Shiomi, K. Osakada, T. Nakamura, T. Yamashita and F. Abe, "Residual Stress within Metallic Model Made by Selective Laser Melting Process," *CIRP Annals - Manufacturing Technology,* vol. 53, no. 1, pp. 195-198, 2004.

[29] C. Over, Generative Fertigung von Bauteilen aus Werkzeugstahl X38CrMoV5-1 und Titan TiAl6V4 mit Selective Laser Melting, Aachen: Shaker Verlag, 2003.

[30] D. Buchbinder, G. Schilling, W. Meiners, N. Pirch and K. Wissenbach, "Untersuchung zur Reduzierung des Verzugs durch Vorwärmung bei der Herstellung von Aluminiumbauteilen mittels SLM," *RT Journal,* vol. 8, no. 1, 2011.

[31] B. Künne, Einführung in die Maschinenelemente, Stuttgart: Teubner GmbH, 2001.

[32] H. Gugel, *Laserschweißen artgleicher und artfremder Maerialkombinationen mit Nickel-Titan Formgedächtnislegierungen,* Wuppertal, 2010.

[33] S. David and J. Vitek, "Correlation between solidification parameters and weld microstructures," *International Materials Reviews,* vol. 1, no. 34, pp. 213-245, 1989.

[34] G. Schulze, Die Metallurgie des Schweißens, Heidelberg: Springer, 2010.

[35] M. Wolf, *Zur Phänomenologie der Heißrissbildung beim Schweißen und Entwicklung aussagekräftiger Prüfverfahren,* Berlin: BAM, 2006.

[36] I. Yadroitesev, P. Krakhmalev, I. Yadroitsava, S. Johannsson and I. Smurov, "Energy input on morphology and microstructure of selective laser melting single tracks from metallic powder," *Journal of Materials Processing Technology,* vol. 213, no. 4, pp. 606-613, 2013.

[37] F. Verhaeghe, T. Craeghs, J. Heulens and L. Pandelaers, "A pragmatic model for selective laser melting with evaporation," *Acta Materialia,* vol. 57, no. 20, pp. 6006-6012, 2009.

[38] K. Kempen, L. Thijs, J. Humbeeck and J.-P. Kruth, "Mechanical properties of AlSi10Mg produced by Selective Laser Melting," *Physics Procedia,* vol. 39, pp. 439-446, 2012.

[39] Renishaw plc, Renishaw additive manufacturing system AM250, N/A: N/A, 2013.

[40] Renishaw plc, "http://www.renishaw.com/," Renishaw plc, 2011-2014. [Online]. Available: http://resources.renishaw.com/details/Build+volume+chamber+in+AM+machine(129748)(36390). [Accessed 10 11 2014].

[41] S. Czerner, Schmelzbaddynamik beim Laserstrahl-Wärmeleitungsschweißen von Eisenwerkstoffen, Hannover: N/A, 2005.

[42] L. Papula, Mathematische Formelsammlung, Wiesbaden: Vieweg + Teubner, 2009.

[43] T. Ostwald, Objekt-Identifikation Anhand Regionenbeschreibender Merkmale, Aachen: RWTH Aachen, 2005.

[44] R. Cook and Y. Warren, Advanced Mechanics of Materials, New Jersey: Prentice-Hall, 1999.

[45] S. Meister, *Grain and Particle Analysis with Line Intersection Method,* N/A: N/A, 2012.

Appendix

A1 Derivation of the Volume Energy for Constant and Pulsed SLM Systems

No derivation for the volume energy for pulsed laser systems is found. For this reason, the derivation is done similarly to the derivation of the volume energy for constant laser sources according to Meiners et al [3]. For the derivation of the two volume energies, *Figure 65* is used. For a better overview, the hatch spacing (left), and the point distance (right) have been depicted very large.

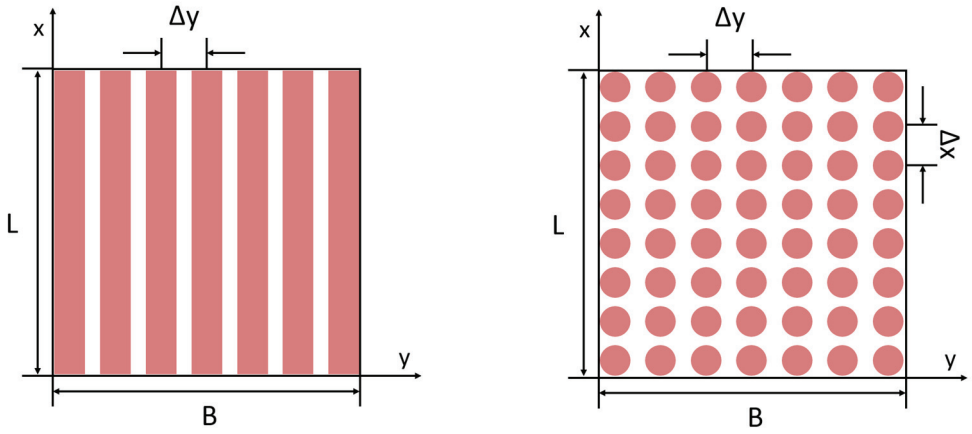

Figure 65 Schematic representation of the scan path (red) for constant (left) and a pulsed (right) laser source

The heat energy required to melt the powder is provided by laser radiation. The volume energy E_V radiated into the powder is

10.1
$$E_V = \frac{P_L t_{ww}}{V}$$

where: P_L = *laser power*
t_{ww} = *exposure time*
V = *volume of one layer*

The derivation of volume energy is based on *Equation 10.1* (where $L >> D_s$ und $B >> \Delta y$).

10.2
$$t_{ww} = n\frac{L}{v_s} \quad with \quad n = \frac{B}{\Delta y} \quad and \quad V = LBD_s$$

Substituting *Equation 10.2* in *Equation 10.1* yields the well-known formula from the literature used to calculate the volume energy in the case of a constant laser heat source (*Equation 10.3*).

10.3

$$E_V = \frac{P_L}{\Delta y \, D_s \, v_s}$$

where: P_L = *laser power*
Δy = *hatch spacing*
v_s = *scan velocity*
D_s = *layer thickness*

In order to derive the volume energy for a pulsed laser heat source, a similar approach is used. It is assumed that no time-dependent intensity change per pulse operation is performed. Point of departure is again *Equation 10.1*.

10.4

$$t_{WW} = n t_{Puls} \quad with \quad n = \frac{B}{\Delta x} \frac{L}{\Delta y} \quad and \quad V = LBD_s$$

Equation 10.4 substituted in *10.1* results in an equation used to calculate the volume energy for a pulsed laser heat source in SLM (*Equation 10.5*).

10.5

$$E_V = \frac{P_L \, t_{Puls}}{\Delta y \, \Delta x \, D_s}$$

where: P_L = *laser power*
t_{Puls} = *exposure time per pulse*
Δy = *hatch spacing*
Δx = *point distance*
D_s = *layer thickness*

A2 Real Layer Thickness and Filling Factor

Derivation of the Real Layer Thickness

Equation 3.11 (from Meiners et al [3]) is subsequently derived and explained to enable a better understanding.

In SLM, a compaction of the powder takes place as a result of laser irradiation. Thus, the melting of the powder causes the volume of the powder layer to decrease. The volume reduction is carried out by reducing the layer thickness in the *z* direction by the amount *d**. Consequently, the real layer thickness *d** differs from the (theoretical) layer thickness *d* defined in the software.

10.6
$$d^* = d(1 - a)$$

where: d*= real layer thickness (melted)
d = theoretical layer thickness (powder)
a = filling factor of the powder

Thereafter, the build platform is lowered by *z*, which corresponds to the theoretical layer thickness *d*, and a new powder layer is applied. Consequently, the thickness of the next layer of powder to be processed increases to:

10.7
$$d_i = z + d^*$$

where: z = lowering of the base plate
d= real layer thickness (melted)*
d_i = thickness of the i'th layer

If this consideration is repeated, the layer thickness as a function of the number of the applied layers results in a converging geometric row:

10.8
$$d_i = z \sum_{k=0}^{i-1} (1 - a)^k$$

where: d_i = thickness of the i'th powder layer
a = filling factor of the powder layer
z = lowering of the base plate

The derivation of the real layer thickness is shown in *Figure 66*.

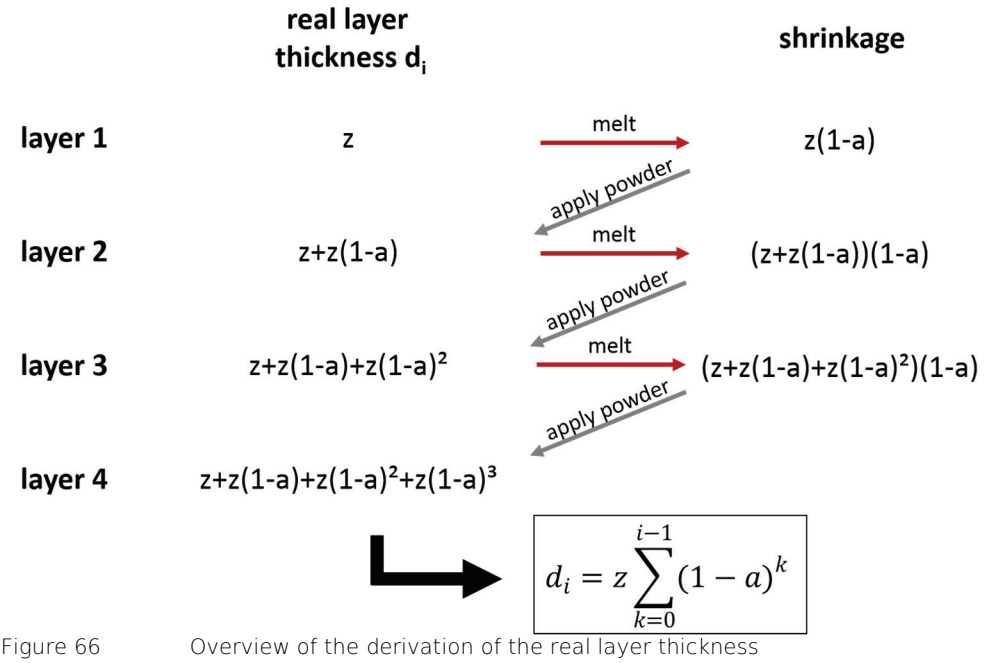

Figure 66 Overview of the derivation of the real layer thickness

Equation 10.8 is checked for convergence according to Papula [42]. Here, $q = 1\text{-}a$ is an auxiliary variable. In addition, $q < 1$, since $a > 0$.

10.9

$$set: \quad q = 1 - a \quad \rightarrow \quad \sum q^k = s_n$$

$$partial\ sums: \quad s_n = 1 + q + q^2 + \cdots + q^n \qquad (1)$$

$$qs_n = q + q^2 + \cdots + q^n + q^{n+1} \qquad (2)$$

$$(1) - (2): \quad s_n = \frac{1 - q^{n+1}}{1 - q} \quad \rightarrow \quad \lim_{n\to\infty} = \frac{1}{1 - q}$$

Substituting the result for $n \rightarrow \infty$ back into *Equation 10.8* results in a simple equation for calculating the real layer thickness according to:

10.10

$$d_{i\to\infty} = \frac{z}{a}$$

The geometric series in *Equation 10.8* converges relatively quickly to the constant value calculated with *10.10*. For example, if a layer thickness of 30 µm is used (as in this work) and a filling factor of 0.6 (typical for powder with the grain size distribution used in this work) is taken as basis, the layer thickness converges according to *Equation 10.8* for $n \to \infty$ to a real layer thickness of 0.5µm. This value is already reached after the first six layers. This finding is very important when it comes to the application of single tracks In order to mirror the build process as close to reality as possible.

Experimental Determination of the Filling Factor

In order to calculate the real layer thickness as described in *Chapter 10.2.1*, it is necessary to determine the filling factor *a* of a given powder first. The determination of the filling factor is carried out experimentally. By means of a measuring cup, a defined amount of powder is weighed. The determination of the filling factor is performed according to *Equations 10.11* and *10.12*.

10.11

$$\rho_{powder} = \frac{m_{powder}}{V_{powder}}$$

10.12

$$a = \frac{\rho_{powder}}{\rho_{CoCr}}$$

where: ρ_{powder} *= density of the powder*
m_{powder}*= weight of the powder*
V_{powder}*= volume of the powder*
P_{CoCr} *= density of the solidified material* [14]

The results of the experimental study on the filling factor are summarized in *Table 15*. The result is a filling factor of approximately 0.6 and a real layer thickness according to *Equation 10.10* of approximately 50 µm.

Personal experience has demonstrated that the measuring cup method of determining the real layer thickness is sufficiently accurate. Thus, the error caused by the compression of the powder due to weight, gravity, or vibration is negligible. The resulting error due to measurement uncertainty is empirically estimated to be 5 µm.

Table 15: Determination of the filling factor and the real layer thickness

	Weight powder [g]	Volume powder [cm³]	Density powder [g/cm³]	Fill factor [-]	Real layer thickness [µm]
Measurement 1	50.11	10	5.01	0.604	49.7
Measurement 2	99.23	20	4.96	0.598	50.2
Measurement 3	148.15	30	4.94	0.595	50.4
Measurement 4	206.65	40	5.17	0.622	48.2
				Mean	50.0

A3 Shape Factors

Area and perimeter are the two parameters by which the size of an object can be described. In order to compare objects that vary in size, values are needed that are independent of the actual size of the object [43]. *Table 16* shows a few examples for different objects.

Roundness: Specifies how closely the shape of an object resembles a circle. The closer the value is to 1, the more round is the object.

10.13
$$Roundness = 4 \cdot \frac{[Area]}{\pi[Major\ Axis]^2}$$

Circularity: Circularity is the ratio of the object surface to the object perimeter. The more circular an object is, the closer its value for circularity is to one. The measure *circularity* is more sensitive to small bumps that increase the perimeter than is the measure *roundness*.

10.14
$$Circularity = 4\pi \cdot \frac{[Area]}{[Perimeter]^2}$$

Solidity: Solidity is the ratio of the surface of the object to the convex surface of the object (convex surface is defined by a convex hull of the object in question). The solidity indicates the compactness of an object or how much an object is fissured.

10.15
$$Solidity = \frac{[Area]}{[Convex\ Area]}$$

Table 16 Circularity, roundness, and solidity of different shapes

						
Circularity	0.101	0.097	0.899	0.864	0.728	0.749
Roundness	0.997	0.714	0.997	0.717	0.450	0.860
Solidity	0.762	0.761	1.000	1.000	1.000	0.946

A4 Experiment Data Sheets

In this section, the experiment data sheets are listed. Every experiment data sheet corresponds to an experiment carried out for this work. The purpose of the experiment data sheets is to document the experiments and to note possible inconsistencies.

Experiment 1: Variation of Parameters

Name	Date	Experiment	Page
Stefan Popp	09/29/2014	R_20140929	1/2
Short Description			
Variation of Parameters & Mini Base Plate			

General Conditions			
System	**Inert Gas**	**Temp. Baseplate**	**Wavelength**
Renishaw AM-250	Argon	RT	1060 - 1100nm
Powder Material	**Particle Size**	**Focus diameter**	**Substrate Plate**
CoCr 2LC	15 - 45 µm	70 µm	A36

Constant Process Parameters		
Hatch Style: Stripes	Layer thickness: 30 µm	Focus offset: 0 µm
Stripe Width: 5 mm	Point distance: 70 µm	
Stripes overlap: 0.05 µm	Hatch Overlap: 0.125 mm	

Plate

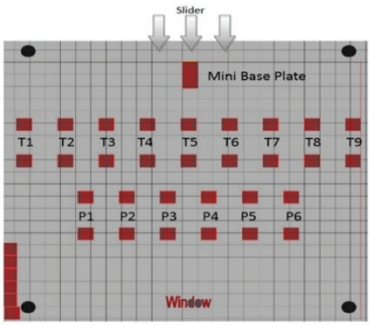

Build time: ca. 3.5 hr	No. of layers: 368	Software: Autofab

Notes: - Mini base plate wasn't built. It only built the support structures (reason unclear)
- Height of supports only 1-2 mm (reason unclear)
- wasn't present during building

Figure 67 Experiment data sheet corresponding to *Experiment 1* (page 1/2)

Name	Date	Experiment	Page
Stefan Popp	09/29/2014	R_20140929	2/2

Nr.	E [% E_0]	t_{exp} [µs]	P_L [mm]
T1	60	60	180
T2	70	70	180
T3	80	80	180
T4	90	90	180
T5	100	100	180
T6	110	110	180
T7	120	120	180
T8	130	130	180
T9	140	140	180
P1	≈60	100	100
P2	≈70	100	120
P3	≈80	100	140
P4	≈90	100	160
P5	≈100	100	180
P6	≈110	100	200

E Volume Energy

E_0 Standard Volume Energy (standard parameters given by Renishaw)

t_{exp} Exposure time

P_L Laser Power

Figure 68 Experiment data sheet corresponding to *Experiment 1* (page 2/2)

Experiment 2: Twincantilevers, Bridges, and Single Tracks

Name	Date	Experiment	Page
Stefan Popp	10/12/2014	R_20141012	1/2
Short Description Twincantilever – Bridges – Single Lines			

General Conditions			
System Renishaw AM-250	**Inert Gas** Argon	**Temp. Baseplate** RT	**Wavelength** 1060 - 1100nm
Powder Material CoCr 2LC	**Particle Size** 15 - 45 µm	**Focus diameter** 70 µm	**Substrate Plate** A36

Constant Process Parameters		
Hatch Style: Stripes Stripe Width: 5 mm Stripes overlap: 0.05 µm	Layer thickness: 30 µm Point distance: 70 µm Hatch Overlap: 0.125 mm	Focus offset: 0 µm

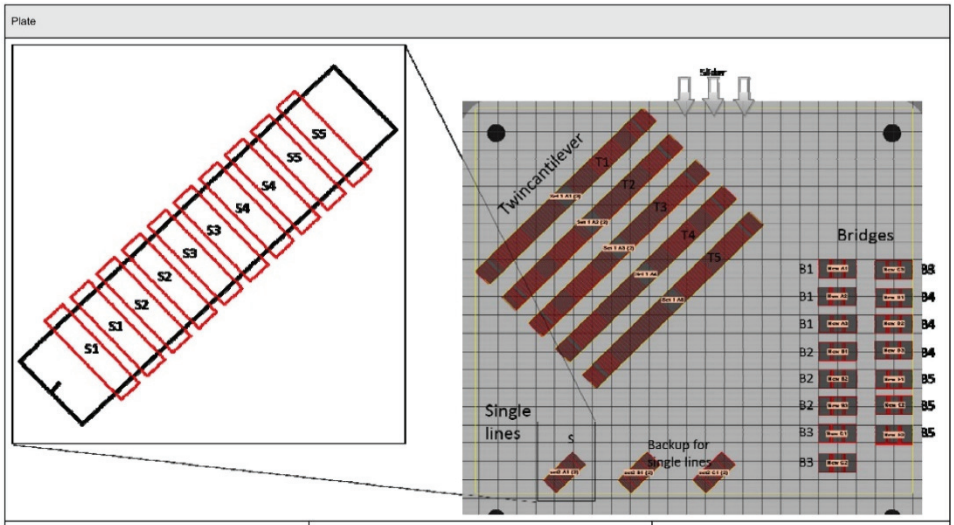

Build time: ca. 12 hr	No. of layers: 337	Software: Autofab
Notes: - was not present during the build - powder bed looked ok after build was done		

Figure 69 Experiment data sheet corresponding to *Experiment 2* (page 1/2)

Name	Date	Experiment	Page
Stefan Popp	10/12/2014	R_20141012	2/2

Nr.	E [% E_0]	t_{exp} [µs]	P_L [mm]
T1	90	100	160
T2	100	100	180
T3	110	100	200
T4	90	90	180
T5	110	110	180
B1	90	100	160
B2	100	100	180
B3	110	100	200
B4	90	90	180
B5	110	110	180
S1	90	100	160
S2	100	100	180
S3	110	100	200
S4	90	90	180
S5	110	110	180

E Volume Energy

E_0 Standard Volume Energy (standard parameters given by Renishaw)

t_{exp} Exposure time

P_L Laser Power

Figure 70 Experiment data sheet corresponding to *Experiment 2* (page 2/2)

Experiment 3: Tensile Specimen

Name	Date	Experiment	Page
Stefan Popp	10/07/2014	R_20141007	1/2
Short Description			
Tensile Specimen			

General Conditions			
System	**Inert Gas**	**Temp. Baseplate**	**Wavelength**
Renishaw AM-250	Argon	RT	1060 - 1100nm
Powder Material	**Particle Size**	**Focus diameter**	**Substrate Plate**
CoCr 2LC	15 - 45 µm	70 µm	A36

Constant Process Parameters		
Hatch Style: Stripes	Layer thickness: 30 µm	Focus offset: 0 µm
Stripe Width: 5 mm	Point distance: 70 µm	
Stripes overlap: 0.05 µm	Hatch Overlap: 0.125 mm	

Plate

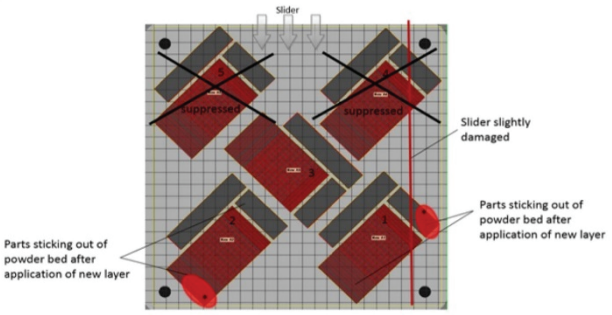

Build time: ca. 136 hr	No. of layers: 2500	Software: Autofab

Notes:
- Block 4 and 5 had to be suppressed after 3.8 mm (127) to reduce the built time (10 days – 5.5 days)
  1. Reason for suppressing 5: block 5 is scanned with the slowest velocity
  2. Reason for suppressing 4: block 4 damaged slider
  3. Block 4 and 5 are related -> either build both or non in order to be consistant
- Block 4 slightly damaged the slider before it was suppressed (probably due to too much energy input)
- Block 3 in perfect condition, completely covered in powder, visually best melting conditions
- Block 1 and 2 partially not completely cover by powder
- Areas marked with *: looks like low energy in put in this area, rest of part looks ok

Figure 71 Experiment data sheet corresponding to *Experiment 3* (page 1/2)

Name	Date	Experiment	Page
Stefan Popp	10/07/2014	R_20141007	2/2

Nr.	E [% E_0]	t_{exp} [µs]	P_L [mm]
1	90	100	160
2	100	100	180
3	110	100	200
4	90	90	180
5	140	140	180

E Volume Energy

E_0 Standard Volume Energy (standard parameters given by Renishaw)

t_{exp} Exposure time

P_L Laser Power

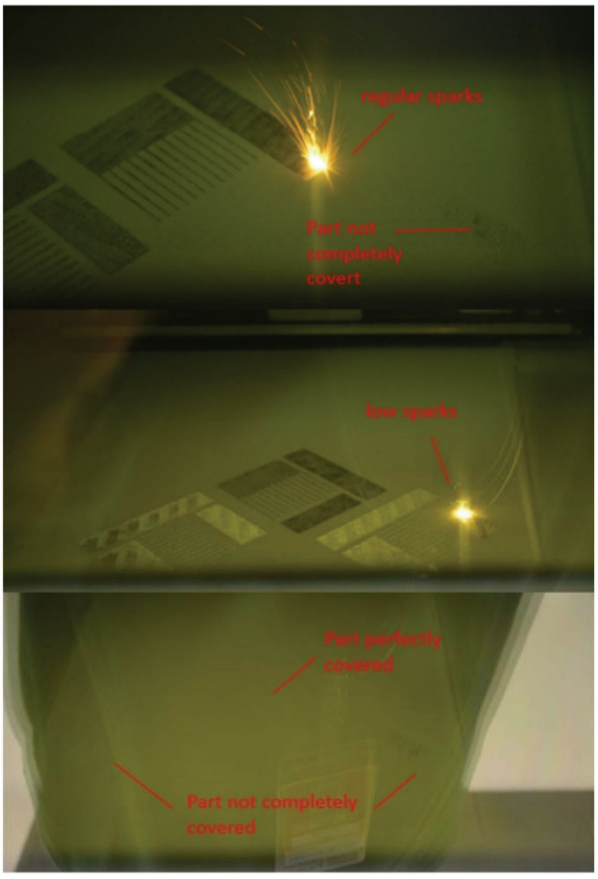

Figure 72 Experiment data sheet corresponding to *Experiment 3* (page 2/2)

A5 Pictures of Builds

Images of all constructed builds are depicted below.

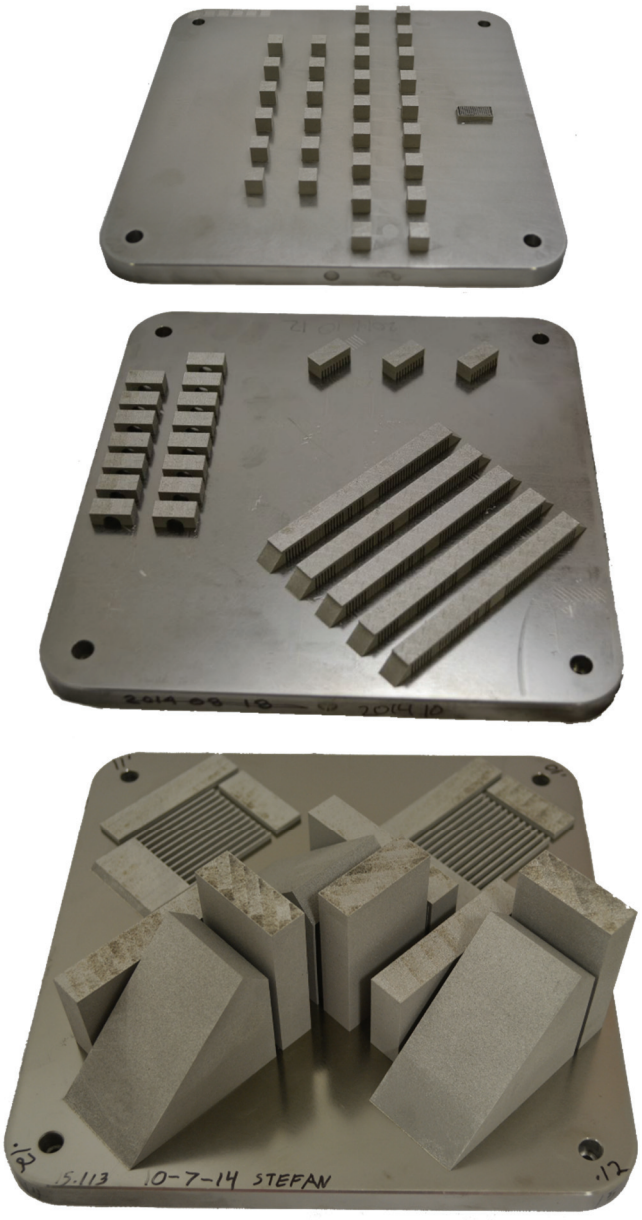

Figure 73 Top: Build 1 (cubes) to analyse density and microstructure
Middle: Build 2 (Twincantilevers, bridges, and single tracks) to analyze the deformation due to residual stress and the weld pool shape
Bottom: Build 3 (tensile blocks) to analyze mechanical properties

A6 CAD

Build 1: Cube

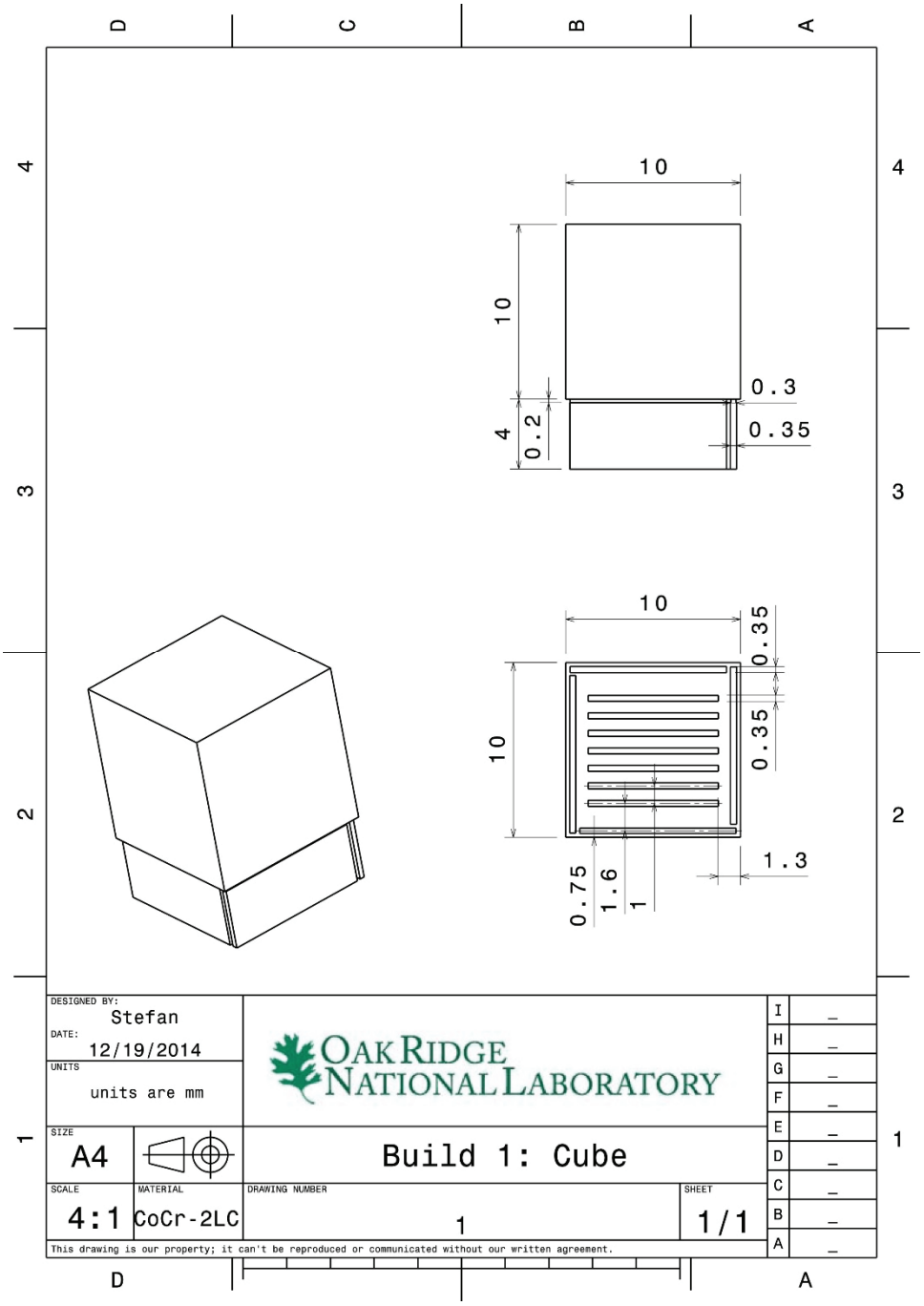

Figure 74 Technical drawing of parts used in *Experiment 1*

Build 2: Residual Stress

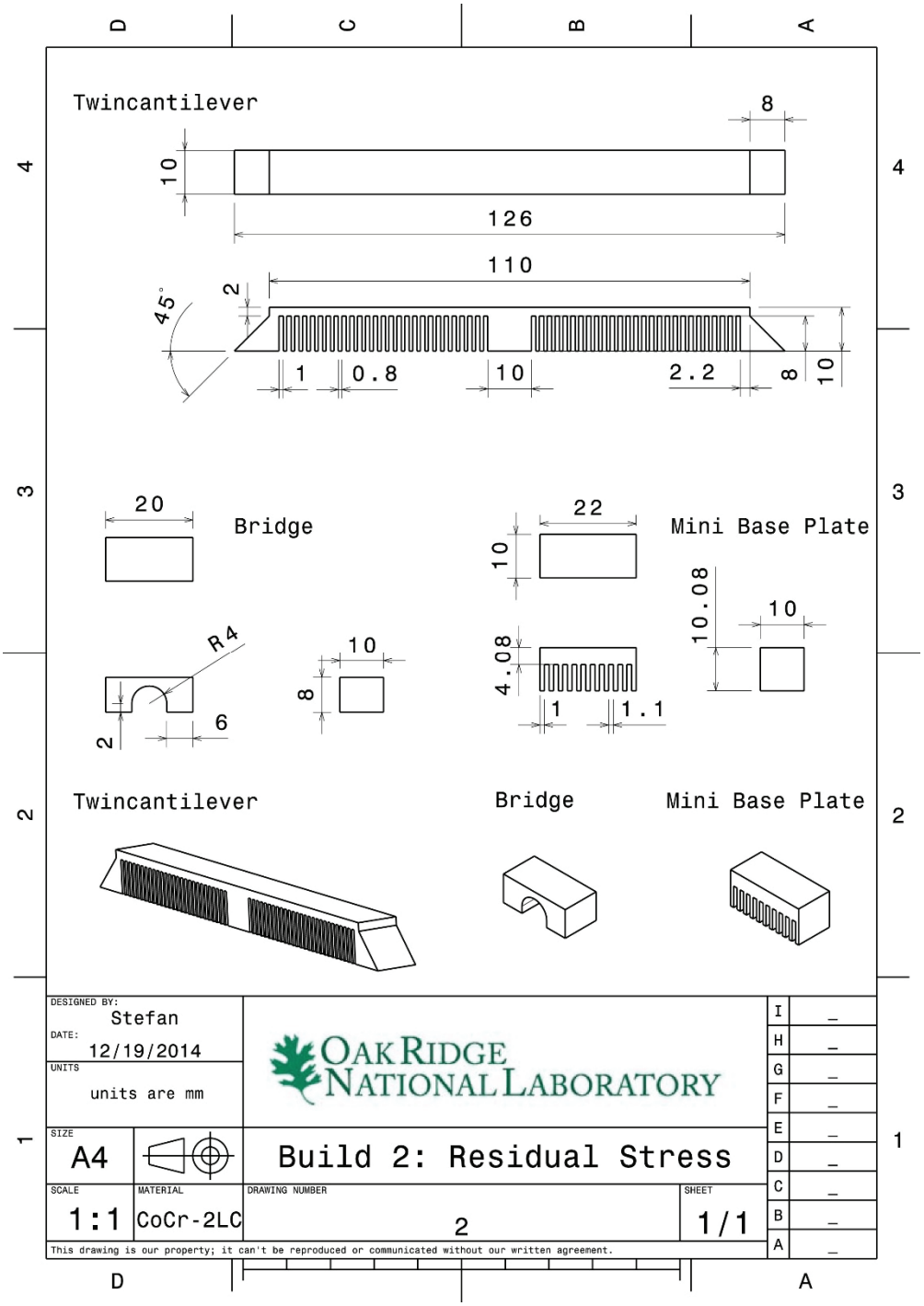

Figure 75 Technical drawing of parts used in *Experiment 2*

Build 3: Tensile Blocks

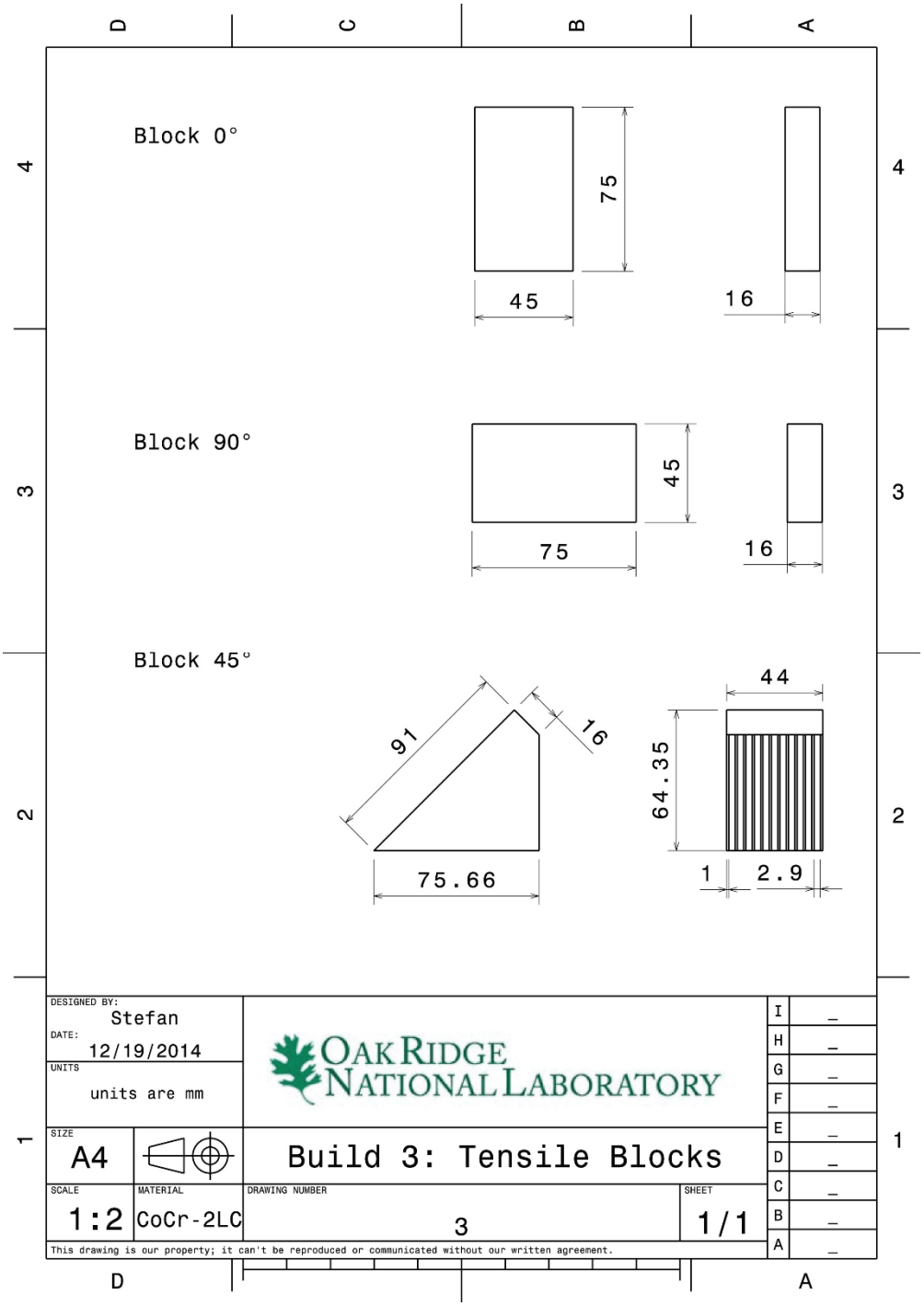

Figure 76 Technical drawing of parts used in *Experiment 3*

Build 3: Tensile Specimen

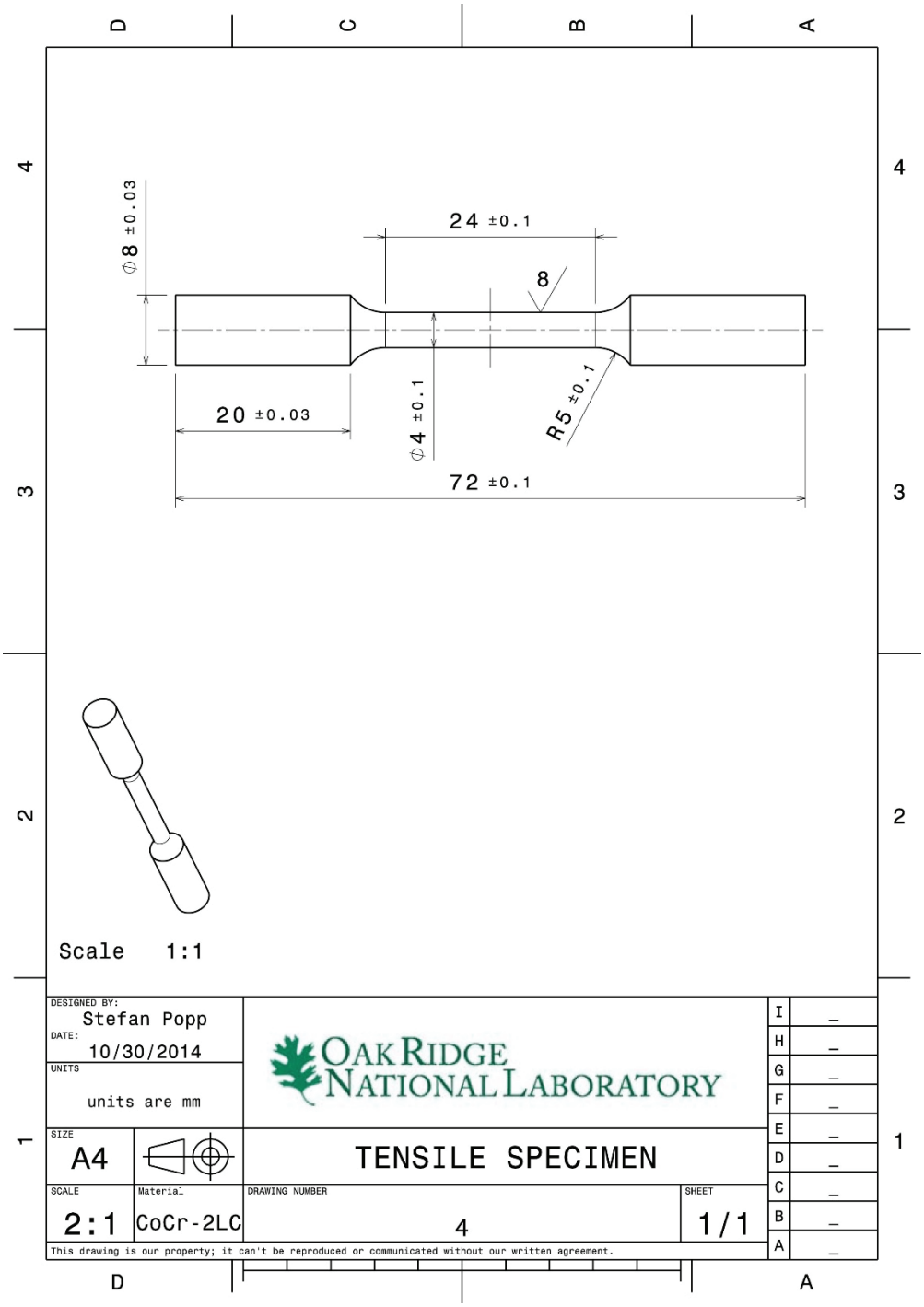

Figure 77 Technical drawing of tensile specimen

A7 Measuring Data

The measuring data used in this work is presented in this section. It contains screenshots of tables and additional pictures not shown in the main part of this work.

Section 1 Density

Sample #	Power W	Exposure time µs	Ev J/mm³	Ev % of Ev_0 (rounded)	Position low 1	Position low 2	Position low 3	Mean low Statistics O	Standard D low Statistics	Mean whole part Statistics	Standard D whole part Statistics
P1	100	100	38,1	60	89,083	88,358	88,785	87,60933	1,58041	87,93656	1,00541
P2	120	100	45,7	70	93,957	94,037	94,362	94,50767	0,4551	94,88289	0,39832
P3	140	100	53,3	80	98,009	97,307	98,021	98,03733	0,22665	97,94656	0,33078
P4	160	100	61	90	99,142	99,164	98,839	99,256	0,08839	99,07911	0,16905
P5	180	100	68,6	100	99,649	99,651	99,587	99,69467	0,13557	99,67356	0,07442
P6	200	100	76,2	110	99,855	99,765	99,804	99,83967	0,04302	99,82489	0,03942
Sample #	Power W	Exposure time µs	Ev J/mm³	Ev % of Ev\-(0) (rounded)	Position middle 1	Position middle 2	Position middle 3	Mean middle Statistics	Standard middle Statistics	--	--
P1	100	100	38,1	60	89,772	89,288	89,715	88,23933	0,41623	--	--
P2	120	100	45,7	70	94,35	93,247	93,905	94,997	0,23355	--	--
P3	140	100	53,3	80	97,798	97,457	97,833	98,022	0,40626	--	--
P4	160	100	61	90	99,206	99,136	99,159	99,07933	0,07974	--	--
P5	180	100	68,6	100	99,695	99,693	99,617	99,67033	0,04148	--	--
P6	200	100	76,2	110	99,827	99,738	99,75	99,83433	0,02466	--	--
Sample #	Power W	Exposure time µs	Ev J/mm³	Ev % of Ev\-(0) (rounded)	Position top 1	Position top 2	Position top 3	Mean top Statistics	Standard top Statistics	--	--
P1	100	100	38,1	60	90,571	90,16	90,308	87,961	1,03605	--	--
P2	120	100	45,7	70	92,816	93,408	92,795	95,144	0,19993	--	--
P3	140	100	53,3	80	97,128	97,773	97,675	97,78033	0,39862	--	--
P4	160	100	61	90	99,061	98,922	98,986	98,902	0,07843	--	--
P5	180	100	68,6	100	99,623	99,635	99,612	99,65567	0,02984	--	--
P6	200	100	76,2	110	99,751	99,85	99,87	99,80067	0,04914	--	--

Sample #	Power W	Exposure time µs	Ev J/mm³	Ev % of Ev\-(0) (rounded)	Position low 1	Position low 2	Position low 3	Mean top Statistics	Standard top Statistics	Mean whole part Statistics	Standard whole part Statistics
T1	180	60	41,1	60	87,568	86,05	89,21	87,60933	1,58041	87,93656	1,00541
T2	180	70	48	70	94,006	94,894	94,623	94,50767	0,4551	94,88289	0,39832
T3	180	80	54,9	80	98,299	97,902	97,911	98,03733	0,22665	97,94656	0,33078
T4	180	90	61,7	90	99,274	99,334	99,16	99,256	0,08839	99,07911	0,16905
T5	180	100	68,6	100	99,741	99,1	99,542	99,69467	0,13557	99,67356	0,07442
T6	180	110	75,4	110	99,886	99,832	99,801	99,83967	0,04302	99,82489	0,03942
T7	180	120	82,3	120	99,826	99,803	99,926	99,85167	0,06539	99,85922	0,05386
T8	180	130	89,1	130	99,773	99,911	99,917	99,867	0,08146	99,89733	0,06041
T9	180	140	96	140	99,865	99,831	99,872	99,856	0,02193	99,86589	0,04454
Sample #	Power W	Exposure time µs	Ev J/mm³	Ev % of Ev\-(0) (rounded)	Position middle 1	Position middle 2	Position middle 3	Mean middle Statistics	Standard middle Statistics		
T1	180	60	41,1	60	88,422	87,763	88,533	88,23933	0,41623		
T2	180	70	48	70	94,936	94,8	95,255	94,997	0,23355		
T3	180	80	54,9	80	98,489	97,75	97,827	98,022	0,40626		
T4	180	90	61,7	90	98,991	99,146	99,101	99,07933	0,07974		
T5	180	100	68,6	100	99,624	99,683	99,704	99,67033	0,04148		
T6	180	110	75,4	110	99,846	99,851	99,806	99,83433	0,02466		
T7	180	120	82,3	120	99,906	99,882	99,766	99,85133	0,07487		
T8	180	130	89,1	130	99,859	99,95	99,938	99,91567	0,04944		
T9	180	140	96	140	99,88	99,844	99,945	99,88967	0,05119		
Sample #	Power W	Exposure time µs	Ev J/mm³	Ev % of Ev\-(0) (rounded)	Position top 1	Position top 2	Position top 3	Mean top Statistics	Standard top Statistics		
T1	180	60	41,1	60	88,174	86,835	88,874	87,961	1,03605		
T2	180	70	48	70	95,176	95,326	94,93	95,144	0,19993		
T3	180	80	54,9	80	98,238	97,509	97,594	97,78033	0,39862		
T4	180	90	61,7	90	98,872	98,991	98,843	98,902	0,07843		
T5	180	100	68,6	100	99,636	99,641	99,69	99,65567	0,02984		
T6	180	110	75,4	110	99,838	99,819	99,745	99,80067	0,04914		
T7	180	120	82,3	120	99,902	99,886	99,836	99,87467	0,03443		
T8	180	130	89,1	130	99,947	99,939	99,842	99,90933	0,05845		
T9	180	140	96	140	99,785	99,872	99,899	99,852	0,05957		

Figure 78 Results from the density study (variation of laser power and exposure time)

Section 2: Melt Pool – Single Tracks

Sample	Volume En % E0	Laser powe W	Exp Time µs	Area µm²	Area µm²	Area µm²	Area µm²	Mean Statistics On	Standard Deviati Statistics On Ro
S1	90	160	100	4485,46	6672,34	6732,373		5963,391	1280,27771
S2	100	180	100	6008,28	7287,562	8299,734	10234,176	7957,438	1784,06402
S3	110	200	100	11247,349	7036,243	6131,292	--	8138,29467	2730,27438
S4	90	180	90	6410,36	5573,687	5588,18	10880,385	7113,153	2541,74829
S5	110	180	110	6024,425	5812,223	5798,874	11340,63	7244,038	2733,01513

Figure 79 Melt pool area of the single tracks

Sample	Volume En % E0	Laser powe W	Exp Time µs	x µm	x µm	x µm	x µm	Mean Statistics On	Standard D Statistics
S1	90	160	100	80,63	96,16	72,98		83,25667	11,81112
S2	100	180	100	93,36	113,74	111,87	111,32	107,5725	9,53145
S3	110	200	100	133,26	113,64	107,15	--	118,01667	13,5941
S4	90	180	90	87,3	94,55	96,64	108,5	96,7475	8,79805
S5	110	180	110	109,74	102,29	96,73	106,67	103,8575	5,65014

Sample	Volume En % E0	Laser powe W	Exp Time µs	x µm	x µm	x µm	x µm	Mean Statistics	Standard D Statistics
S1	90	160	100	65,16	57,36	70,93		64,48333	6,81026
S2	100	180	100	79,46	87,39	88,78	101,99	89,405	9,34052
S3	110	200	100	109,9	98,84	80,02	--	96,25333	15,10701
S4	90	180	90	86,61	72,66	78,85	106,92	86,26	14,9089
S5	110	180	110	77,97	76,36	70,19	115,27	84,9475	20,49121

Figure 80 Melt pool width (top) and height (bottom) of the single tracks

Sample	Volume En % E0	Laser powe W	Exp Time µs	Rnd	Rnd	Rnd	Rnd	Mean Statistics	Standard D Statistics
S1	90	160	100	0,67	0,84	0,606		0,70533	0,12094
S2	100	180	100	0,924	0,936	0,835	0,954	0,91225	0,05296
S3	110	200	100	0,782	0,869	0,711	--	0,78733	0,07913
S4	90	180	90	0,885	0,784	0,808	0,789	0,8165	0,04682
S5	110	180	110	0,76	0,801	0,738	0,931	0,8075	0,08637

Sample	Volume En % E0	Laser powe W	Exp Time µs	Circ	Circ	Circ	Circ	Mean Statistics	Standard D Statistics
S1	90	160	100	0,791	0,861	0,832		0,828	0,03517
S2	100	180	100	0,949	0,864	0,915	0,94	0,917	0,03815
S3	110	200	100	0,895	0,934	0,873	--	0,90067	0,03089
S4	90	180	90	0,881	0,891	0,881	0,903	0,889	0,01046
S5	110	180	110	0,865	0,915	0,884	0,942	0,9015	0,03397

Sample	Volume En % E0	Laser powe W	Exp Time µs	Sol	Sol	Sol	Sol	Mean Statistics	Standard D Statistics
S1	90	160	100	0,95	0,973	0,965		0,96267	0,01168
S2	100	180	100	0,99	0,961	0,987	0,979	0,97925	0,01302
S3	110	200	100	0,972	0,987	0,98	--	0,97967	0,00751
S4	90	180	90	0,979	0,987	0,978	0,97	0,9785	0,00695
S5	110	180	110	0,983	0,986	0,981	0,989	0,98475	0,0035

Figure 81 Melt pool roundness, circularity and solidity of the single tracks

Section 2: Melt Pool – Skin Tracks

Sample	Volume En % E0	Laser powe W	Exp Time µs	Area µm²	Area µm²	Area µm²	Area µm²	Area µm²	Area µm²	Area µm²	Area µm²	Area µm²	Area µm²
P4	90	160	100	5522,10425	6077,72314	4172,60542	4104,88919	5674,95042	5422,46418	3861,90475	5439,19401	4209,25264	7599,87156
P5	100	180	100	5320,83139	6221,80643	6196,19974	5629,42731	8469,54867	7307,15257	5237,92115	5496,72455	7663,54829	5374,77738
P6	110	200	100	8083,50579	8291,03785	10591,58726	7252,8656	7188,67694	8704,96412	9607,58896	7295,48708	9596,43541	8850,0143
P4	90	160	100	5351,78835	4447,79769	6242,00781	5378,3629	7704,86094	6243,43062	5721,84033	4755,53876	6470,08221	4734,02855
P5	100	180	100	8627,63016	5837,07238	6111,24077	5571,49784	6046,88113	6705,95261	6551,74062	4739,20688	7084,9394	5843,27556
P6	110	200	100	6578,65711	7382,89274	8056,53328	9241,91842	8870,72761	7074,69672	10949,63278	8984,70783	9162,9337	8927,00631
P4	90	160	100	5520,96639	5649,45771	6441,80087	4742,39444	6479,18703	7259,97868	5280,31563	6221,52149	7598,27778	11158,53066
P5	100	180	100	6753,52542	5602,90878	6979,83604	8220,703	5918,33282	6474,23666	7495,62208	7676,69261	8124,87543	7140,13723
P6	110	200	100	8030,47067	8770,91656	6793,87117	6770,99515	7612,84588	7279,78209	10366,64245	9214,20504	9379,2296	8544,94691
				MEAN P	SD P	--	--	--	--	--	--	--	--
P4	90	160	100	5478,72155	1011,9797	--	--	--	--	--	--	--	--
P5	100	180	100	6550,38644	1018,3219	--	--	--	--	--	--	--	--
P6	110	200	100	8535,94535	1250,21941	--	--	--	--	--	--	--	--
T4	90	180	90	5835,70656	6212,36065	5762,18608	5232,17389	5524,66492	7123,06546	6326,73882	6114,9393	5778,97291	6385,97712
T5	100	180	100	5320,83139	6221,80643	6196,19974	5629,42731	8469,54867	7307,15257	5237,92115	5496,72455	7663,54829	5374,77738
T6	110	180	110	9094,93252	9353,96388	8053,85863	10527,74053	7596,34303	8186,61741	9271,22364	7525,7242	8210,5743	9991,98107
T4	90	180	90	5104,02451	7258,3849	5930,96617	5729,57933	4954,19396	4919,25449	5030,44608	4307,12894	6246,56021	4491,50003
T5	100	180	100	8627,63016	5837,07238	6111,24077	5571,49784	6046,88113	6705,95261	6551,74062	4739,20688	7084,9394	5843,27556
T6	110	180	110	7858,27604	10157,34661	10333,40977	7992,74257	7186,45724	9321,01615	8334,51321	10367,26837	7504,95389	11203,25785
T4	90	180	90	7261,68547	5561,19817	5689,68949	5972,67678	4788,65746	4944,63419	5440,7308	6218,39189	5405,16444	5551,41044
T5	100	180	100	6753,52542	5602,90878	6979,83604	8220,703	5918,33282	6474,23666	7495,62208	7676,69261	8124,87543	7140,13723
T6	110	180	110	10475,78627	9925,57271	6499,61636	7464,66513	7505,01088	7406,90663	6156,93486	7171,49215	9517,33768	7500,23148
				MEAN T	SD T								
T4	90	180	90	5703,43545	745,81497								
T5	100	180	100	6550,38644	1018,3219								
T6	110	180	110	8592,69047	1334,16691								

Figure 82 Melt pool area skin tracks

Sample	Volume En % E0	Laser powe W	Exp Time µs	Length x & y µm	Length x & y µm	Length x & y µm	Length x & y µm	Length x & y µm	Length x & y µm	Length x & y µm	Length x & y µm	Length x & y µm	Length x & y µm
P4	90	160	100	106,47111	115,35183	103,20434	96,47474	124,70006	106,90481	101,6521	114,01112	100,24668	124,93381
P5	100	180	100	119,5565	121,28261	114,33567	129,61952	135,32428	124,52909	113,13986	135,98304	126,28031	117,3426
P6	110	200	100	134,63267	135,01325	152,23957	132,21786	146,26435	143,14828	143,50953	132,74429	148,23098	140,79142
P4	90	160	100	120,2993	105,41245	129,21576	123,77663	120,35726	114,19175	112,40092	108,0929	126,65896	112,5632
P5	100	180	100	146,03253	121,6854	120,51953	118,22159	119,0861	128,98877	128,74632	113,05872	126,12866	115,67638
P6	110	200	100	139,88538	141,80564	148,30729	142,27025	142,61122	141,07733	152,88577	143,45834	141,62984	157,9849
P4	90	160	100	118,0004	120,01339	119,73134	115,79809	--	--	--	--	--	--
P5	100	180	100	131,60836	113,27026	133,27845	118,17233	125,97315	119,75065	134,15647	131,83245	146,62947	115,53535
P6	110	200	100	136,69106	139,16576	137,22715	120,14185	143,55879	135,51167	136,56356	142,28957	141,31398	136,00912
--	--	--	--	MEAN P x	SD P x	--	--	--	--	--	--	--	--
P4	90	160	100	114,18596	9,03221	--	--	--	--	--	--	--	--
P5	100	180	100	125,19182	9,02252	--	--	--	--	--	--	--	--
P6	110	200	100	141,79302	8,39587	--	--	--	--	--	--	--	--
P4	90	160	100	75,507	69,178	57,226	56,866	65,254	69,126	51,805	69,087	56,183	89,478
P5	100	180	100	62,837	71,436	72,252	63,801	89,674	79,607	62,409	54,08	83,817	63,554
P6	110	200	100	81,78	87,573	94,202	79,314	67,029	83,338	90,355	76,773	89,405	88,133
P4	90	160	100	58,152	56,309	62,084	61,616	86,842	71,609	65,503	58,519	67,081	57,624
P5	100	180	100	79,239	71,892	71,151	58,914	67,37	74,032	69,081	58,866	72,664	68,959
P6	110	200	100	68,462	73,764	70,556	95,251	75,098	70,253	82,04	102,311	81,225	86,457
P4	90	160	100	64,27	64,999	78,209	57,314	--	--	--	--	--	--
P5	100	180	100	73,585	65,529	76,629	89,813	68,487	73,332	80,806	80,734	83,498	85,476
P6	110	200	100	76,798	82,101	67,677	74,519	77,703	76,037	95,206	87,918	94,319	92,361
--	--	--	--	MEAN P y	SD P y	--	--	--	--	--	--	--	--
P4	90	160	100	65,41004	9,63111	--	--	--	--	--	--	--	--
P5	100	180	100	72,63537	8,77024	--	--	--	--	--	--	--	--
P6	110	200	100	82,70419	9,60347	--	--	--	--	--	--	--	--
T4	90	180	90	112,5632	111,14619	123,29367	110,08753	113,26253	126,1644	117,90284	98,87024	123,26373	119,23582
T5	100	180	100	119,5565	121,28261	114,33567	129,61952	135,32428	124,52909	113,13986	135,98304	126,28031	117,3426
T6	110	180	110	136,21389	137,15181	143,43612	151,78752	139,43139	134,28494	148,95542	132,3753	136,29407	134,18642
T4	90	180	90	112,26087	117,79659	116,06082	112,37678	112,53712	108,41841	122,83099	105,37092	122,76724	120,78806
T5	100	180	100	146,03253	121,6854	120,51953	118,22159	119,0861	128,98877	128,74632	113,05872	126,12866	115,67638
T6	110	180	110	132,8544	143,01305	151,00512	135,85167	128,84098	140,58761	126,06974	142,3823	138,14671	162,60975
T4	90	180	90	137,91489	113,11088	113,13986	123,03867	107,24095	115,58462	121,16091	120,1293	120,9088	121,35216
T5	100	180	100	131,60836	113,27026	133,27845	118,17233	125,97315	119,75065	134,15647	131,83245	146,62947	115,53535
T6	110	180	110	156,2385	147,2496	134,13715	130,22226	134,46557	124,52716	119,7835	138,26069	153,33203	133,17992
--	--	--	--	MEAN T x	SD T x	--	--	--	--	--	--	--	--
T4	90	180	90	116,68596	7,49328	--	--	--	--	--	--	--	--
T5	100	180	100	125,19182	9,02252	--	--	--	--	--	--	--	--
T6	110	180	110	139,11815	9,64605	--	--	--	--	--	--	--	--
T4	90	180	90	67,749	79,28	65,151	68,701	69,943	78,229	81,922	74,5	65,934	69,568
T5	100	180	100	62,837	71,436	72,252	63,801	89,674	79,607	62,409	54,08	83,817	63,554
T6	110	180	110	79,547	86,842	81,017	95,065	73,013	86,031	85,498	77,373	84,8	98,536
T4	90	180	90	66,346	85,088	73,401	69,754	58,31	67,326	58,102	56,727	72,378	49,752
T5	100	180	100	79,239	71,892	71,151	58,914	67,37	74,032	69,081	58,866	72,664	68,959
T6	110	180	110	82,73	97,788	90,005	81,467	78,705	88,596	94,963	94,868	82,26	89,938
T4	90	180	90	74,505	66,368	68,78	68,355	58,957	66,721	66,526	71,216	60,602	73,903
T5	100	180	100	73,585	65,529	76,629	89,813	68,487	73,332	80,806	80,734	83,498	85,476
T6	110	180	110	87,513	88,364	65,39	77,479	76,844	78,165	67,999	76,477	83,122	79,622
--	--	--	--	MEAN T y	SD T y								
T4	90	180	90	68,4698	7,67946								
T5	100	180	100	72,63537	8,77024								
T6	110	180	110	83,52623	8,07331								

Figure 83 Melt pool width and height of the skin tracks

Sample	Volume En % E0	Laser powe W	Exp Time µs	Round&Circ	Round&Circ	Round&Circ	Round&Circ	Round&Circ	Round&Circ	Round&Circ	Round&Circ	Round&Circ	Round&Circ
P4	90	160	100	0,73324	0,6535	0,57095	0,64302	0,53107	0,68958	0,49807	0,63063	0,57614	0,72522
P5	100	180	100	0,60557	0,69077	0,64927	0,62243	0,51181	0,60874	0,62148	0,62686	0,6494	0,69336
P6	110	200	100	0,60371	0,67653	0,58259	0,63402	0,60962	0,6895	0,78371	0,80963	0,54767	0,62165
P4	90	160	100	0,49126	0,58417	0,50206	0,50034	0,73434	0,65006	0,60274	0,54118	0,57379	0,52874
P5	100	180	100	0,54249	0,54126	0,49997	0,71883	0,62962	0,49463	0,6985	0,63013	0,60241	0,56847
P6	110	200	100	0,66009	0,74601	0,67053	0,66726	0,53034	0,68458	0,48473	0,51657	0,61029	0,44345
P4	90	160	100	0,54837	0,57557	0,66673	0,52438	--	--	--	--	--	--
P5	100	180	100	0,62286	0,60626	0,50494	0,68287	0,53262	0,57447	0,71656	0,64456	0,7492	0,74167
P6	110	200	100	0,55576	0,59216	0,62438	0,55375	0,60613	0,63169	0,56133	0,63807	0,48682	0,57217
--	--	--	--	MEAN P Round	SD P Round	--	--	--	--	--	--	--	--
P4	90	160	100	0,5948	0,07741	--	--	--	--	--	--	--	--
P5	100	180	100	0,62211	0,07301	--	--	--	--	--	--	--	--
P6	110	200	100	0,61316	0,08403	--	--	--	--	--	--	--	--
T4	90	180	90	0,60371	0,67653	0,58259	0,63402	0,60962	0,6895	0,78371	0,80963	0,54767	0,62165
T5	100	180	100	0,57181	0,58797	0,62191	0,47986	0,66954	0,66895	0,56768	0,42458	0,68196	0,54189
T6	110	180	110	0,60367	0,65642	0,56191	0,69518	0,55401	0,6536	0,62599	0,61936	0,65513	0,76794
T4	90	180	90	0,66009	0,74601	0,67053	0,66726	0,53034	0,68458	0,48473	0,51657	0,61029	0,44345
T5	100	180	100	0,57872	0,56856	0,56366	0,55584	0,54534	0,59426	0,56448	0,54686	0,61392	0,62558
T6	110	180	110	0,65021	0,71226	0,62867	0,6264	0,66436	0,69788	0,76905	0,61091	0,60273	0,58341
T4	90	180	90	0,55576	0,59216	0,62438	0,55375	0,60613	0,63169	0,56133	0,63807	0,48682	0,57217
T5	100	180	100	0,56047	0,59427	0,59419	0,72548	0,55636	0,66165	0,6034	0,62135	0,56787	0,81505
T6	110	180	110	0,60568	0,61428	0,49101	0,59925	0,60724	0,61889	0,58764	0,57382	0,58658	0,59512
--	--	--	--	MEAN T Round	SD T Round	--	--	--	--	--	--	--	--
T4	90	180	90	0,61316	0,08403	--	--	--	--	--	--	--	--
T5	100	180	100	0,59785	0,06745	--	--	--	--	--	--	--	--
T6	110	180	110	0,62603	0,0586	--	--	--	--	--	--	--	--
P4	90	160	100	0,9	0,851	0,796	0,796	0,713	0,862	0,753	0,78	0,707	0,855
P5	100	180	100	0,728	0,805	0,804	0,712	0,853	0,866	0,782	0,649	0,875	0,727
P6	110	200	100	0,798	0,801	0,814	0,765	0,684	0,774	0,771	0,757	0,841	0,816
P4	90	160	100	0,734	0,758	0,755	0,742	0,668	0,861	0,842	0,795	0,792	0,775
P5	100	180	100	0,758	0,736	0,806	0,758	0,799	0,822	0,779	0,756	0,781	0,782
P6	110	200	100	0,712	0,732	0,675	0,832	0,81	0,715	0,813	0,807	0,762	0,74
P4	90	160	100	0,785	0,796	0,857	0,733	--	--	--	--	--	--
P5	100	180	100	0,779	0,789	0,811	0,91	0,784	0,831	0,761	0,749	0,746	0,869
P6	110	200	100	0,781	0,797	0,717	0,805	0,704	0,706	0,806	0,842	0,852	0,887
--	--	--	--	MEAN T Round	SD T Round	--	--	--	--	--	--	--	--
P4	90	160	100	0,79608	0,05448	--	--	--	--	--	--	--	--
P5	100	180	100	0,78631	0,05078	--	--	--	--	--	--	--	--
P6	110	200	100	0,77948	0,0543	--	--	--	--	--	--	--	--
T4	90	180	90	0,778	0,866	0,766	0,794	0,792	0,857	0,884	0,897	0,811	0,817
T5	100	180	100	0,728	0,805	0,804	0,712	0,853	0,866	0,782	0,649	0,875	0,727
T6	110	180	110	0,785	0,806	0,723	0,749	0,711	0,798	0,736	0,803	0,822	0,829
T4	90	180	90	0,786	0,882	0,842	0,821	0,776	0,836	0,72	0,737	0,774	0,64
T5	100	180	100	0,758	0,736	0,806	0,758	0,799	0,822	0,779	0,756	0,781	0,782
T6	110	180	110	0,815	0,759	0,804	0,745	0,79	0,85	0,86	0,827	0,775	0,768
T4	90	180	90	0,76	0,805	0,795	0,745	0,791	0,762	0,797	0,802	0,738	0,722
T5	100	180	100	0,779	0,789	0,811	0,91	0,784	0,831	0,761	0,749	0,746	0,869
T6	110	180	110	0,784	0,8	0,667	0,814	0,768	0,794	0,792	0,748	0,775	0,793
--	--	--	--	MEAN T Round	SD T Round	--	--	--	--	--	--	--	--
T4	90	180	90	0,7931	0,05527	--	--	--	--	--	--	--	--
T5	100	180	100	0,78631	0,05078	--	--	--	--	--	--	--	--
T6	110	180	110	0,78371	0,04087	--	--	--	--	--	--	--	--

Figure 84 Melt pool roundness, circularity and solidity of the skin tracks

Section 3: Twincantilever

measuring plane -	TC 1 mm TC 1	TC 2 mm TC 2	TC 3 mm TC 3	TC 4 mm TC 4	TC 5 mm TC 5	Mean Statistics	Standard D Statistics
1	2,12	1,92	2,03	1,97	2,25	2,058	0,13065
2	1,32	1,5	1,2	1,3	1,42	1,348	0,11541
3	0,72	0,55	0,64	0,55	0,84	0,66	0,12309
4	0,3	0,16	0,19	0,15	0,41	0,242	0,11122
5	0	-0,02	-0,01	-0,04	0,18	0,022	0,08955
6	0	-0,09	-0,07	-0,01	0,05	-0,024	0,05639
7	-0,04	-0,02	-0,05	-0,1	0,06	-0,03	0,05831
8	0,03	-0,09	-0,01	-0,09	0,11	-0,01	0,08485
9	0,28	0,14	0,16	0,2	0,4	0,236	0,10621
10	0,71	0,54	0,63	0,56	0,83	0,654	0,11887
11	1,31	1,14	1,27	1,17	1,4	1,258	0,10569
12	2,29	1,9	2,07	1,95	2,16	2,074	0,15789

Figure 85 Deformation of the twincantilever in z-direction

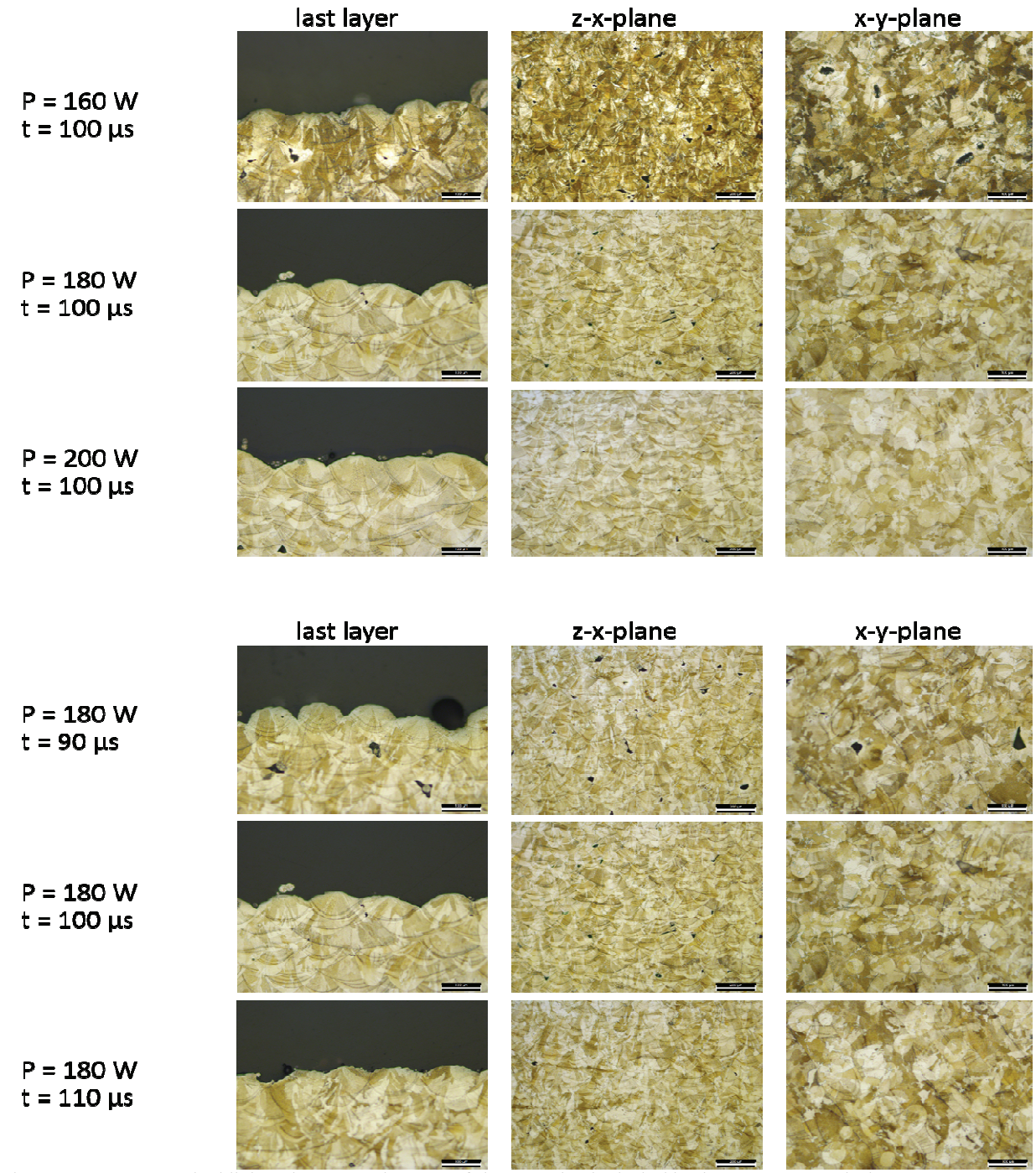

Figure 86 Optical light microscope images of the samples included in the parameter window

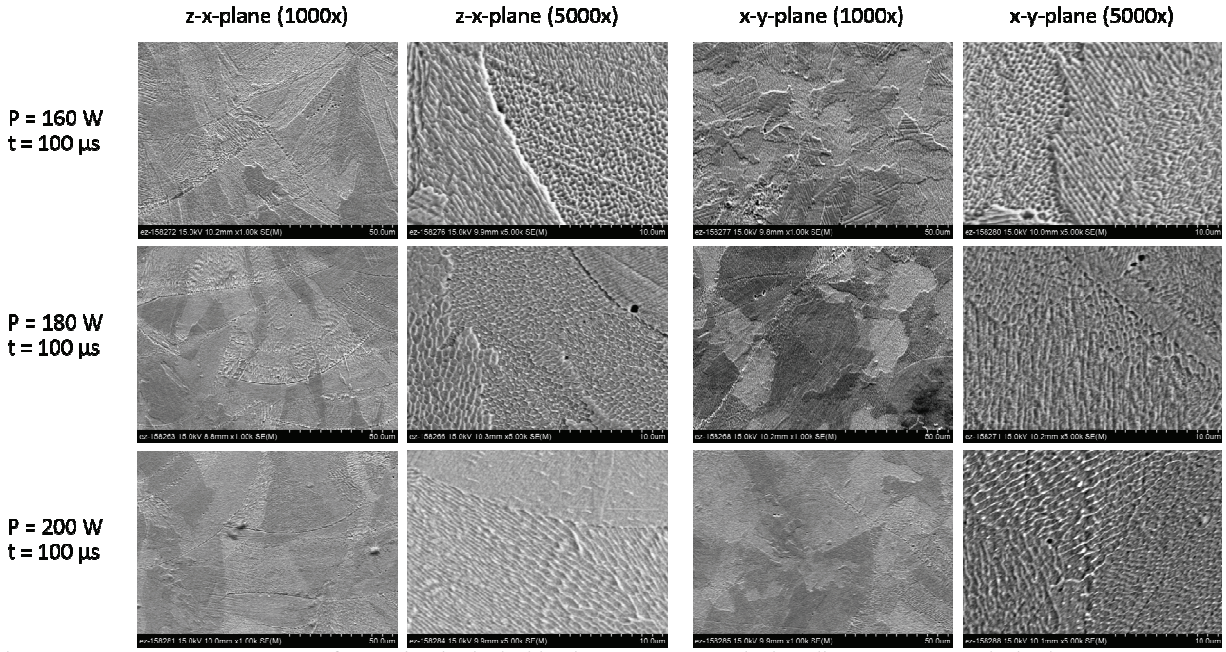

Figure 87 SEM Images of samples included in the parameter window (laser power variation)

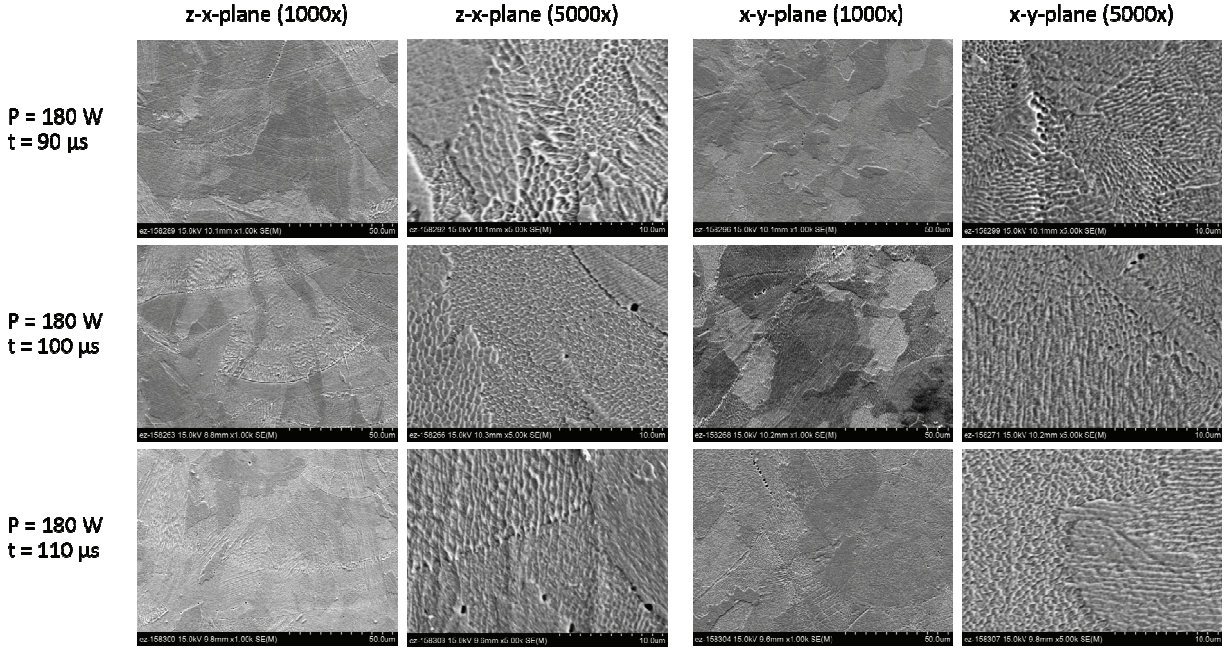

Figure 88 SEM Images of samples included in the parameter window (exposure time variation)

Sample	Wt% Cr%	Wt% Cr%	Wt% Cr%	Wt% Cr%	Wt% Cr%
Sample	whole	Boundary	Boundary	bulk	bulk
P4	26,32	26,34	0,34409	25,984	0,22689
P5	26,87	26,516	0,49475	26,492	0,24129
P6	26,31	26,25333	0,14295	26,13333	0,35346
T4	26,55	26,09333	0,36774	26,42	0,5003
T5	26,87	26,516	0,49475	26,492	0,24129
T6	26,54	26,36667	0,03215	26,67333	0,14572

Sample	Wt% Mo%	Wt% Mo%	Wt% Mo%	Wt% Mo%	Wt% Mo%
Sample	whole	Boundary	Boundary	bulk	bulk
P4	5,88	5,67	0,13398	5,986	0,34093
P5	5,41	5,726	0,25363	5,686	0,11216
P6	5,78	5,77333	0,11372	6,02333	0,15177
T4	5,86	5,96667	0,55582	5,8	0,1852
T5	5,41	5,726	0,25363	5,686	0,11216
T6	5,88	6,02333	0,40649	5,75	0,11533

Figure 89 Results of EDS analysis (Chrome content left and Molybdenum content right)

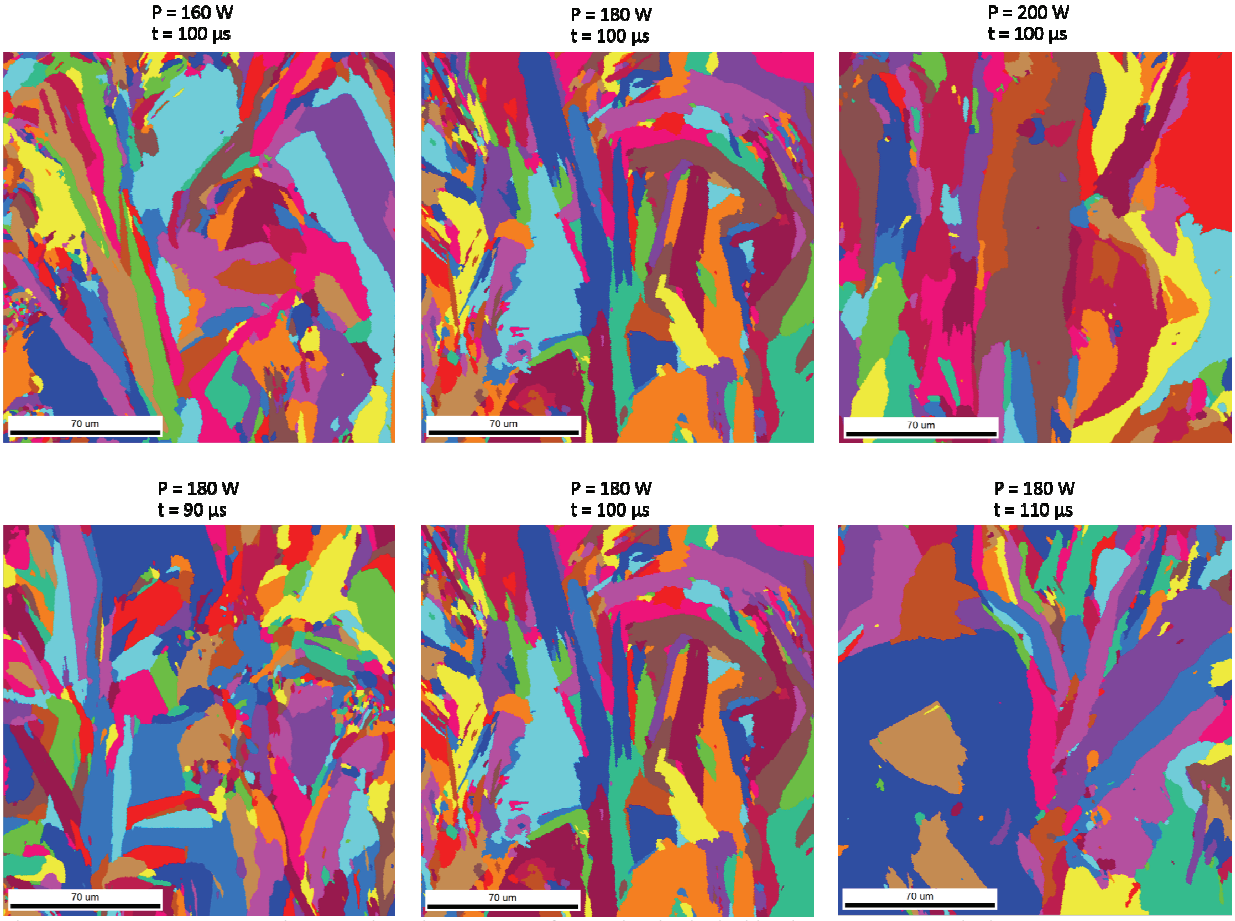

Figure 90 EBSD unique grain colour maps of samples included in the parameter window

Section 5: Tensile Test

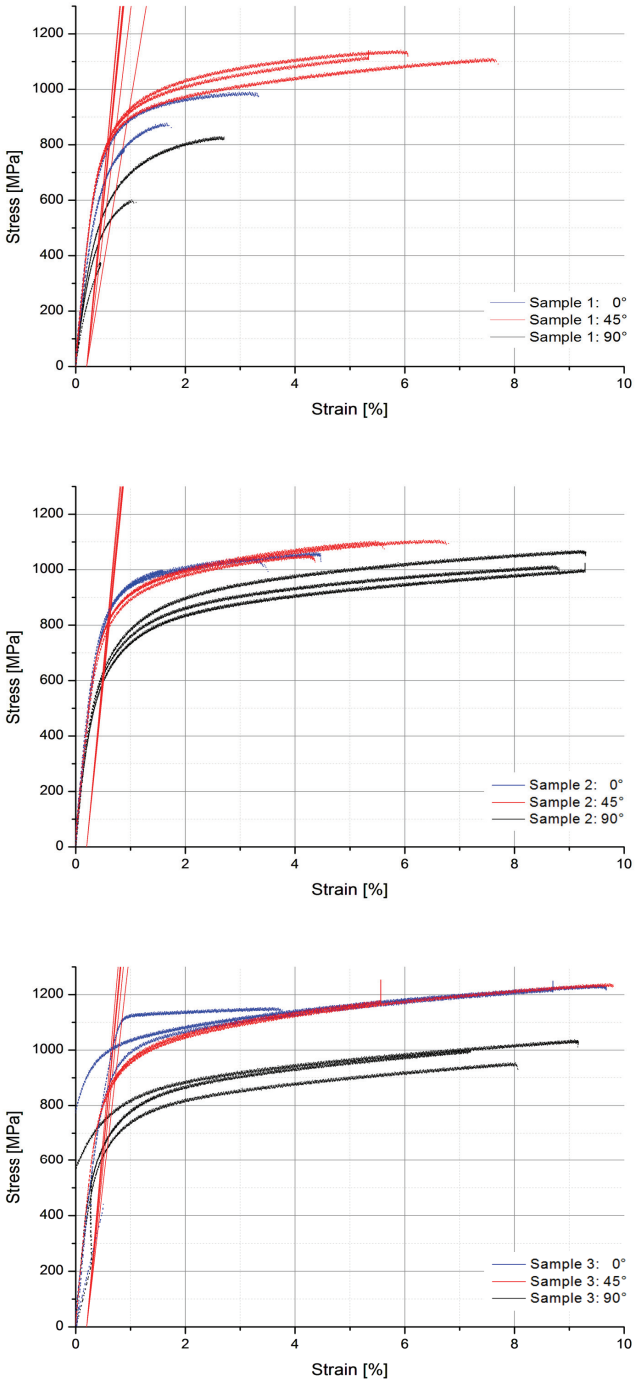

Figure 91 Stress-strain curves of tenile blocks 1 (top), blocks 2 (middle) and blocks 3 (bottom)

Vita

Stefan Popp was born in Marktheidenfeld, Bavaria in Germany. He attended the University of Applied Sciences in Aachen, where he obtained a Bachelor of Engineering degree in Aerospace Engineering. During his studies, Stefan gained research experience pertaining to selective laser melting at Fraunhofer Center for Laser Technology in Aachen. Stefan went on to study Mechanical Engineering at the University of Tennessee. He completed his Master's Thesis at Oak Ridge National Laboratory in the field of additive manufacturing. Stefan's initially came to the United States was to be with his American wife; the two now share a beautiful daughter. Stefan strongly dislikes writing about himself in the third person.